The Atypical Protein Kinase C - Creb Binding Protein Pathway Regulates Post-Stroke Neurovascular Remodeling and Functional Recovery

Ayden Gouveia

Thesis submitted to the
Faculty of Graduate and Postdoctoral Studies
In partial fulfillment of the requirements for the
MSc degree in Neuroscience

Department of Cellular Molecular Medicine
Faculty of Medicine
University of Ottawa

©Ayden Gouveia, Ottawa, Canada 2016

Abstract

Ischemic stroke related brain damage causes loss of multiple cell types, including neural and vascular cells. The extent of post-stroke neurogenesis and angiogenesis predicts the level of functional regeneration/recovery after stroke. In this regard, my thesis was focused on defining the molecular process that modulates post-stroke functional recovery by co-ordinating post-stroke neurovascular remodeling. Since stroke-related brain damage releases enriched local microenvironmental cues, I examined the role of a signaling-induced epigenetic pathway, an atypical protein kinase C (aPKC)-mediated phosphorylation of CREB Binding Protein (CBP), in regulating post-stroke neurovascular remodeling and functional recovery. This pathway, has previously been shown to be activated by metformin, an adenosine monophosphate kinase (AMPK) activator, to promote the differentiation of neural precursors in the developing and adult brain. Here, I first developed a murine focal cortical ischemic stroke model with persistent motor function deficits by combined intra-cortical injections of endothelin-1 (ET-1) and L-NAME into the sensorimotor cortex. Second, I applied the ET-1/L-Name-induced focal cortical stroke model in a knock-in mouse CBPS436A where the aPKC-CBP pathway is deficient, and showed that the aPKC-CBP pathway is involved in post-stroke functional recovery by coordinating neurovascular remodeling. Specifically, CBPS436A-KI mice displayed reduced motor recovery, correlated with reduced vascular remodeling and impaired post-stroke angiogenesis. Intriguingly, I also observed that CBPS436A-KI mice showed a reduction in the population of stroke-induced newborn pericytes but an increase in the population of perivascularly-derived neural precursors, implying that the aPKC-CBP pathway may be involved in the process that reprograms pericytes into neural precursors. Together, this study elucidates the novel role of the aPKC-CBP pathway in modulating neurovascular remodeling and functional recovery following focal ischemic cortical stroke.

Contents

List of Figures

List of Abbreviations

AMPK	AMP kinase
aPKC	atypical protein kinase C
BrdU	5'-Bromo-3'-deoxyuridine
CBP	CREB binding protein
CCAO	common carotid artery occlusion
CREB	cyclic AMP response element binding protein
DCX	doublecortin
EDU	5-ethynyl-3'-deoxyuridine
eNOS	endothelial nitric oxide synthase
EPCs	endothelial progenitor cells
HATs	histone acetyl transferases
HDACs	Histone deacetylases
HDACi	Histone deacetylase inhibitors
HIF-1α	hypoxia inducible factor 1α
iNOS	inducible nitric oxide synthase
I.P	Intraperitoneal
IV rTPA	intravenous recombinant tissue plasminogen activator
L-NAME	L-N^G-Nitroarginine methyl ester
MCA	middle cerebral artery
PDGF-β	Platelet derived growth factor B
PDGFR-β	Platelet derived growth factor Receptor B
PFA	Paraformaldehyde
SGZ	sub-granular zone

SB	sodium butryrate
SOX2	(sex determining region Y)-box 2
SVZ	Sub-ventricular zone
TSA	trichostatin A
VEGF	Vascular endothelial growth factor
VPA	valproic acid

Acknowledgements

I would like to thank all those who offered both technical and emotional support throughout the past two years: Karolynn Hsu, Matthew Seegobin, and Fares Ould-Brahim, Anthony Carter, Mirela Hasu, Christine Luckhart, Dr. Baptiste Lacoste, and my supervisor Dr. Jing Wang.

To Dr. Wang, I must thank you for your consistent help and guidance and your ability as a mentor to push others beyond what they believe they can accomplish. Thank you for taking me on as your first graduate student and investing countless time and effort into my personal and professional development.

Additonally, I would like to thank my thesis advisory committee, Dr. Diance Lagace and Dr. Ruth Slack as well as my co-supervisor Dr. Bill Stanford, for pushing me to think critically about my project and goals over the last two years.

1.0 Introduction

1.1 Stroke: Pathophysiology and Epidemiology

Ischemic stroke is caused by the blockage or disruption of blood flow to a portion of the central nervous system[1]. This rapid loss of blood disrupts the exchange of oxygen and nutrients to the brain and causes cell death in a defined area, named the infarct core. The surrounding tissue, called the penumbra, becomes hypo-perfused and will die off without rapid medical intervention. Stroke often leads to neurological deficits including but not limited to motor dysfunction, aphasia, dysphagia, memory loss, and sensory dysfunction[1]. The exact prognosis, from complete rehabilitation to death, is dependent on the location and extent of the stroke, as well as factors including gender, age, co-morbidities, and time to treatment[2].

Improvements in stroke therapy and rehabilitation have failed to keep pace with the increasing incidence and severity of stroke in Canada. In Canada alone, there are more than 46,500 people hospitalized for stroke[3]. Stroke represents the number one cause of neurological disability among Canadians with a cumulative 405 000 Canadians living with the neurological deficits following stroke[3]. A vast majority of these costs, upwards of 87%, relates to the long term care of stroke patients. These numbers highlight the importance of developing novel therapeutic approaches towards stroke recovery, especially in the face of a rapidly aging Canadian population.

1.2 Stroke Treatment

During the acute phase of stroke, time to receive treatment from the onset of stroke predicts the ultimate clinical outcomes of patients. This is due to the hypoperfusion in the penumbra of

the stroke. Therefore, acute stroke treatment aims to restore blood flow and allow reperfusion back into the penumbra to halt further damage. Two types of successful acute stroke treatment are currently employed, intravenous thrombolysis and mechanical thrombectomy[4]. Intravenous thrombolysis is performed using intravenous injection of recombinant tissue plasminogen activator (IV rtPA), which enzymatically break down the blood clots. The therapeutic window for treatment with IV rtPA is quite short, only 4.5 hours from the onset of stroke [4,5].

While IV rtPA treatment is beneficial across all types of ischemic stroke, it still shows generally low levels of recanalization (10%-50% depending on the location of the occlusion) [5]. Therefore, more direct clot disruption methods, such as mechanical thrombectomy, are now approved [6-8]. The window for this treatment is generally 6-8 hours following the onset of stroke. Although acute stroke treatment continues to improve, the narrow therapeutic window will prevent large numbers of patients from receiving treatment in time.

Long-term disability following stroke is mainly manifested by motor and cognitive dysfunction, leading to the difficulty to perform normal daily tasks. Rehabilitation in the form of exercise, physiotherapy, and goal directed challenges improves the long-term outcomes of stroke patients[9]. However, rehabilitation therapies require intensive and prolonged periods of treatment that may not be suitable for many stroke patients who may be constrained by other medical conditions (e.g. frailty), motivational deficits, or by cognitive dysfunction[9]. Clearly, additional interventions will be required to produce successful recovery in many stroke patients. Understanding of molecular mechanisms that mediate the self-repair process during post-stroke recovery will provide potential therapeutic targets to enhance post-stroke recovery.

1.3 Mouse Models of Stroke

Many transgenic mice have been produced to provide tools to study the contribution of individual genes and cell types to the pathophysiology of stroke and stroke recovery. However, currently there is a lack of a single, reproducible murine model of stroke that closely mimics human clinical conditions. In order to accurately model human ischemic stroke, animal models of stroke must meet the following several criteria. First, the stroke size must be reproducible and produce an infarct volume that mirrors treatable human stroke, between 4.5-15% of the ipsilateral cortex[10]. Second, the model must emulate the types of cell damage, reperfusion, disability and inflammation observed in humans. Finally, the model must be able to produce persistent behavioural deficits. Since human stroke often has limited self-recovery, relevant amounts of spontaneous behavioural, histological and cellular recovery should appear in the animal model of stroke [11]. The most commonly used models of stroke in mice are the middle cerebral artery occlusion (MCAO), photothrombosis, and the endothelin-1 (ET-1) models.

The MCAO model of stroke uses sutures or filaments to occlude the middle cerebral artery. There are many variations in the MCAO model including transient versus permanent occlusion, distal occlusion, and three-vessel occlusion directly at the surface of the brain[11]. The MCAO model has long been used in mice due to the short surgical time, low morbidity and avoidance of any direct physical damage to the brain tissues during surgery. However, the MCAO model lacks many aspects relevant to human stroke. The model produces very large infarcts that damage deep brain structures including the hypothalamus, hippocampus, striatum, and subventricular zone (SVZ) [11-12]. The affected diverse brain structures complicate the interpretation of behavioural testing and produce surgery-related complications such as

hyperthermia. Additionally, the variation in stroke volume can be as high as five-fold even within the same cohort of mice[11]. Based on these shortcomings, recent research has focused on the use of focal ischemic stroke models.

Photothrombosis uses photo-oxidation of injected dyes such as rose-bengal to induce vascular damage and permanently disrupt blood flow to the targeted area [13]. It has been a reliable model of focal stroke in mice due to minimum surgical intervention, small clinically-relevant size, and stereotaxic determination of the infarct. These features allow for larger cohorts with more reproducible behavioural deficits, especially when used to target the well-mapped motor cortex. While photothrombosis can mimic human models of stroke, the type of damage and accompanying cellular responses may replicate traumatic brain injury more closely [14, 15]. The presence of vasogenic edema, not present in human stroke, produces vascular cell death and no reperfusion into the infarcted area, which complicates the study of vascular associated cells[16, 17, 4]. Therefore, a murine focal ischemic stroke model that allows for reperfusion and no vasogenic edema could prove to be a more clinically translatable model.

The ET-1 model of stroke uses a direct injection of the vasoconstrictive peptide endothelin-1 (ET-1) in the brain parenchyma to induce occlusion and natural reperfusion when ET-1 breaks down *in vivo*. The model has been used in rats with great success. It creates a relevant infarct size, consistent behavioural deficits, reperfusion, and allows stereotaxic determination of the infarct[18]. The only drawbacks to the procedure are the physical damage of brain tissues from the needle injections and longer surgical times. The translation of this procedure to mice has proven to be difficult. The initial study was only able to create very small infarcts with behavioural deficits that disappeared after three to five days[20]. This may be due to inter-strain

variability, and possible difference in the expression of the ET-1B receptor [21]. Activation of the ET-1B receptor counteracts the vasoconstriction of the ET-1A receptor by producing nitric oxide (NO) and resulting in vasodilation (Fig 1). More recently, an optimized ET-1 approach using three intracerebral injections into the motor cortex was demonstrated to replicate the rat model more closely [22]. However, this model was only tested on FVBN mice and it is unclear how it translates into different strains of mice.

Two studies have attempted to optimize the ET-1 model in mice by inhibiting the production of NO [20,23]. The original paper used the endothelial nitric oxide synthase (eNOS) inhibitor L-NAME along with common carotid artery occlusion (CCAO) among many different strains and had some success increasing infarct volumes. However, the use of both ET-1 and CCAO caused a high mortality rate and an inability to distinguish the usefulness of eNOS inhibition [20]. A recent study used a single injection of ET-1 and L-NAME to induce ischemia in the internal capsule. They demonstrated severe vasoconstriction shortly after injection, long-term functional deficits, and a defined infarct with circumscribed penumbra [24]. Based on these findings it appears that the addition of L-NAME to the ET-1 model may reduce the inter-species and inter-strain difference of the model and allow for a more clinically-relevant focal ischemic model in mice.

A

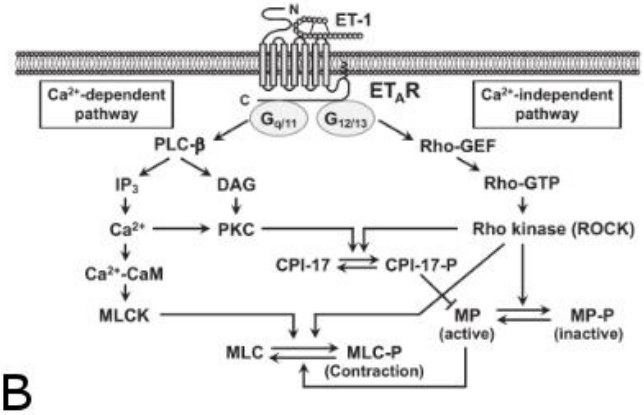
ET-1
N
C
ET_AR
Ca^{2+}-dependent pathway
Ca^{2+}-independent pathway
$G_{q/11}$
$G_{12/13}$
PLC-β
Rho-GEF
IP_3
DAG
Rho-GTP
Ca^{2+}
PKC
Rho kinase (ROCK)
Ca^{2+}-CaM
CPI-17
CPI-17-P
MLCK
MP (active)
MP-P (inactive)
MLC
MLC-P (Contraction)

B

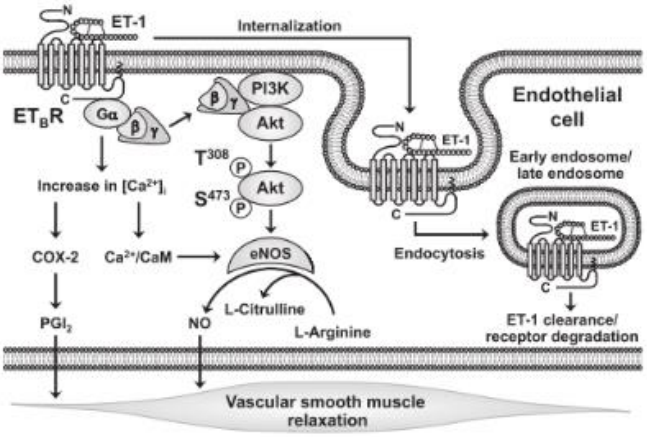
ET-1
Internalization
ET_BR
Gα
β γ
PI3K
Akt
T^{308}
S^{473}
P
Endothelial cell
Early endosome/ late endosome
Increase in $[Ca^{2+}]_i$
COX-2
Ca^{2+}/CaM
eNOS
Endocytosis
PGI_2
NO
L-Citrulline
L-Arginine
ET-1 clearance/ receptor degradation
Vascular smooth muscle relaxation

Figure 1: **Endothelin Receptor A and B signaling.** A) Activation of ET-1A receptor signaling causes the contraction of smooth muscle cells surrounding blood vessels. B) Activation of ET-1B receptor signaling releases nitric oxide, leading to vasodilative effects. Figure adapted from Wiley, K (2004)[21].

1.4 Cellular responses following ischemic stroke-related brain injury

Following stroke, natural repair processes give rise to spontaneous recovery[4]. The cellular responses involved in the recovery include: neurogenesis, the production of new neurons, and angiogenesis, the production of new blood vessles[25]. These cellular changes arise in response to the microenvironmental cues released from stroke injury sites, leading to cellular growth, differentiation, migration, and maturation. This spontaneous recovery often reaches the plateau, which leaves long-term disability for stroke patients. Therefore, if we can understand how the signaling-induced molecular processes are involved in the endogenous repair processes, we may identify valid therapeutic targets to enhance the post-stroke recovery.

Neurogenesis is the process that gives rise to newborn neurons. Continuous neurogenesis throughout adulthood mainly takes place in the two regions of adult brain, the SVZ of the lateral ventricle and the hippocampal subgranular zone (SGZ) [26,27]. The newborn neurons produced in the hippocampal SGZ play a key role in learning and memory, while newborn neurons produced in the SVZ migrate through the rostral migratory stream to the olfactory bulb and participate in sensory function of the olfactory bulb [28]. Recently, carbon-14 dating the birth of human neurons showed conclusive evidence of neurogenesis in humans [29]. The major difference between human and rodent neurogenesis appears to be the final destination of neuronal maturation. In rodents, most neuroblasts from the SVZ migrate to the olfactory bulb. Whereas in humans, the main area for maturation appears to be the striatum[30,31].

In both rodents and humans, glia-like adult neural stem cells residing in the SVZ and SGZ neurogenic regions possess both self-renewal and multipotency[24] and express markers such as

Nestin, glial fibrillary acidic protein, and Sox2. These cells give rise to transiently amplifying cells, which downregulate multipotent markers such as Sox2, and differentiate into neuroblasts[24] Neuroblasts are proliferative and migratory immature neurons and express functional markers such as doublecortin (DCX) and the cellular adhesion protein PSA-NCAM. Subsequently, neuroblasts mature into post-mitotic neurons that integrate into neural circuits over a period of 6-8 weeks[24] and express mature neuron markers, such as NeuN, calretinin, and relevant neurotransmitter receptors.

The discovery of endogenous adult neural stem cells opens the door for the therapeutic application of these cells to replace lost neural cells in order to treat the injured brain following stroke. Indeed, the proliferation of neural stem cells in the SVZ is increased and these SVZ neural stem cells ectopically migrate towards the lesion site in response to stroke-related injury[31]. In addition, recent studies indicate that ischemic stroke-induced neural stem cells may also be derived from other local cell sources, such as reactive astrocytes and pericytes around the injury site [32-33]. These recruitments represent an attempt at endogenous repair. However, this level of endogenous repair is often not sufficient to recover perturbed brain function, since only a small percentage of neural stem cells and their progeny will survive and integrate into neural circuits[34-36]. A few studies have shown that functional motor and cognitive recovery after stroke can be enhanced by increasing the level of post-stroke neurogenesis, while inhibited when newly born neurons are genetically ablated[37-40]. This correlation between the level of stroke functional recovery and the extent of post-stroke neurogenesis provides strong support for the development of novel regenerative strategies to treat stroke-related brain injury. Despite these findings, it remains controversial about the relevance of neurogenesis to clinical

application in stroke recovery due to the lack of translation over the past decade, as well as recent findings that human neuroblasts do not give rise to mature neurons at the site of cortical stroke[41]. To date, it remains unclear as to the exact causative nature of neurogenesis to stroke recovery, and the translational ability of rodent neurogenesis to humans.

It is possible that the translation of post-stroke neurogenesis to stroke recovery requires vascular support. Newborn and integrating neurons must receive trophic support and microenvironmental signals from nearby cells in a neurovascular niche [42]. The neurovascular niche is comprised of neurons, astrocytes, endothelial cells, and pericytes in a well-defined spatial organization. Since stroke damages the vasculature, which supports the neurovascular niche, it is imperative to promote the growth of new blood vessels and associate them with damaged or newborn cells in the penumbra area in order to prevent the spread of the ischemic core during the post-stroke recovery[43]. The growth of new blood vessels can be derived from two regenerative processes, angiogenesis and vasculogenesis, which together form vascular remodeling. Angiogenesis is the reorganization or growth of new vasculature from locally present endothelial cells. This process leads to the extension or widening of existing vasculature[43]. Vasculogenesis refers to the new blood vessels that are generated from bone marrow derived endothelial progenitor cells (EPCs). Angiogenesis produces sprouting from existing blood vessels and grows into hypoperfused areas [43]. Vascular remodeling begins within 24 hours after the onset of stroke and plays an integral part in stroke recovery [44].

Vascular remodeling contributes in multiple ways to post-stroke recovery. In early stages, it increases vascular support to the fragile penumbral area, thereby reducing the spread of the infarct core. For example, an increase in the sprouting of microvessels in the periinfarct

reduced apoptosis and decreased the eventual infarct size[45-46]. Over the intermediate term, it acts as physical scaffolding for the migration of both immune cells as well as migrating neuroblasts. For example, the systemic administration of endostatin, a potent angiogenic inhibitor, abolished neuroblast migration from the SVZ towards the periinfarct area in a rodent model of stroke[47]. Finally, new vasculature acts as the coordinator and physical basis for the neurovascular niche. The importance of vascular remodeling post-stroke is better defined than that of neurogenesis. In rodents, there is strong evidence that increased vascular remodeling contributes to reduced infarct size and greater functional recovery [44,45]. This underscores vascular remodeling as an important target for therapeutic treatment, which may reduce short-term damage.

1.5 Epigenetic regulation of Post-Stroke Recovery and Cellular Responses

Following ischemic stroke, rapid and robust changes in gene expression occur in all cell types of the central nervous system. Most of these gene changes are driven by epigenetic modifications that alter DNA organization and accessibility, allowing concerted and directed efforts to limit the spread of damage and mount a reparative and regenerative response [48]. Histone acetylation is one of many epigenetic modifications that are altered following stroke. The acetylation of histone lysine residues are regulated by two enzymes, histone acetyl transferases (HATs) and histone deacetylases (HDACs).

HATs and HDACs both contain a wide variety of isoforms in order to fine tune histone acetylation upon the activation of environmental cues. HDACs contain 11 major isoforms, splitting into four families. Three of these families are dependent on zinc for catalytic reactions

and consist of class 1 (HDAC 1, 3, and 8), class 2 (HDAC 4,5,6,7, and 9), and class 4 (HDAC 11). Class 3 HDACs, termed sirtuins, rely on nicotinamide adenine dinucleotide substrate to catalyze histone deacetylation[48]. HATs fall into four major families consisting of GNAT, MYST, P300/ CREB binding Protein(CBP) and SRCs. Of these, the CBP/P300 family is the best studied in relation to stroke [48]. In addition to its histone acetylation function, HATs serve as scaffolding proteins to physically bridge specific transcription factors to general transcriptional machinery. They acetylate other non-histone proteins to regulate their function as well [49].

Following stroke, widespread transcriptional repression occurs within the ischemic core and penumbra[50,51]. This is marked by a dramatic drop in histone acetylation level caused by a combination of increased HDAC activity and decreased HAT activity 50,[51]. In a rat MCAO model of stroke, HDAC expression is rapidly upregulated and sustained in the periinfarct [52,53]. Two common HDAC inhibitors (HDACi), trichostatin A (TSA) and valproic acid (VPA), block the activity of HDAC classes 1, 2 and 4 and have been shown to reduce infarct volume and neurologic deficits when given in the rat model of MCAO stroke [50-52]. Their neuroprotection is driven by the expression of anti-inflammation and pro-angiogenic factors.

HAT activity is thought to be greatly reduced following stroke, possibly through metabolic limitations[50]. Following ischemia, the availability of acetyl-CoA drops as aerobic metabolism is unable to proceed. Without a readily available source of acetyl-CoA, HATs are unable to reverse the changes induced by high HDAC activity, which could produce lethally low levels of transcription for the cells in the penumbra [53-56]. Additionally, CBP and P300 are essential for the transactivation of hypoxia inducible factor -1α (HIF-1α), which subsequently increases the transcription of proteins that are important in surviving from ischemic insult. However, it

remains controversial whether HAT activity is actually decreased post-stroke [57]. The involvement of histone acetylation in the acute phase of stroke injury is well studied[53-56]. Until recently, a couple of studies using HDACi treatment suggest participation of histone acetylation during post-stroke recovery. In a juvenile murine MCAO stroke model, TSA and VPA both increase SGZ neurogenesis and improve neurological outcomes in memory and motor testing[54]. An additional study using adult murine MCAO model found that VPA treatment increases neurogenesis in the periinfarct, associated with increased histone 4 acetylation[58]. Another comprehensive study using sodium butryrate (SB), a potent HDACi, showed that SB increases the proliferation of neural precursors in the SVZ, SGZ, striatum, and cortex, as well as enhances the population of newborn neurons and nestin expressing cells in the periinfarct [56]. These findings suggest that increased histone acetylation could promote neural cell genesis, consequently enhancing the regenerative capacity of the damaged brain. Since histone deacetylase pan-inhibitors are compounds with a wide spectrum of functions, their clinical use is of limited viability. Therefore, it is important to understand the underlying molecular mechanisms that could be targeted therapeutically to regulate histone acetylation and promote brain repair and stroke recovery.

The contribution of histone acetylation to angiogenesis is well studied outside of the context of stroke. Silencing or inhibition of specific HDAC isoforms leads to pro-angiogenic effects by increasing expression of fibroblast growth factor, Platelet-derived growth factor β (PDGF-β), PDGF-β receptor (PDGFR-β), VEGF as well as promoting migration of EPCs, sprouting of microvessels and proliferation of pericytes [59-63]. A recent study from the rat MCAO model showed that VPA treatment following stroke increases blood vessel density in the periinfarct

region and improves global cerebral blood flow. This was associated with increased expression of pro-angiogenic proteins VEGF, matrix metalloproteinase 2 and 9, and the transcription factor HIF-1α in the periinfarct region [64].Therefore, it is possible that histone acetylation plays an important role in post-stroke vascular remodeling.

1.6 aPKC-CBP Signaling

To date, most research work investigating the role of histone acetylation has focused on the role of HDACs due to the simplicity of using small molecules to inhibit HDAC activity. Very little work has focused on HATs and their role in post-stroke recovery during the chronic phase. Of the limited work that has been done, it is evident that P300/CBP family plays a key role in ischemic resistance [65]. The repression of p300/CBP by HDAC 1 and 2 leads to reduced ischemic resistance to stroke-related brain damage [66]. While these findings focus on the role of CBP/p300 during the acute phase of ischemic stroke, it remains largely unknown regarding its involvement in brain regeneration and recovery during the chronic phase of stroke. Given the important role of histone acetylation in neurogenesis and vascular remodeling, it will be interesting to elucidate its contribution to post-stroke regeneration and recovery.

CBP acts as a transcriptional co-activator, interacting with a wide variety of transcription factors including NF-KB, CREB, retinoic acid receptor alpha, p53 and AP-1[67]. CBP-mediated transcription controls many cellular processes including differentiation and maturation. When CBP is haploinsufficient in humans, it causes the genetic disorder Rubinstein-Taybi syndrome (RTS), characterized by severe cognitive disabilities along with facial abnormalities [68, 69]. This cognitive dysfunction in RTS has been causally linked to deficits in developmental neurogenesis due to

CBP haploinsuficiency [70]. Moreover, CBP phosphorylation at Ser436 by aPKCζ was necessary for CBP to regulate the differentiation of neural precursors through activating histone acetylation at neural gene promoters. The activation of the aPKC-CBP pathway by metformin, a FDA-approved drug and AMPK (adenosine monophosphate kinase) activator, has been shown to enhance adult neurogenesis and improve spatial memory [71]. Recent work from our lab (as a co-first author, appendix A) shows that the aPKC-CBP pathway regulates adult hippocampal neurogenesis and hippocampal-dependent memory in an age-dependent manner, supporting the concept that the aPKC-CBP pathway is a homeostatic signaling that maintains homeostatic adult neurogenesis, which is required for increased memory as mice age[72].

Interestingly, CBP is also involved in the process of angiogenesis. CBP is required for both thrombin- and mechanical shear force- induced angiogenesis [72,73]. It also regulates the cell cycle and differentiation of endothelial progenitor cells through interaction with HIF-1α [72]. Additionally, mice carrying a truncated form of CBP show severe developmental deficits in vasculogenesis and angiogenesis, resulting in embryonic lethality [74]. While CBP is important to angiogenic signaling, it remains to be determined whether aPKC-CBP pathway is involved in post-stroke angiogenesis and recovery.

Following the initial discovery that metformin can enhance adult neurogenesis and improve spatial memory, several groups have assessed the therapeutic potential of metformin treatment on animal models of stroke in the past two years[75-79]. They found that chronic metformin treatment improves stroke functional recovery, associated with increased neurogenesis[77, 79] and angiogenesis [76,77,]. While the beneficial effects of metformin in stroke recovery are evident, the underlying molecular mechanisms remained to be determined. In this

regard, it is important to delineate the role of the aPKC-CBP pathway, the metformin-induced epigenetic pathway, in post-stroke neurogenesis, angiogenesis, and functional recovery.

1.7 Objectives and Hypothesis

The objective of this study was to determine the role of the aPKC-CBP pathway in neurogenesis, angiogenesis and functional recovery following sensorimotor cortical stroke using the CBPS436A Knock-in (KI-CBPS436A) mouse.

The four aims of the study were:

Aim 1: Optimize and confirm the ET-1 focal ischemic stroke model in our transgenic mouse line.

Aim 2: Determine whether the aPKC-CBP pathway regulates stroke infarct sizes and functional recovery following ET-1 cortical stroke.

Aim 3: Investigate the role of the aPKC-CBP pathway in the modulation of post-stroke neurogenesis following ET-1 cortical stroke.

Aim 4: Investigate the role of the aPKC-CBP pathway in the modulation of post-stroke angiogenesis following ET-1 cortical stroke.

Hypothesis:

I hypothesize that the aPKC-CBP pathway mediates the intrinsic self-repair and recovery following focal ischemic ET-1 stroke through modulating neurovascular remodeling.

2.0 Methods and Materials

2.1 Animals and drug treatment

All animal use was approved by the Animal Care Committees of the University of Ottawa in accordance with the Canadian Council of Animal Care policies. A transgenic mouse line CBPS436A was maintained on a 12 h light/12 h dark cycle with *ad libitum* access to food and water. Heterozygous CBPS436A were used for breeding to produce littermates of WT and KI-CBPS436A for the experiments. The transgenic CBPS436A mouse line was obtained from the laboratory of Dr. Fredric Wondisford at John Hopkins University (Baltimore, MD).

2.2 ET-1 Surgery

Mice from the CBPS436A genetic background between the ages of 2-4 months were anesthetized using 4-5% isoflurane and 1.5% oxygen and mounted to a stereotaxic frame. Injections were performed using a Hamilton 10uL gastight syringe with a 0.49mm diameter needle (Hamilton Robotics, Reno NV, 7653-01). Injections of saline, ET-1 (Abcam, Cambridge, UK, AB120471) (2 µg/ µl) alone, or ET-1 (2 µg/ µl) + L-N^G-Nitroarginine methyl ester (L-NAME) (Sigma-Aldrich, St. Louis MS, N5751) (2.7 µg/ µl) were performed at +0.0mm anterior-posterior (AP), -1.0mm Medial-Lateral (ML), -1.3mm Dorsal-Ventral (DV); +0.2AP, -1.0ML, -1.4DV; and +0.4AP, -1.0ML, -1.6DV. ET-1 and L-NAME were dissolved in PBS and sonicated in a 4^{o}C water bath for 15 minutes before use. The injection was performed at 0.2 µL/minute for 5 minutes per site for a total of 1µL/injection. Upon needle insertion, a one-minute waiting time was used to allow for settling of tissue. Following injection, a three-minute waiting time before needle removal was used to reduce back-flow. Body temperatures were continually monitored and

maintained at 37°C during surgery using a heating pad and anal thermometer. Local Bupivacaine and subcutaneous buprenorphine were administered post-surgery and 4 hours later. Approximate surgery time was 50 minutes per mouse.

2.3 5-ethynyl-2'-deoxyuridine (EdU)/5-bromo-2'-deoxyuridine (BrdU) Injections

To label dividing cells, mice received an intraperitoneal injection (I.P) with 50mg/kg EdU (Cedarlane, Burlington, ON, AB16186) prepared in sterile PBS using a 25-guage needle. Injections were performed once a day from 2-5 days post-stroke for a total of four injections.

A separate cohort of mice received I.P injections with 100mg/kg BrdU (Sigma-Aldrich, B9285) prepared in sterile PBS using a 25-guage needle. Injections were performed beginning 24 hours before surgery and were repeated four times, once every three hours.

2.4 Tissue Preparation

At 3 or 14 days post-surgery, mice were anesthetized by an I.P injection of 0.1µl of 65mg/ml sodium pentobarbital. The mice were transcardially perfused with 35 mL of 4°C PBS (7ml/min for 5 minutes) followed by 70mL (7mL/min for 10 minutes) of 4°C 4% Paraformaldehyde (PFA) (Sigma-Aldrich, 1518127) in PBS. Then the brains were removed and transferred to 4% PFA for 24 hours, followed by a dehydration step using cold 30% sucrose solution containing 0.1% sodium azide (Fisher, Toronto ON 19038-1000) for 48 hours. Samples were flash frozen over dry ice in optimal cutting temperature solution (VWR, Randor PN, 25608-930). All samples were cut in a CRYOSTAT (Leica Biosystems, Buffalo Grove IL, CM1850) at 20 µm. Serial sections were mounted on 10 glass slides. Sections were stored at -80°C until needed.

Samples that were stained for CD31 or PDGFR β were perfused with PBS, followed by immediate dissection and snap freezing in 100% ethanol cooled with dry ice. Samples were cut in the same way as mentioned above, and fixed with acetone in room temperature immediately following collection of cut sections. The slides were allowed to dry and were stored at -80°C until needed.

2.5 Immunostaining

The sections were defrosted at 37°C for 15 minutes. For PFA perfused sections, Two 5-minute washes with PBS were performed before 15-minute fixation with 4°C 4% PFA. For acetone fixed sections; the sections were directly fixed with -20°C acetone for 15 min and dehydrated with -20°C 100% ethanol. Three 5-minute washes with PBS were performed on all slides sections before proceeding to the permeabilisation/blocking step.

One hour incubation with 10% goat serum (Jackson Immunoresearch, West Grove PA, 008-000-121) (horse serum if primary antibody was produced in a goat) containing 0.3% triton x-100 in PBS was performed to slides to permeabilize and block the brain sections. Samples to be labelled for BrdU were treated with 2N HCL at 45°C for 20 minutes and then rinsed with borate buffer solution (pH=8.0) prior to permeabilization/blocking step. Brain sections were then incubated with the primary antibody in 10% goat serum containing 0.3% triton x-100 in PBS at 4 °C overnight. Antibodies used were: rat anti-CD31 (1:200) (BD Pharminogen, Franklin Lake, NJ, 550274), rat anti-BrdU (1:200) (AbD Serotec, Oxford UK, OBTOO30G), rabbit anti-Sox2 (1:200) (Millipore, Billiereca MA, 49005), goat anti-DCX (1:200) (Santa Cruz Biotechnologies, Dallas TX,

sc-8066), rabbit anti-PDGFR-β (1:100) (Santa Cruz Biotechnologies, sc-1627), mouse anti-NeuN (1:500) (Millipore, Mab377).

Following overnight incubation, three 5-minute PBS washes were performed before addition of the Alexa fluora conjugated secondary antibody (Cell Signaling Technologies) diluted in PBS with 0.3% triton x-100 (Fisher, 9002-93-1) for one hour. Immediately after the secondary antibody incubation, brain sections were counterstained with Hoechst 33342 stain (New England Biotech, Ipswich MA, 40825) at 1ug/mL in PBS for 3 minutes followed by three 5-minute washes with PBS. Permafluor solution (ThermoFisher, TA-030-FM) was used to mount the slides, which were imaged after drying for 24 hours.

2.6 Three Dimensional (3-D) Blood Vessel Staining, Imaging and Quantification

At 25 days post-surgery mice were anesthetized as described above and killed by cervical dislocation. The cortices were dissected, flattened between two layers of glass and immersed in 4% PFA overnight at 4^{o}C. The brains were then removed from between the glass and washed with PBS, and then embedded in 2% agarose in PBS. The cortices were then cut tangentially into 120µm sections using a vibratome (Leica WT1000S). Sections were blocked with 10% horse serum, permeabilized with 0.2% tritonx100 and 0.5% fish gelatin followed by overnight incubation with rat anti-CD31 (BD Pharminogen 550274, 1:200). The sections were then rinsed in PBS and incubated for two hours in anti-rat Alexa fluor 488 conjugated antibodies (Jackson Immunoresearch, 1:300). Slides were then mounted with fluoromount G and visualized using fluorescent confocal microscopy (LSM510/Axioimager.M1, Zeiss). Z-Stacks between 60-80µm were obtained. Stacks were obtained at 10x magnification on a Zeiss LSM510/AxioImager M.1.

Two images per hemisphere per section for three sections were captured and outsourced for computational analysis of vasculature length and branch points using Python 2.7 as described in Lacoste B et al. 2014[80]

2.7 Imaging and Quantifications

Digital image acquisition was performed using either a Zeiss Axioplan 2 fluorescent microscope with Zeiss Axiovision software that contains z-axis capability, or a Zeiss LSM 510 confocal microscope using Zeiss Zen Pro software V2.0 (Oberkochen, Germany). 10-15 images were captured in the Z-axis per section at a maximum of 1 µm apart and processed as an optical stack of 10-15 scanned slices for quantification.

For quantification, positive cells in the peri-infarct/infarct region were quantified using imageJ software (National Institute of Health, Bethesda MD). Images were obtained at 20x magnification. Three images per section for 6-10 sections were quantified, dependent on the extent of the stroke and presence of immunoreactive cells. Cell counts in the periinfarct were measured as labelled cells per area. The identity of cells was confirmed using Hoechst as a counterstain.

Particle analysis for vascular coverage was performed using ImageJ. The auto threshold function was used in conjunction with particle analysis for area coverage. Particles below 5 pixels were excluded from analysis for area coverage.

2.8 EdU Click-it Chemistry Labelling

EdU was visualized using the click-it chemical reaction kits from Cell Signaling (C10338) according to commercial instructions. Briefly, the components were combined in the suggested

ratio and sequential order and were applied to the sections for 20 minutes, following fixation. The Click-it reaction solution was washed with three 5-minute PBS washes before permeabilization/blocking mentioned as described above.

2.9 Horizontal Ladder Test

Mice were placed at the beginning of a horizontal ladder consisting of two plexiglass walls and irregularly placed metal bars across from their home cage. The home cage was placed at the end of the ladder. The mice were videotaped crossing the bar from slightly below in order to have full view of all four limbs. Five trials per day were videotaped and only trials in which mice made clear, uninterrupted movement across the ladder were later analyzed. The mice were given one day of pre-training and one day of baseline measurements prior to surgery. Mice were re-tested at 7 and 14 days post-stroke. The videos were later analyzed in a blinded fashion using VLC media player at a reduced speed. Steps in which the mice slipped on or missed a bar, or the use of the wall to support their weight, were counted as an error. The percentage of steps containing an error was reported. Data for forelimb errors is reported.

2.10 Cylinder Test

Mice were placed in a clear plastic cylinder under red light and were videotaped from above for the time it took for the mice to perform twenty rears. One pre-surgery baseline value was obtained and the mice were re-tested at 7 and 14 days post-stroke. The videos were later analyzed frame-by-frame in VLC media player (Version 2.2.3). The total number of ipsilateral, contralateral, and double paw touches against the cylinder wall was counted. The percentage ipsilateral preference was calculated as:

(total ipsilateral paw touches – contralateral paw touches) *100) / total paw touches

2.11 Adhesive Tape Test

Prior to testing, the home cage of the mouse was emptied of bedding, food, and water. One researcher held the mice while a second placed 1cm^2 pieces of tape on each forepaw. Once the mice were placed back into their home cage, the time to contact and the time to remove the tape for each paw were measured in real time by both researchers. The mice were pre-trained on the task for 4 days with 1 trial per day to reach a plateau in contact and removal time. The final day was taken as the baseline time for each mouse. The test was performed again at 7 and 14 days post-stroke. The mice were allowed to habituate to the environment for 30 minutes prior to testing in order to reduce freezing associated with anxiety and fear. The data is reported as fold-change over the average of the last two days of pre-training.

2.12 Cresyl Violet Staining

Slides containing serially collected sections were dried at 37°C for 15 minutes. The slides were then submerged in cresyl violet solution (Sigma-Aldrich, C5402) (0.2% cresyl violet dissolved in 0.5% acetic acid solution, pH = 3.5) for 20 minutes. Sequential washes in 70%, 95% and 100% ethanol were performed before clearance with citrosolv (Fisher, 22-143-975) clearing agent. The slides were mounted with permount solution and placed on a 37°C slide warmer to dry overnight.

2.13 Infarct volume Measurement

Cresyl violet images were captured using an Aperio digital pathology slide scanner (Leica Biosystems) and analyzed using Image J. To calculate infarct volume, the infarct area was analyzed every tenth 20-µm section and the infarct volume were calculated using following formula below:

(total area of infarct * 20 (section thickness) * 10 (serial collection factor)) = infarct volume

2.14 Statistical Analysis

Data analysis was performed using GraphPad Prism 6 (Graphpad Software, La Jolla CA). Behavioural analysis was performed using either one-way ANOVA with Dunnet's post-hoc test or two-way ANOVA with Tukey's post-hoc test. Single comparisons were performed using two-tailed Student's T-test. Alpha = 0.05 for all tests performed.

3.0 Results

3.1 The injection of ET-1 + L-NAME induces ischemic brain damage in the mouse sensorimotor cortex

In order to study the contribution of the aPKC-CBP pathway on stroke recovery, a viable model of focal cortical stroke had to be optimized. The ET-1 model of stroke is well validated in rats but shows large variability in mice, often in a strain dependent manner[20]. Higher expression of the ET-1B receptor leads to production of the vasodilative nitric oxide (NO) in the mouse brain. This has been thought to be one of reasons for different responses of rats and mice to ET-1 injections [21] (Fig 1). Therefore, to optimize a mouse ET-1 stroke model, I used the nitric oxide synthase inhibitor L-NAME to block the vasodilative effects of the ET-1B receptor. Three stereotaxic injections of saline, ET-1, or ET-1 + L-NAME into the sensorimotor cortex were performed and the mice were sacrificed 3 or 14 days later. Histological analysis using cresyl violet stain showed that only ET-1 + L-NAME produced significantly increased infarct volume over saline injections at both 3 and 14 days (Fig 2). These results indicate that blockage of nitric oxide production is necessary for the production of consistent ischemic brain damage in the CBPS436A mouse line.

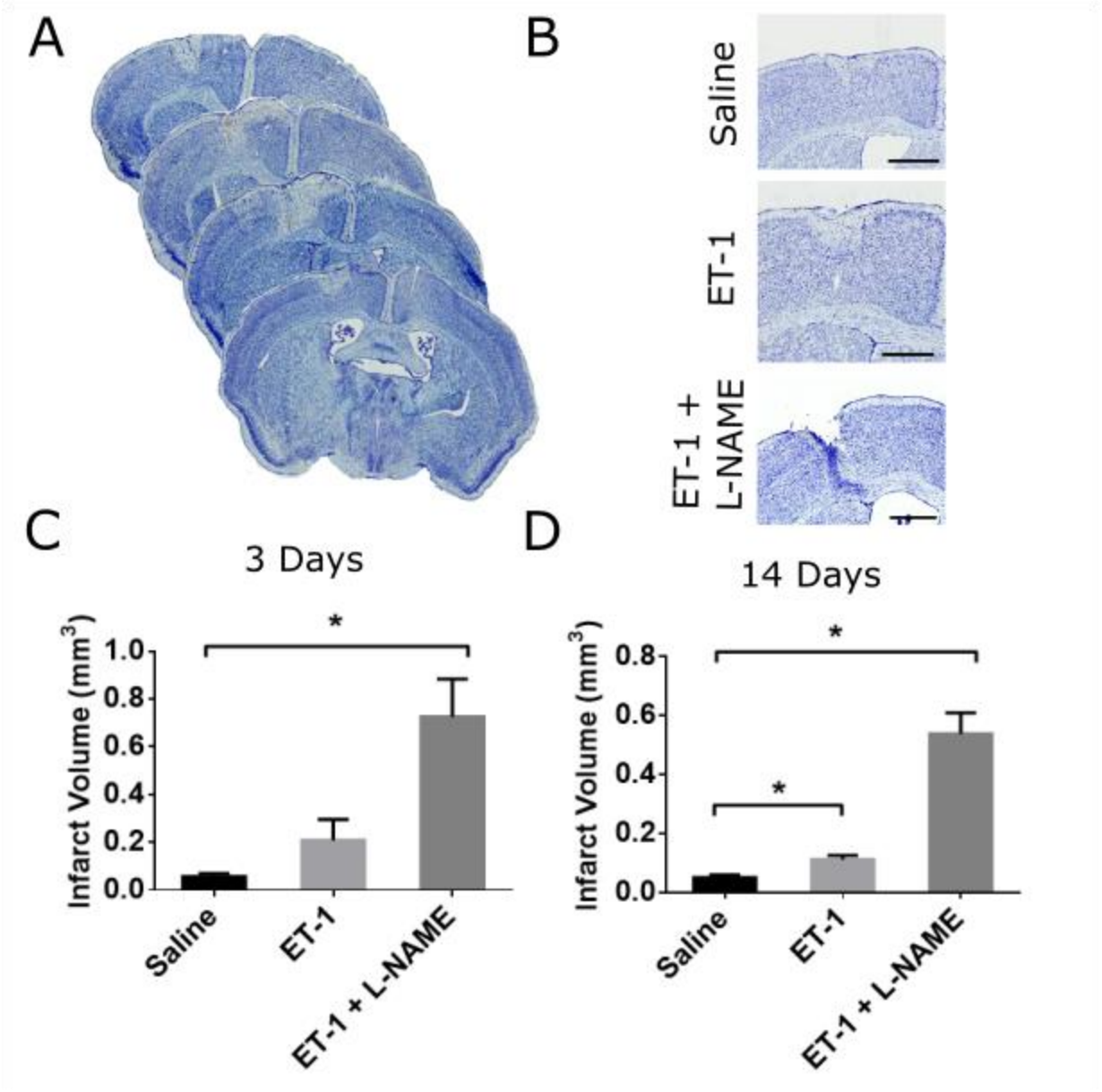
A
B
Saline
ET-1
ET-1 +
L-NAME
C
3 Days
Infarct Volume (mm3)
1.0
0.8
0.6
0.4
0.2
0.0
*
Saline
ET-1
ET-1 + L-NAME
D
14 Days
Infarct Volume (mm3)
0.8
0.6
0.4
0.2
0.0
*
*
Saline
ET-1
ET-1 + L-NAME

Figure 2: **A comparison of infarct volumes produced by ET-1 injections alone and ET-1/ L-NAME co-injections**. (A) Cresyl violet staining from the wild type brain 3 days following ET-1/L-NAME co-injections, captured using an Aperio digital pathology slide scanner from sections. (B-C) Quantification of infarct volumes using cresyl violet staining at 3 days (C) and 14 days (D) post-stroke in saline, ET-1, and ET-1/L-NAME injections. Data was analyzed by one way ANOVA (3 days: $F(2,14) = 7.528$, $P = 0.006$, n= 3 (saline), 7 (ET-1), 9 (ET-1+L-NAME). 14 Days: $F(2,18) = 24.60$, $P = 0.0001$, n = 3 (saline), 8 (ET-1), 9 (ET-1+L-NAME)) with Dunnets post-hoc test in comparison to saline injection (* $p < 0.05$).

3.2 ET-1/L-NAME co-injection causes forepaw motor impairment

The stereotaxic injection of ET-1 + L-NAME induces focal ischemia in the sensorimotor cortex. This localization is useful to study specific motor outcomes post-stroke. In order to determine if the co-injection of ET-1 and L-NAME is capable of producing consistent motor deficits, three behavioral tests were used. The adhesive tape test for sensorimotor function and motor skill; the horizontal ladder test for gross motor function and weight bearing; and the cylinder test for spontaneous motor function [81]. The mice were tested at 7 and 14 days post-stroke in order to investigate both initial deficits and short-term recovery.

The adhesive tape test is used to measure sensorimotor function. Fine motor abilities determine the capability of mice to remove tape from both the contralateral and ipsilateral forelimbs. It is a reliable test for assessing post-stroke motor deficits in mice [82]. The mice were pre-trained for four days to reach a plateau in both time to contact and time to remove the tape (Fig 3. A, B). ET-1 and ET-1/L-NAME injections cause a slight increase (2-3 fold over baseline) in time to contact and remove the tape (Fig 3. C, D) at day 7, and these deficits were totally recovered at day 14, suggesting that the adhesive test is not sensitive to capture persistent behavioral deficits induced by ET-1 and ET-1/L-NAME injections.

The horizontal ladder test was used to determine gross motor function. The mice were placed across a horizontal ladder with irregularly spaced rungs from their home cage and were allowed to spontaneously traverse it. The amount of errors made, including slips, misses, and the use of the walls to support their weight were counted and the percentage of steps containing an error was recorded.

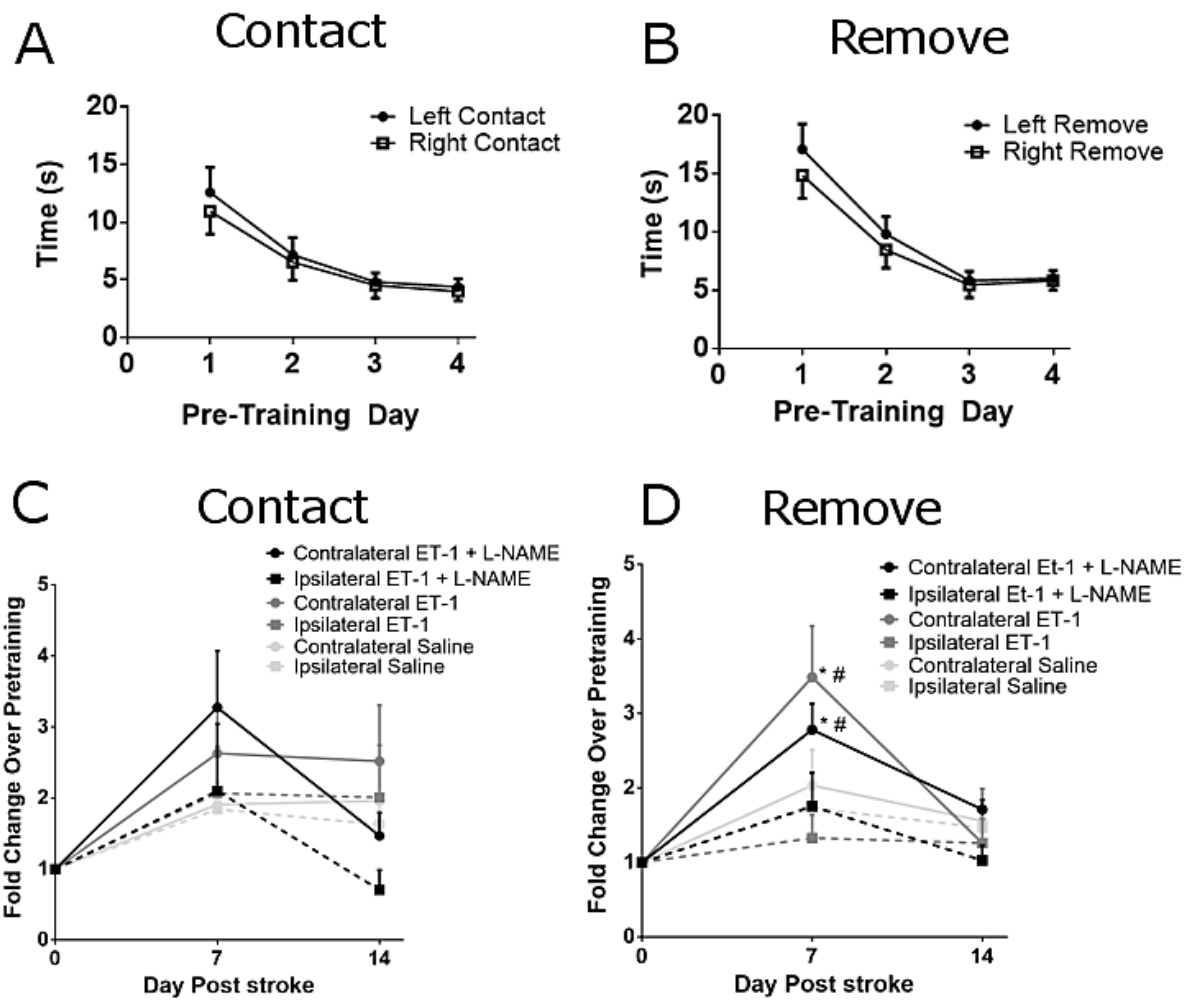
A
Contact
Left Contact
Right Contact
Time (s)
Pre-Training Day
B
Remove
Left Remove
Right Remove
Time (s)
Pre-Training Day
C
Contact
Contralateral ET-1 + L-NAME
Ipsilateral ET-1 + L-NAME
Contralateral ET-1
Ipsilateral ET-1
Contralateral Saline
Ipsilateral Saline
Fold Change Over Pretraining
Day Post stroke
D
Remove
Contralateral Et-1 + L-NAME
Ipsilateral Et-1 + L-NAME
Contralateral ET-1
Ipsilateral ET-1
Contralateral Saline
Ipsilateral Saline
* #
* #
Fold Change Over Pretraining
Day Post stroke

Figure 3: **Adhesive tape test to measure sensorimotor deficit following saline, ET-1, and ET-1/L-NAME injections.** (A-B) Pre-training data showing (A) time to contact and (B) time to remove the adhesive tape for four consecutive days. (C) Time to contact and (D) time to remove the tape at 7 and 14 days post-stroke. Data presented as fold changes over pre-training time (day 0). Data was analyzed by two-way ANOVA (for Contact, Treatment x Testing day $F(10,60) = 0.533$ $P=0.86$, testing day $f(2,60) = 6.240$ $p=0.004$, Treatment $F(5,60) = 0.5831$ $P=0.7127$, n =7 per group. For Remove, Treatment x Testing day $F(10,60) = 1.454$ $P=0.1837$, testing day $F(2,52)=14.64$ $P=0.001$, Treatment $F(5,52) = 1.757$, n=7 per group) with Tukey's post-hoc test (* $p < 0.05$ over contralateral saline # $p < 0.05$ over pre-stroke baseline).

ET-1/L-NAME co-injection method showed significantly higher deficits at 7 and 14 days compared to injection of ET-1 or saline alone (Fig 4A). While the horizontal ladder was able to measure the increased motor deficits correlating to an increase in infarct volume, the test did not show asymmetrical difference between contralateral and ipsilateral forelimbs and hindlimbs.

To test the asymmetrical difference post-stroke, the cylinder test for spontaneous weight bearing was used in ET-1/L-NAME co-injected group. The total amounts of contacts for each paw when rearing up and contacting the inside of a clear cylinder were counted. Using this test an asymmetrical deficit was found at both 7 and 14 days post-injection of ET-1/ L-NAME (Fig 4B). Therefore, the combination of the horizontal ladder test with the cylinder test allows for the analysis of gross motor deficits and asymmetrical deficits, respectively.

3.3 ET-1 + L-NAME model of focal ischemic stroke induces robust neurogenic response

The proliferation and migration of neuroblasts from the SVZ is an endogenous response to ischemic stroke[36]. Therefore, we sought to determine if our ET-1/L-NAME co-injection increased the neurogenic response when compared to ET-1 or saline injections. Total counts of DCX^+ neuroblasts within the peri-infarct of the ipsilateral cortex were performed. The ET-1/L-NAME co-injection was found to greatly increase the amount of neuroblasts at 14 days post-stroke when compared to ET-1 alone or saline (Fig 5). These results allowed us to confirm that the expected post-stroke neurogenesis occurs in our model. Based on these findings we used the ET-1/L-NAME model of stroke for our future experiments.

A

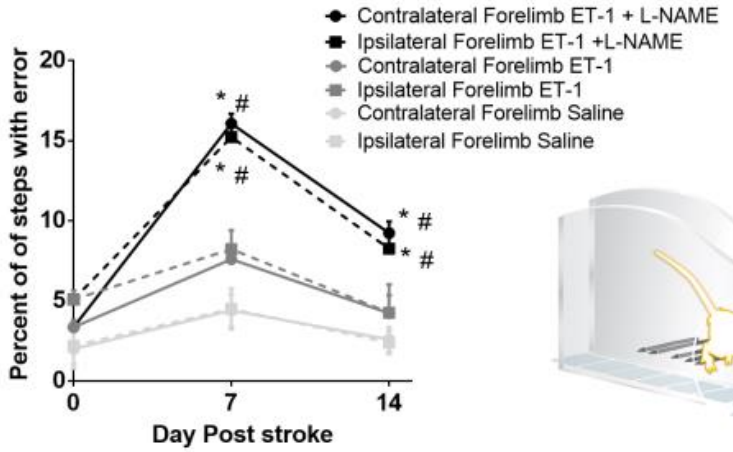
Contralateral Forelimb ET-1 + L-NAME
Ipsilateral Forelimb ET-1 +L-NAME
Contralateral Forelimb ET-1
Ipsilateral Forelimb ET-1
Contralateral Forelimb Saline
Ipsilateral Forelimb Saline
Percent of of steps with error
20
15
10
5
0
0
7
14
Day Post stroke
* #
* #
* #
* #

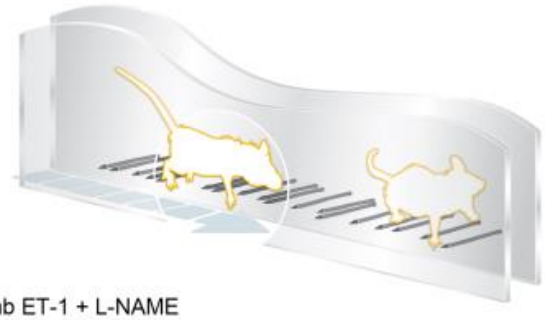

B

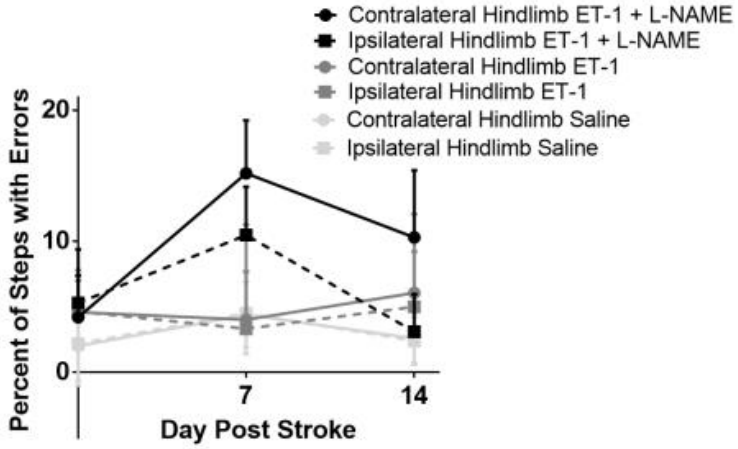
Contralateral Hindlimb ET-1 + L-NAME
Ipsilateral Hindlimb ET-1 + L-NAME
Contralateral Hindlimb ET-1
Ipsilateral Hindlimb ET-1
Contralateral Hindlimb Saline
Ipsilateral Hindlimb Saline
Percent of Steps with Errors
20
10
0
7
14
Day Post Stroke

C

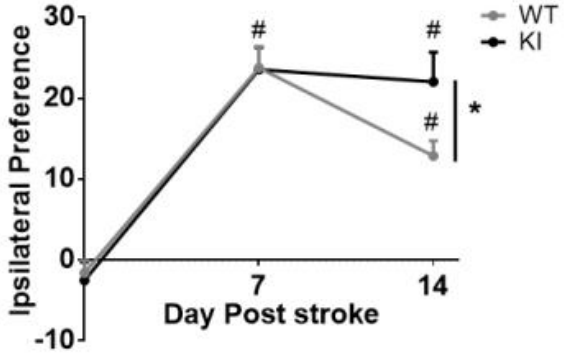
WT
KI
Ipsilateral Preference
30
20
10
0
-10
7
14
Day Post stroke
#
#
#
*


c iStock

Figure 4: **Horizontal ladder and cylinder tests to measure motor deficits after saline, ET-1, or ET-1/L-NAME injections**. (A) Percentage of Forelimb steps containing errors in the horizontal ladder test at 7 and 14 days post-stroke. Data was analyzed by two-way ANOVA(Treatment x Testing day $F(10,60) = 0.5330$ $P=0.86$, testing day $f(2,60) = 40.12$ $p=0.0001$, Treatment $F(5,60) = 4.89$ $P=0.0306$, n =7 per group) with Tukey's post-hoc test in comparison to baseline data (* $p < 0.05$ over contralateral saline # $p < 0.05$ over pre-stroke baseline). (B) Percentage of hindlimb steps containing errors in the horizontal ladder test at 7 and 14 days post-stroke. Data was analyzed by two-way ANOVA(Treatment x Testing day $F(10,60) = 1.685$ $p=0.91$, testing day $f(2,60) = 7.28$ $p=0.03$, Treatment $F(5,60) = 0.67$ $P=0.89$, n =7 per group) with Tukey's post-hoc test in comparison to baseline data (C) The ipsilateral preference at 7 and 14 days post-stroke induced by ET-1/L-NAME co-injection in the cylinder test. Data analyzed by one-way ANOVA ($F(2,21) = 17.14$, $P = 0.0001$, n=7 per group) with Tukey's post-hoc test in comparison to pre-stroke baseline data. (* $p < 0.05$).

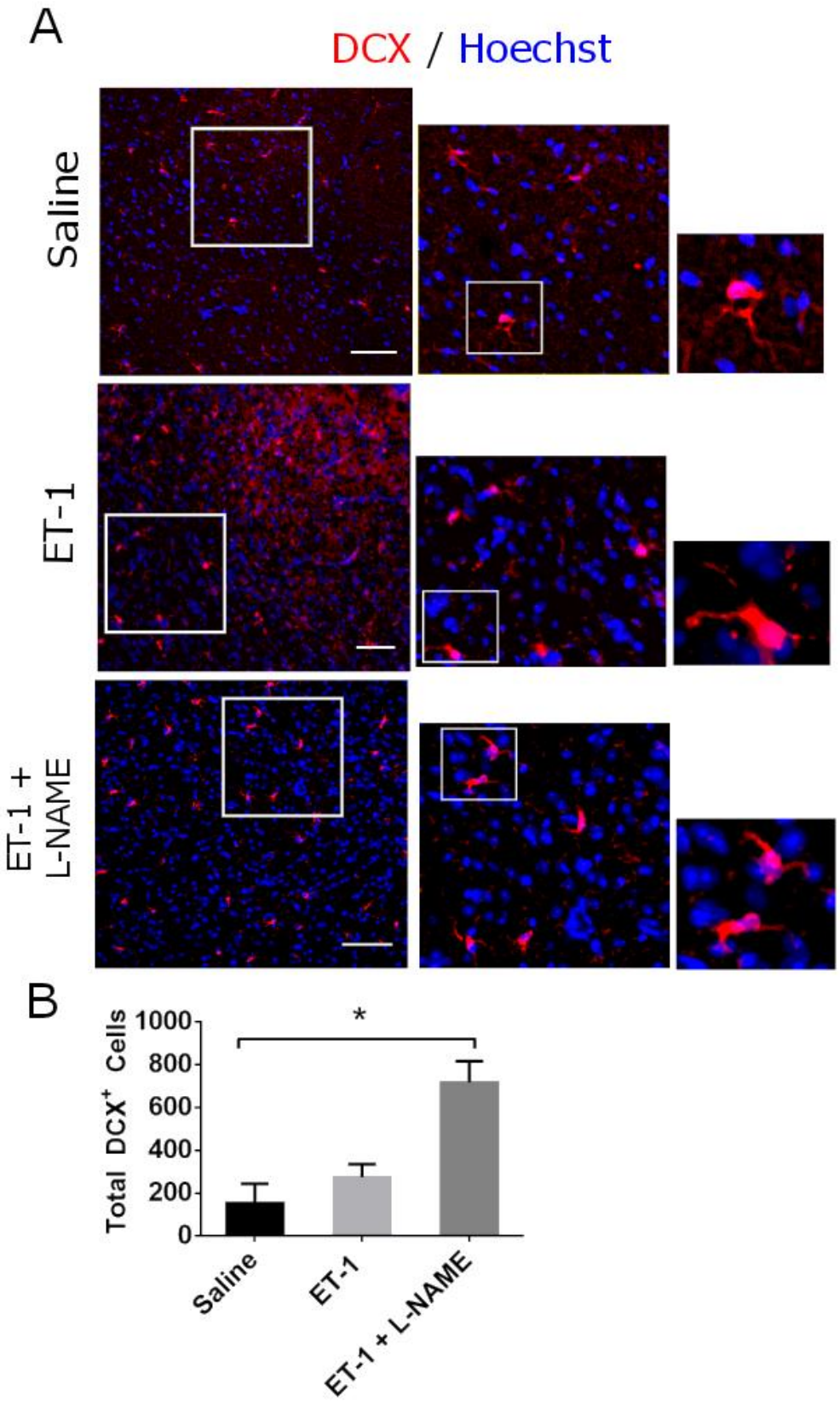
A
DCX / Hoechst
Saline
ET-1
ET-1 + L-NAME
B
Total DCX+ Cells
1000
800
600
400
200
0
*
Saline
ET-1
ET-1 + L-NAME

Figure 5: **The ET-1/L-NAME model produces a neurogenic response**. (A) Fluorescent micrograph of DCX (red) and Hoechst (blue) in the cortex of saline, ET-1, and ET-1/L-NAME injected mice at 14 days post-injection. Images were obtained from the periiinfarct region. (B) Quantification of DCX^+ cells in the cortex as shown in (A). The total number of DCX + cells counted from six sections was normalized by multiplication of a factor of ten to account for serial tissue collection. Scale bars =50µm. Data analyzed by one-way ANOVA ($F(2,9) = 11.21$, $P = 0.0036$, n= 3 per group) with Dunnetts post-hoc test in comparison to saline treatment (* $p < 0.05$).

3.4 Disruption of the aPKC-CBP pathway does not alter stroke infarct volume

Previous studies suggested that CBP plays a key role in neuronal ischemic resistance through its interaction with HIF1-α [65]. It is not clear whether this resistance is conferred through the aPKC-CBP pathway. Therefore, it was important to assess whether the genotypes affect infarct volume that could complicate post-stroke cellular or behavioural results. Cresyl violet staining was performed at 3 and 14 days post-stroke to assess infarct volume. No difference in infarct volume was found between WT and KI-CBPS436A mice at either time point (Fig 6). Thus, the aPKC-CBP pathway does not regulate ischemic resistance.

3.5 The aPKC-CBP pathway modulates post-stroke motor recovery

Mice were tested on the horizontal ladder and cylinder tasks at 7 and 14 days post-stroke to assess motor deficits. Both WT and KI-CBPS436A mice showed a comparable baseline (4-7% error rates) pre-stroke in the horizontal ladder test (Fig. 7A). Seven days after stroke, an increase in the step error (14-18%) occurred in both genotypes from both contralateral and ipsilateral forelimbs (not hindlimb). Interestingly, 14 days after stroke, KI-CBPS436A mice displayed severe deficits when compared to WT mice (Fig 7A). A very similar pattern was shown in the cylinder test as well. Both WT and KI-CBPS436A mice displayed no preference in forepaws to touch the cylinder wall pre-stroke. ET-1/L-NAME injections caused an ipsilateral preference (24%) at 7 days post-stroke for both genotypes. 14 days post-stroke, KI-CBPS436A mice showed significantly higher error rate than WT mice, implicating less recovery in KI mice (Fig 7B).

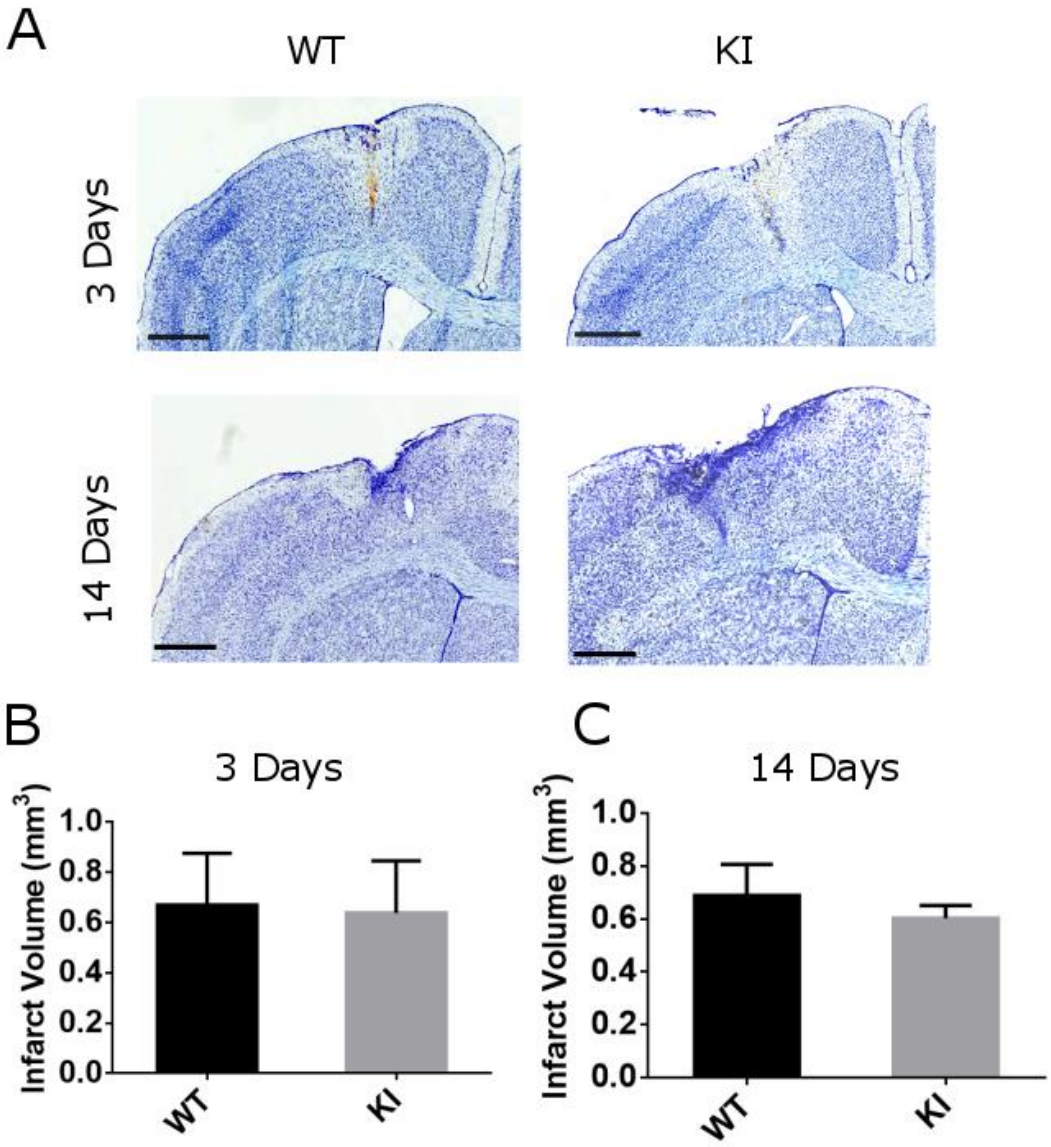
A
WT
KI
3 Days
14 Days
B
3 Days
Infarct Volume (mm3)
1.0
0.8
0.6
0.4
0.2
0.0
WT
KI
C
14 Days
Infarct Volume (mm3)
1.0
0.8
0.6
0.4
0.2
0.0
WT
KI

Figure 6: **KI-CBPS436A mice do not have altered infarct volumes at 3 and 14 days post-stroke.** A) Cresyl violet staining images of the ipsilateral cortex from WT and KI-CBPS436A mice at 3 and 14 days following ET-1/L-NAME co-injections. Scale bars =50 µm (B-C) infarct volumes were analyzed at 3 (B) and (C) 14 days following ET-1/L-NAME co-injections. Data analyzed by Student's T-test (n=6/per group for 3 days; n = 9/ per group for 14 days).

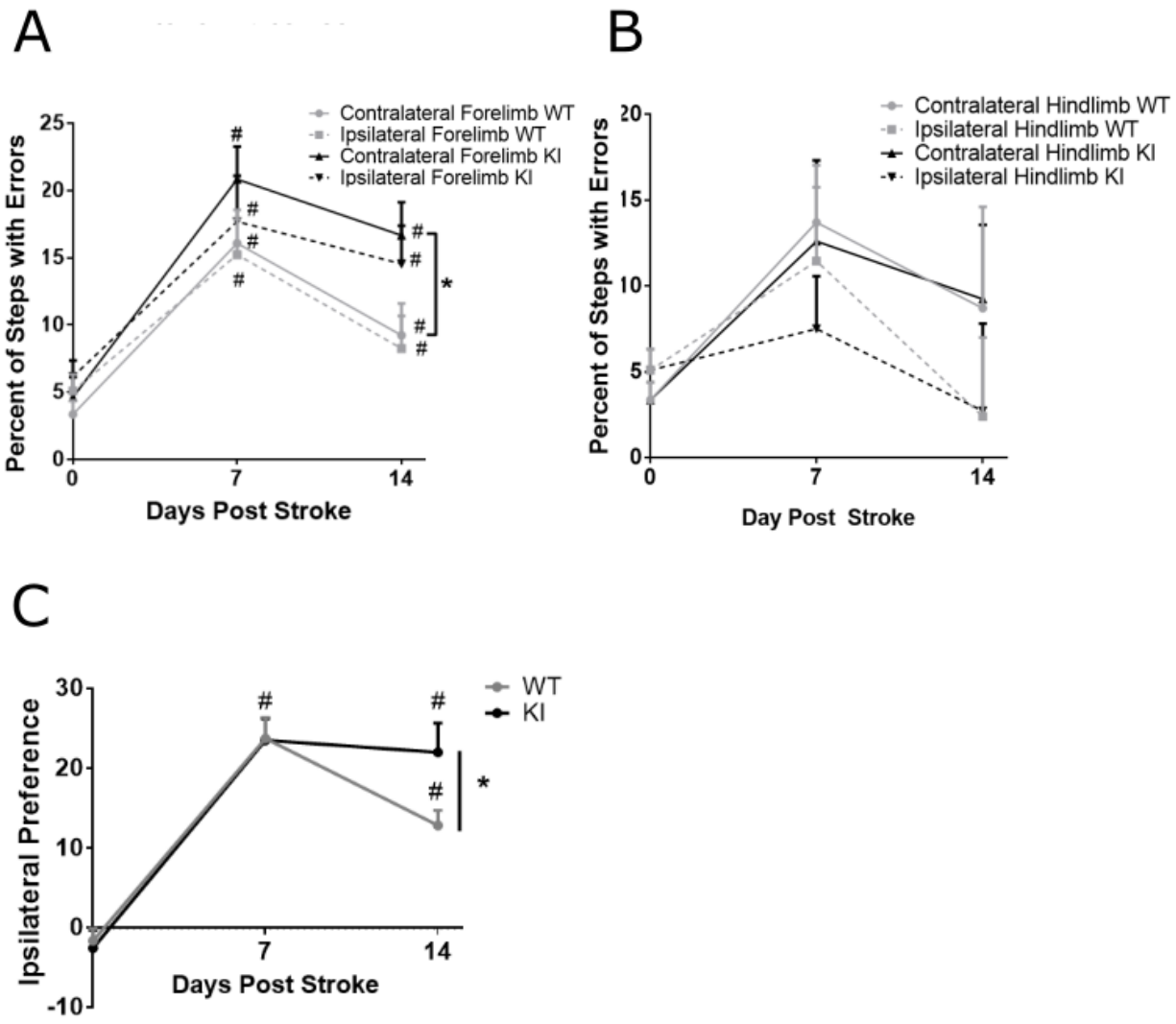
A
Contralateral Forelimb WT
Ipsilateral Forelimb WT
Contralateral Forelimb KI
Ipsilateral Forelimb KI
Percent of Steps with Errors
Days Post Stroke
B
Contralateral Hindlimb WT
Ipsilateral Hindlimb WT
Contralateral Hindlimb KI
Ipsilateral Hindlimb KI
Percent of Steps with Errors
Day Post Stroke
C
WT
KI
Ipsilateral Preference
Days Post Stroke

Figure 7: **KI-CBPS436A mice show reduced post-stroke motor recovery.** (A) The percentage of forelimb error step at 7 and 14 days post-stroke using ET-1/L-NAME cortical stroke model in WT and KI-CBPS436A mice. (Two-Way ANOVA, Time x Genotype, $F(6,168) = 0.76$ $P=0.7587$, Time $F(2,168) = 4.607$ $p = 0.0113$, Genotype $F(3,168) = 0.7047$ $p = 0.56$, n= 17 for WT, n= 13 for KI with Dunnet's Post-hoc test (*$P<0.05$ compared to contralateral WT, # $p < 0.05$ compared to pre-stroke baseline). The percentage of hindlimb error step at 7 and 14 days post-stroke using ET-1/L-NAME cortical stroke model in WT and KI-CBPS436A mice. (Two-Way ANOVA, Time x Genotype, $F(6,152) = 2.174$, $P=0.899$, Time $F(2,168) = 5.30$ $p = 0.0453$, Genotype $F(3,168) = 3.25$ $p = 0.32$, n= 17 for WT, n= 13 for KI with Dunnet's Post-hoc test. (C) The ipsilateral preference in the cylinder test at 7 and 14 days post-stroke induced by ET-1/L-NAME co-injections in WT and KI-CBPS436A mice. Data analyzed by Two-Way ANOVA (Time x Genotype $F(2,42) = 2.395$ $P=0.1035$, Time $F(1,20)$ $p=0.0838$, genotype $F(20,20)$ $p=0.878$, n= 17 for WT, n= 13 for KI) with Tukey's Post-Hoc test (* $p < 0.05$ compared to WT, # $p < 0.05$ compared to pre-stroke baseline).

3.6 Disruption of the aPKC-CBP pathway does not alter neuroblast population in the injured cortex following stroke

The robust proliferation, activation, and migration of neuroblasts from the SVZ towards the site of ischemic injury is a well-documented in rodent models of stroke [83]. I have confirmed a robust increase in the population of DCX^+ cells following ET-1/L-NAME injections as compared to saline injections 14 days post-stroke (Fig 5). To assess whether the aPKC-CBP pathway regulates post-stroke neurogenesis, I performed the same experiment as shown in Figure 5 to a group of KI-CBPS436A mice and their wildtype littermates. Surprisingly, the population of DCX+ newborn in the injured cortex was not altered in KI-CBPS436A mice at 14 days post-stroke (Fig 8A-C).

3.7 The aPKC-CBP pathway regulates vascular remodeling

Previous studies have demonstrated that epigenetic modifications with HDACi can increase angiogenesis and vascular coverage post-stroke[63-64]. To assess whether the aPKC-CBP pathway modulates post-stroke vascular remodeling, brain sections collected at 14 days post-stroke with CD31 to label endothelial cells using immunohistochemistry. Manual counts of the number of CD31+ micro-vessels (Fig 9D) and automated counts of vascular coverage using Image J (Fig 9E) revealed that the ipsilateral cortex in both genotypes had reduced vasculature compared to contralateral cortex (Fig 9). In addition, KI-CBPS436A mice showed a significant decrease in the number of microvessels and the vascular coverage when compared to WT mice in the ipsilateral cortex (Fig 9). I further performed 3D cortex vasculature analysis using brains from 25 days post-stroke. Interestingly, quantification analysis showed that ipsilateral vessel length and branching points from WT mice were comparable to those in contralateral cortex, implying a

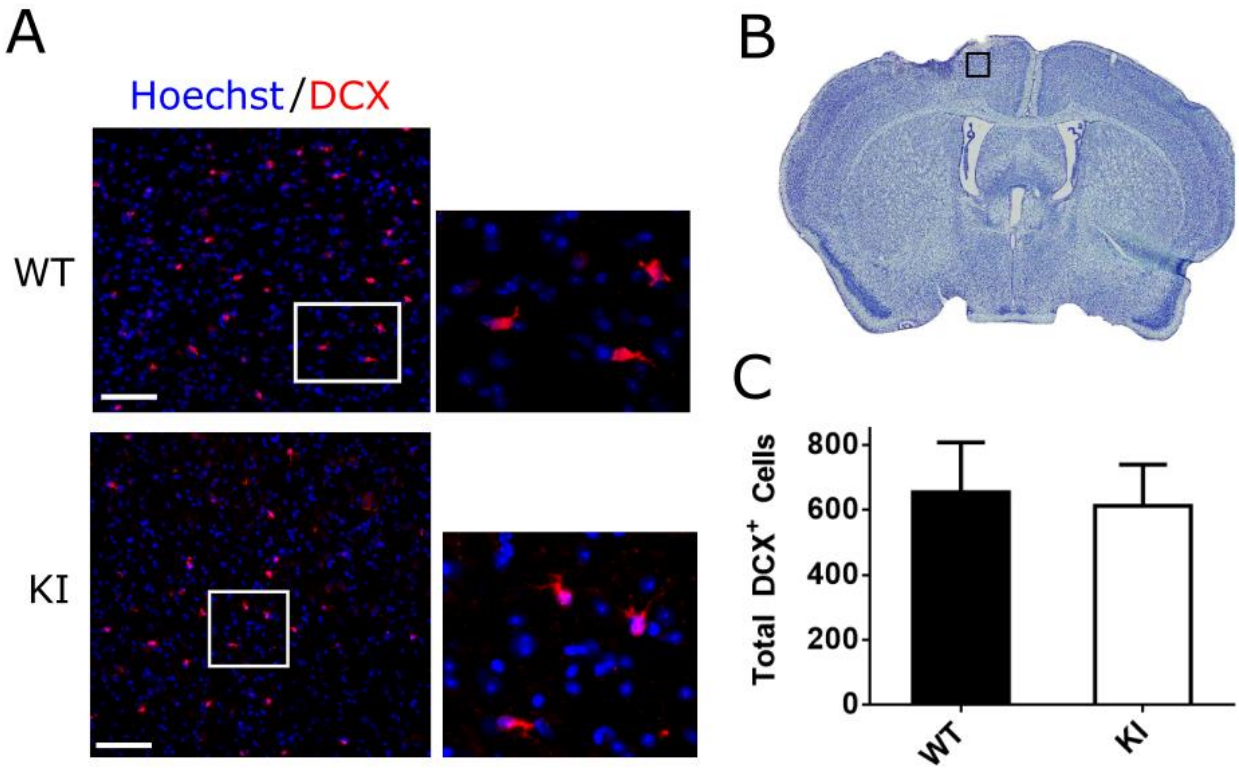
A
Hoechst/DCX
WT
KI
B
C
Total DCX+ Cells
800
600
400
200
0
WT
KI

Figure 8: **KI-CBPS436A mice show unaltered post-stroke neurogenesis.** (A) Fluorescent micrograph of DCX (red) and Hoechst (blue) labelling in the post-stroke periinfarct region. Scale bar= 50µm. (B) Representative area of periinfarct region for cell counts. (C) Total DCX^+ cell counts within the periinfarct region. The total number of DCX + cells counted from six sections were normalized by multiplication of a factor of ten to account for serial tissue collection. Data was analyzed by Students T-test, n = 5.

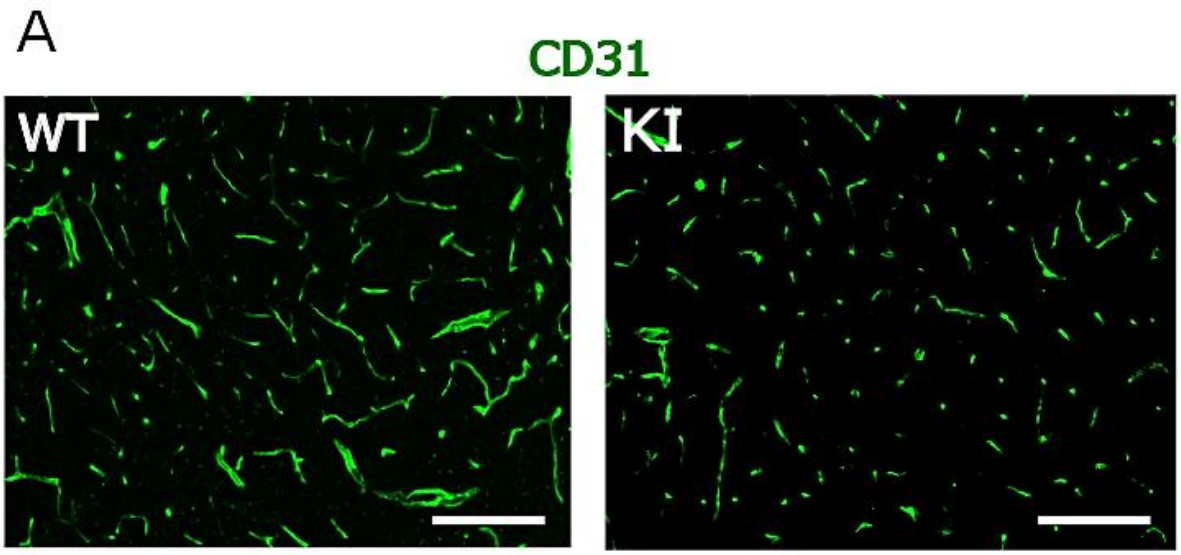
A
CD31
WT
KI

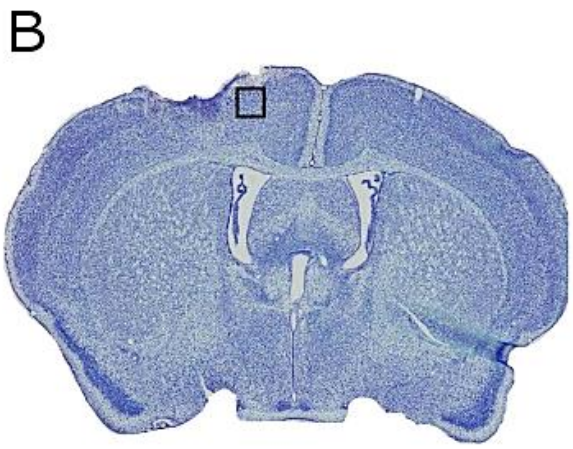
B

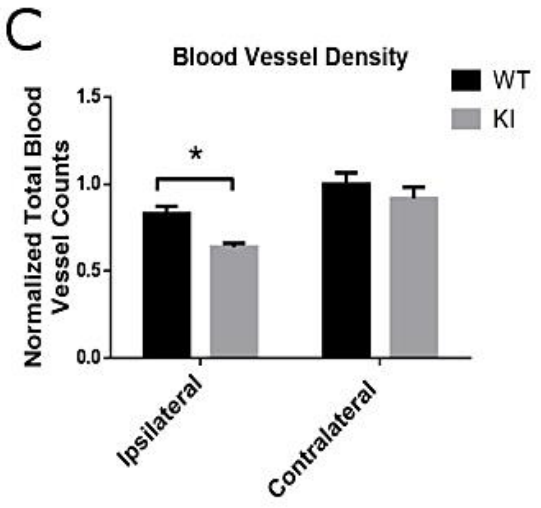
C
Blood Vessel Density
WT
KI
Normalized Total Blood Vessel Counts
1.5
1.0
0.5
0.0
*
Ipsilateral
Contralateral

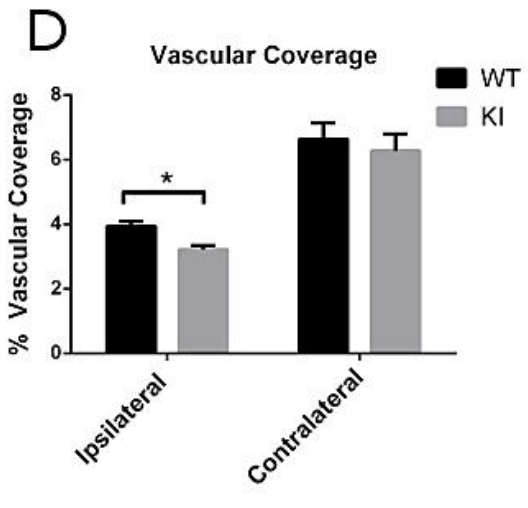
D
Vascular Coverage
WT
KI
% Vascular Coverage
8
6
4
2
0
*
Ipsilateral
Contralateral

Figure 9: **KI-CBPS436A mice show reduced vascular coverage and density post-stroke.** (A) Fluorescent micrographs of CD31 (green) in the ipsilateral cortex from WT and KI-CBPS436A mice 14 days post-stroke. Scale Bar =100um. (B) Representative images location in the cresyl violet staining picture (C) Total blood vessel counts from WT and KI-CBPS436A mice 14 days post-stroke in the ipsilateral and contralateral cortex. Values were normalized to the average WT contralateral value. Data was analyzed by two-way ANOVA (Genotype x Hemisphere interaction $F(1,12) = 1.116$ $P = 0.3022$, Genotype $F(1,12)=4.317$ $p=0.0599$, hemisphere $F(1,12) = 0.03353$ $p=0.857$, n=7/per group), with Tukey's post-hoc test. * $p < 0.05$ (D) The percentage of vascular coverage of WT and KI-CBPS436A mice 14 days post-stroke in the ipsilateral and contralateral cortex measured by particle analysis using Image J. Data was analyzed by two-way ANOVA (Genotype x Hemisphere interaction. $F(1,8) = 0.225$, $P = 0.649$, Genotype $F(1,8)=0.58.76$ $p=0.0001$, hemisphere $F(1,8) = 2.093$ $p=0.1860$, n=4/per group), with Tukey's post-hoc test (* $p < 0.05$).

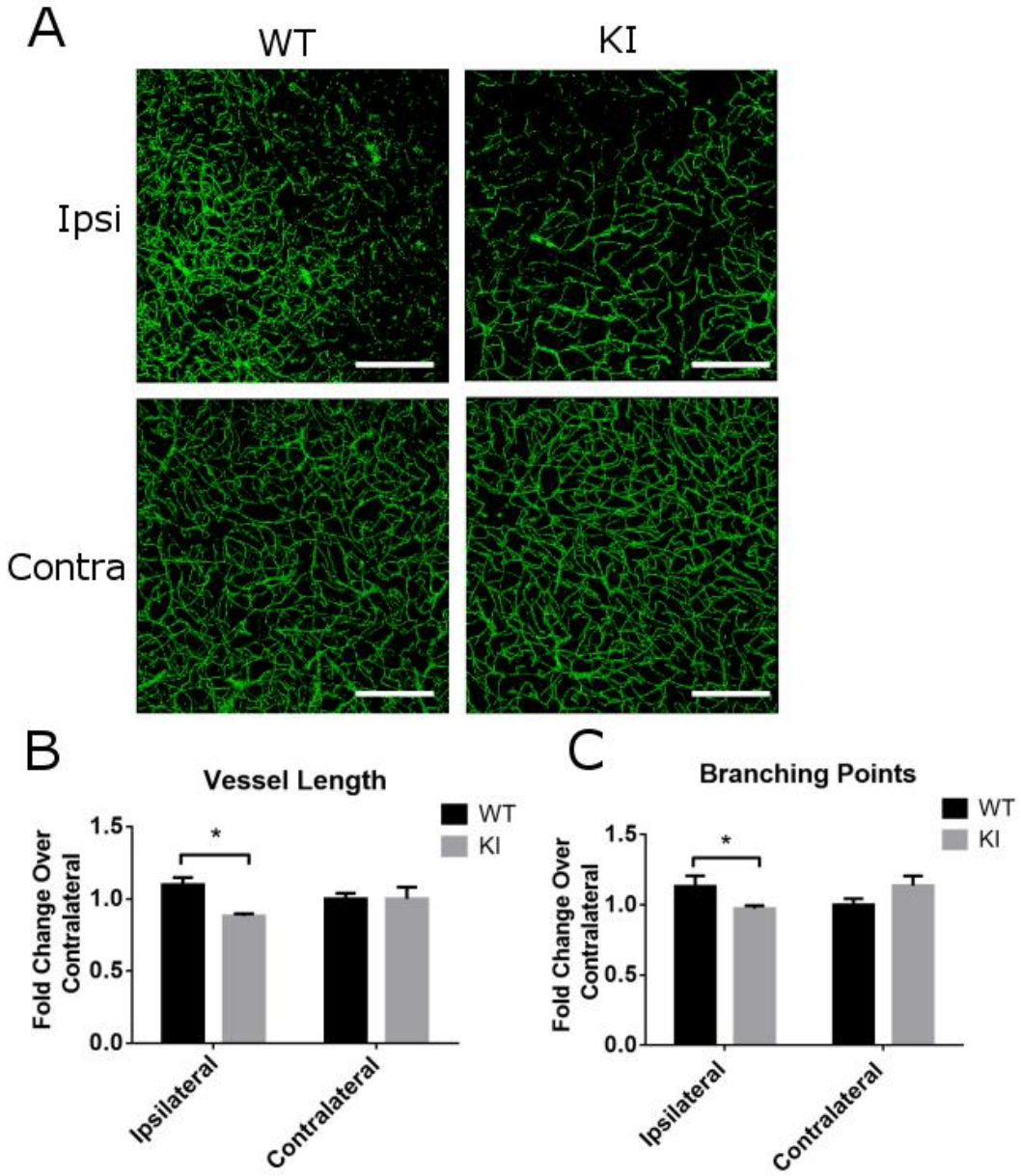
A
WT
KI
Ipsi
Contra
B
Vessel Length
WT
KI
Fold Change Over Contralateral
1.5
1.0
0.5
0.0
*
Ipsilateral
Contralateral
C
Branching Points
WT
KI
Fold Change Over Contralateral
1.5
1.0
0.5
0.0
*
Ipsilateral
Contralateral

Figure 10: **KI-CBPS436A mice showed reduced vessel length and branching points post-stroke as measured by 3D morphometric analysis.** (A) Z-Projection of 80-100 µm confocal microscopy images obtained from the periinfarct region and contralateral hemisphere of WT and KI-CBPS436A mice 25 days post-stroke, immunostained for CD31 (green). Scale bar = 100 µm. (B-C) Vessel Length and (C) Branching points normalized to the average WT contralateral area as analyzed with 3D morphometric analysis using python 2.7. Values were normalized as fold change over contralateral for each mouse (Genotype x Hemisphere interaction $F(1,22) = 1.116$ $P = 0.3022$, Genotype $F(1,12)=4.317$ $p=0.0599$, hemisphere $F(1,12) = 0.03353$ $p=0.857$, n=7/per group for vessel length; Genotype x hemisphere interaction Genotype x Hemisphere interaction. $F(1,4) = 1.225$, $P = 0.0389$, Genotype $F(1,12)=0.06017$ $p=0.8104$, hemisphere $F(1,12) = 0.0268$ $p=0.8726$ for Branching points)(n=5 for WT, n = 3 for KI). Data further analyzed by Tukey's post-hoc test, * $p < 0.05$.

sign of vasculature recovery. However, KI-CBPS436A mice displayed consistently reduced ipsilatereral vessel length and branching points when compared to WT mice (Fig 10).

To determine whether the reduced vasculature in KI-CBPS436A mice was caused by their impaired ability to form newly-generated blood vessels, I assessed post-stroke angiogenesis by analyzing the population of newborn endothelial cells post-stroke. To do that, the thymidine analog EdU was given to mice by I.P injection from 2-5 days post stroke (50mg/kg), and the brains were collected 14 days after stroke and fixed with acetone. EDU was visualized using click-it chemistry, which provides a much cleaner staining when compared with BrdU staining procedure. The number of EDU and $CD31^+$ co-labeled newborn blood vessels was counted and shown as a percentage of total EDU^+ cells in the ipsilateral cortex (Fig 11). As expected, the percentages of EDU/CD31+ newly generated blood vessels was significantly reduced in KI-CBPS436A mice. Since pericytes are known to stabilize the newly-formed blood vessels and neurovascular units[85], I also immunostained the brain sections from the same group of mice with EDU and PDGFRβ, and observed that the percentage of EDU^+/ $PDGFR\beta^+$ pericytes was also significantly decreased in KI-CBPS436A mice (Fig 12). These results suggest that the aPKC-CBP pathway is required for post-stroke vascular remodeling, possibly through regulating post-stroke angiogenesis.

3.8 KI-CBPS436A mice show a larger population of multipotent pericytes post-stroke

Recent findings show that pericytes can enter a multipotent state following stroke, representing a $Nestin^+/Sox2^+$ population with endothelial morphology in the infarct region that does not arise from the SVZ [33, 86]. This population of multipotent pericytes is able to

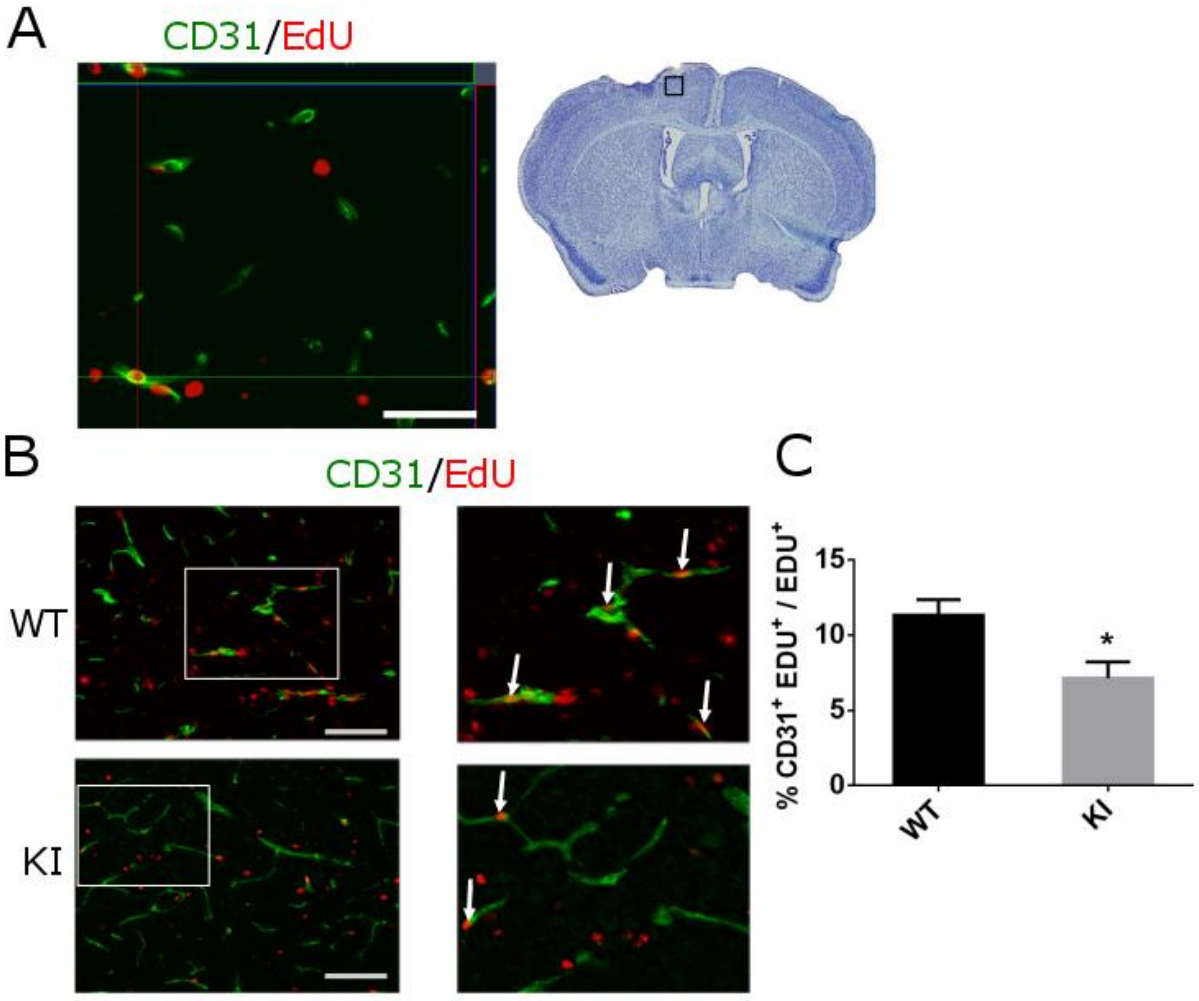
A
CD31/EdU
B
CD31/EdU
WT
KI
C
% CD31+ EDU+ / EDU+
15
10
5
0
*
WT
KI

Figure 11: **KI-CBPS436A mice show reduced post-stroke angiogenesis.** WT and KI-CBPS436A mice who received EDU injections (50mg/kg, I.P) 2-5 days post stroke, and were sacrificed at 14 days post-stroke. (A) Orthogonal confocal image of CD31 (green) and EDU (red) co-localization in the periinfarct region 14 days post stroke. Scale bars= 50µm. **(**B) Fluorescent micrographs of the ipsilateral cortex, immunostained for CD31 (green) and EDU (red), from WT AND KI-CBPS436A mice. Representative location where images were taken is shown on the right. Scale bars= 50µm. (C) The percentage of $CD31^{+}/EDU^{+}$ cells out of total EDU^{+} cells in the ipsilateral cortex at 14 days post-stroke from WT and KI-CBPS436A mice. Data analyzed by Student's T-test, * $p < 0.05$, n = 4/per group.

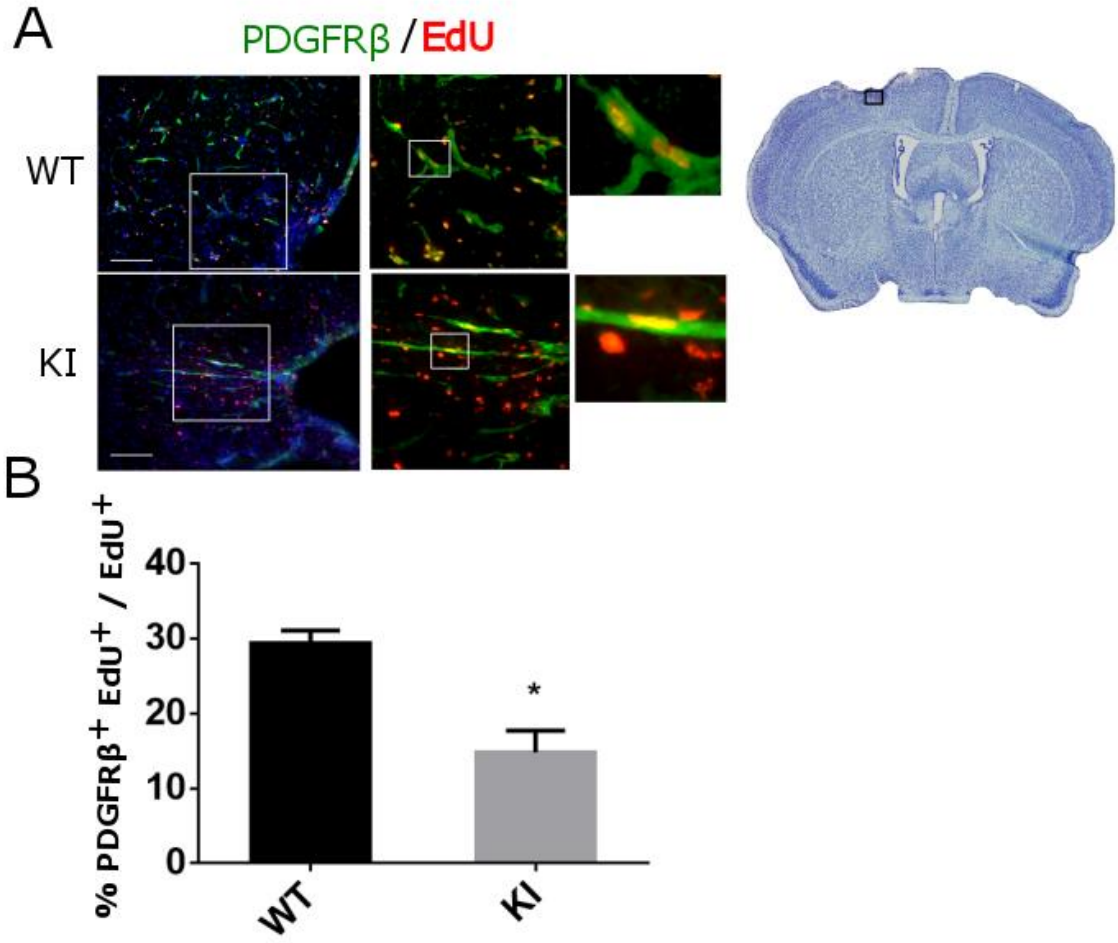
A
PDGFRβ / EdU
WT
KI
B
% PDGFRβ+ EdU+ / EdU+
40
30
20
10
0
*
WT
KI

Figure 12: **KI-CBPS436A mice show reduced newly-generated pericytes post-stroke.** (A) Fluorescent micrographs of the ipsilateral cortex , immunostained for PDGFRβ (green) and EDU (red), from WT and KI-CBPS436A mice who received EDU administration (50mg/kg, I.P) 2-5 days post stroke, and sacrificed at 14 days after stroke. Scale bars= 50µm (B) The percentage of $PDGFR\beta^{+}/EDU^{+}$ cells out of total EDU^{+} cells in the ipsilateral cortex 14 days post-stroke from WT and KI-CBPS436A mice. Data analyzed by Student's T-test, * $p < 0.05$, n = 4/per group.

differentiate into both neural precursor cells and microglia post-stroke. I asked whether the reduced number of stroke-induced newborn pericytes in KI-CBPS436A mice is the outcome of increased reprograming of pericytes to other cell types.

To first confirm that any populations of $Sox2^+$ cells in the post-stroke cortex were not derived from the SVZ, we injected BrdU 4 times, three hours apart, beginning 24 hours before surgery. This paradigm is expected to label the vast majority of actively proliferating neural precursors in the SVZ. The mice were sacrificed at 3 days following stroke and the brains were stained for BrdU and Sox2. $BrdU^+/Sox2^+$ cells appeared in the SVZ, but only $Sox2^+/BrdU^-$ cells were identified in the cortex (Fig 13). Therefore, the Sox2 population in the cortex was confirmed to be locally derived after stroke and not derived from proliferating cells labelled pre-stroke.

On the basis of this finding, we further immunostained brain sections from 3 days post-stroke with Sox2 and Nestin to identify multipotent pericytes. Two populations of $Sox2^+/Nestin^+$ were observed in the ipsilateral cortex; cells on the edge of the glia scar with astrocyte-like morphology and cells projected from the meninges with longer endothelial-like morphology. The cells with endothelial-like morphology were assumed to be pericytes, with the double positive population showing similarities to previously described multipotent pericytes which appear post-stroke [33, 86]. KI-CBPS436A mice displayed a significant increase in the population of the $Sox2^+/Nestin^+$ multipotent pericytes post-stroke (Fig 14).

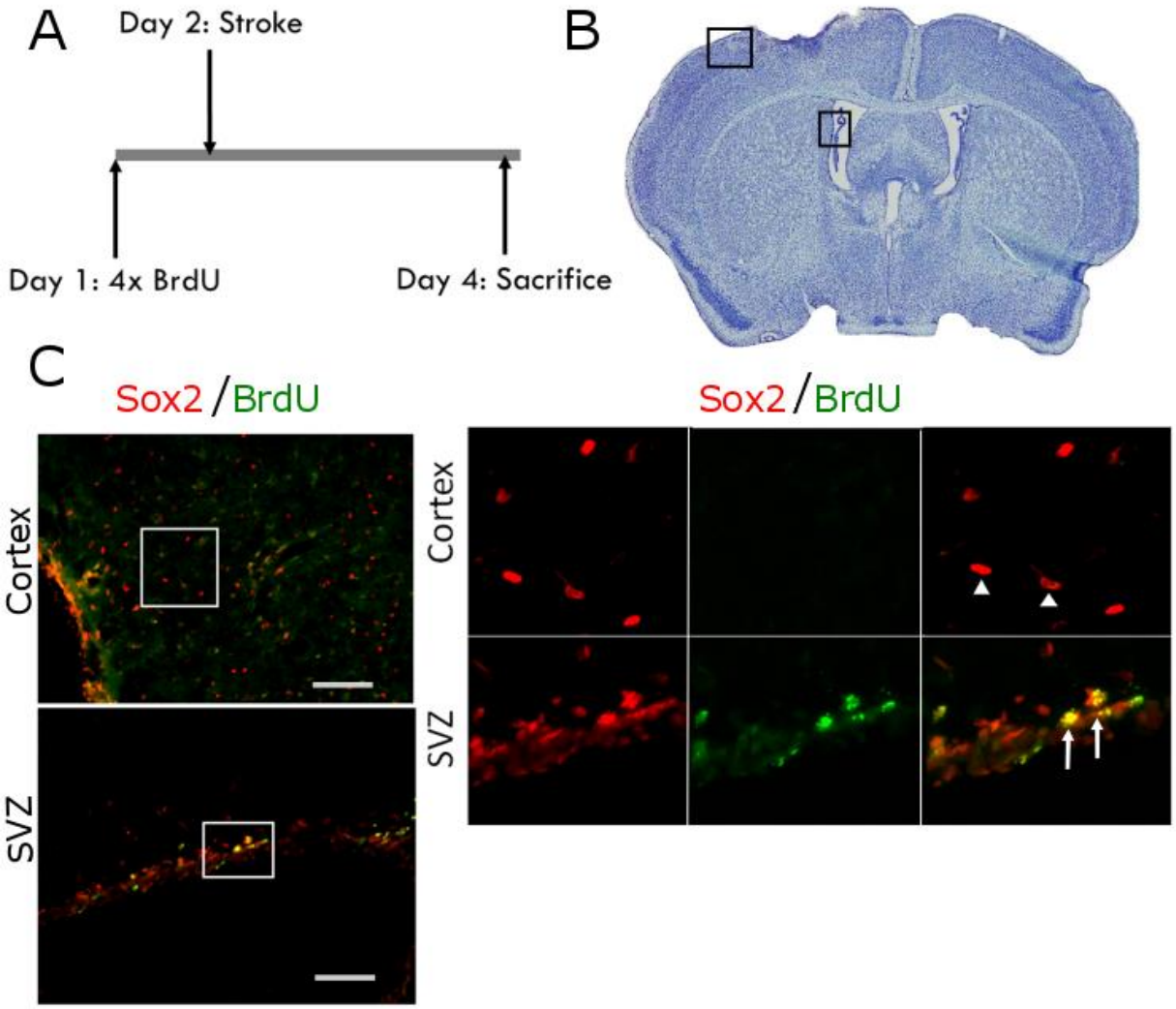
A
Day 2: Stroke
Day 1: 4x BrdU
Day 4: Sacrifice
B
C
Sox2 /BrdU
Sox2 /BrdU
Cortex
SVZ
Cortex
SVZ

Figure 13: **Locally derived Sox2 positive neural precursors were observed in ET-1/L-NAME cortical stroke.** (A) Flow chart showing that mice were injected with BrdU (100mg/kg, I.P) four times, 3 hours apart, beginning 24 hours before stroke. (B) Representative areas for the identification of cells in the periinfarct and SVZ. (C) Fluorescent micrographs of the ipsilateral cortex and SVZ at 3 days post-stroke, stained for Sox2 (red) and BrdU (green), Scale bar= 100 µm. Enlarged images showing co-staining of Sox2 (red) and BrdU (green) within the SVZ and cortex. Arrows denote co-labelled cells, arrow heads denote single-labeled cells with $Sox2^{+}$.

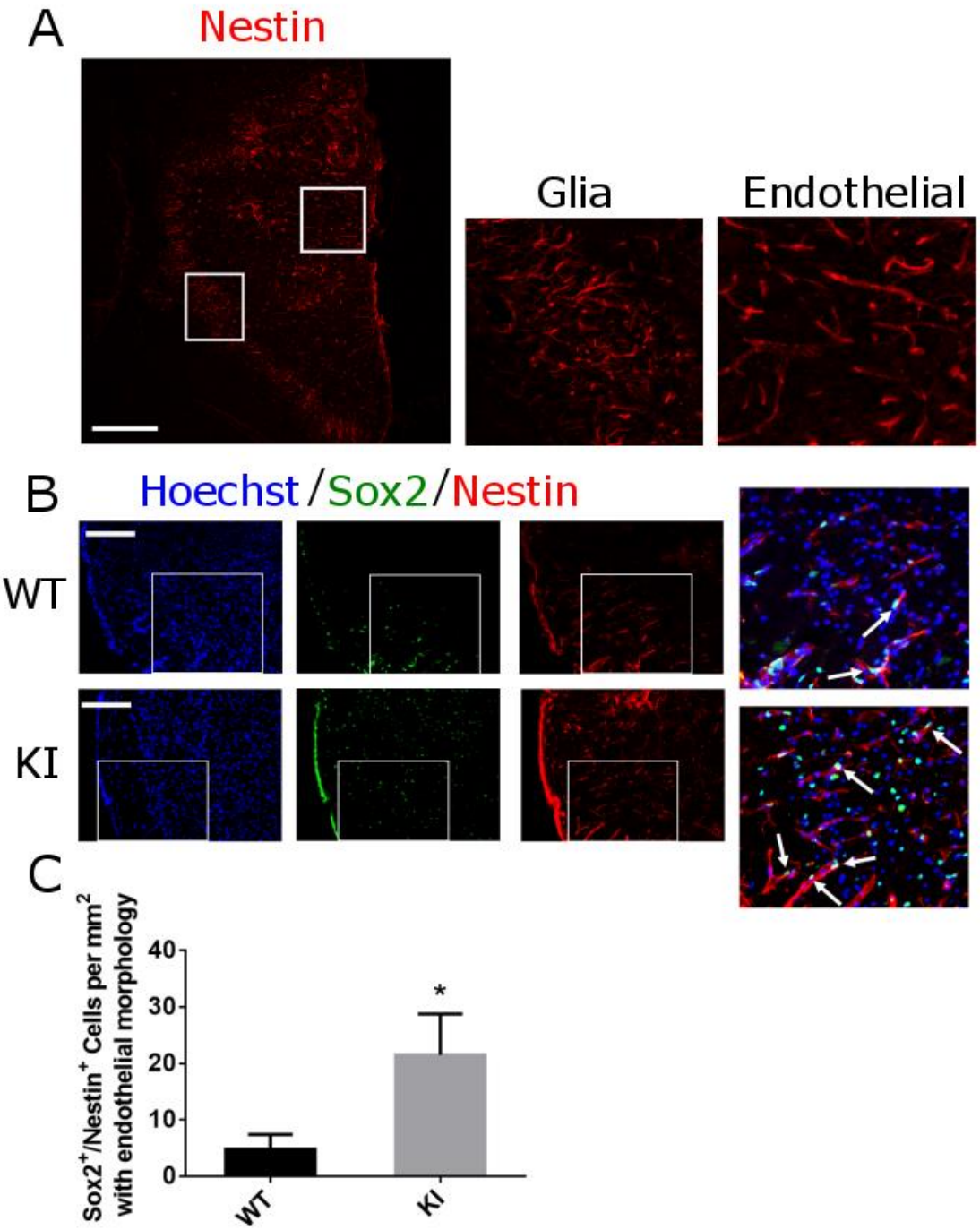
A
Nestin
Glia
Endothelial
B
Hoechst/Sox2/Nestin
WT
KI
C
Sox2+/Nestin+ Cells per mm2 with endothelial morphology
40
30
20
10
0
*
WT
KI

Figure 14: **KI-CBPS436A mice show increased multipotent pericytes 3 days post-stroke.** The post stroke ipsilateral cortex was stained for nestin (red), Sox2 (green) and hoechst (blue) at 3 days post-stroke. (A) Nestin (red) staining photographs show representative areas for glia and endothelial like morphology, scale bar = 100µm (B) Immunostaining images display $Sox2^+/Nestin^+$ cells with endothelial like morphology, Scale bars=50µm. (C) Quantification of $Sox2^+/Nestin^+$ cells with endothelial-like morphology within the infarct/periinfarct regions. * $p < 0.05$.

4.0 Discussion

Using ET-1/L-NAME induced focal cortical stroke model and a genetically-modified KI-CBPS436A mice, I demonstrate three key events that are mediated by the aPKC-CBP pathway post-stroke : 1) intrinsic stroke functional recovery 2) vascular remodeling through modulation of angiogenesis 3) production of locally-derived neural precursor cells, possibly through reprograming of stroke-induced pericytes.

4.1 Addition of L-NAME to the ET-1 model of stroke increases infarct size and produces consistent functional deficits

ET-1-induced cortical stroke model was originally outlined in mice in 2008 [20]. However, deficits were only observed for 3 days and recovered rapidly. Since then, the model was further refined and studied. In 2014, a triple injection of ET-1 was shown to create long-lasting and larger infarcts in FVBN mice [22]. We were unable to replicate either the infarct size or motor deficits using the triple injection ET-1 model of stroke in our CBPS436A mouse line of mixed background. Previously, the difference in the efficacy of the ET-1 model between mice and rats was studied. Higher expression of the ET-1B receptor that leads to higher levels of vasodilation was evident in mice[21]. It seems plausible that the ET-1B receptor may also have differential expression among different mouse lines. In fact, previous work testing the ET-1 model on a variety of strains of mice demonstrated that only C57Bl/6 and FVB mice showed infarcts consistently in response to ET-1 alone [20]. Our work shows that the triple injections of ET-1 alone are not sufficient to produce consistent cortical stroke in our transgenic mouse strain.

Based on the fact that activation of the ET-1B receptor leads to production of nitric oxide and blocks the vasoconstrictive effects of the ET-1A receptor, the eNOS inhibitor L-NAME was used in previous studies to block the production of nitric oxide and enhance ET-1 induced vasoconstrictive effect [23]. However, in this specific study, the group also combined ET-1/L-NAME with common carotid artery occlusion (CCAO), making it difficult to interpret results for ET-1 and L-NAME co-injection. Recently, the co-injection of ET-1 and L-NAME into the internal capsule has been used to produce a subcortical stroke [24]. Thus, I co-injected ET-1 and L-NAME into the sensorimotor cortex and produced consistent focal cortical stroke. I found that the combination of ET-1 with L-NAME increased the size of stroke infarcts approximately four-fold to an average of 0.6mm^3, when compared to ET-1 injection alone.

To test the extent of motor deficits post-stroke using ET-1/L-NAME co-injections, I performed behavioral analysis at 7 and 14 days post-stroke using adhesive tape test, horizontal ladder test, and cylinder test. The adhesive tape test measures both sensory perception and fine motor skill. It is a well-established test for post-stroke analysis in mice [82]. To my surprise, mice receiving either ET-1 injections alone or ET-1/L-NAME co-injections did not show consistent motor deficits in the adhesive test. There are two potential explanations for the failure to the adhesive test using ET-1/L-NAME cortical stroke model in our transgenic mouse strain. First, the baseline values pre-stroke from our transgenic mouse strain were much lower than those obtained from other strains, such as C57Bl6. Average time to remove the tape at day 1 from our transgenic mouse is 14-second, which is the time that other strains of mice are able to obtain after 5 days of pre-training (personal communications with the lab members in the Lagace lab). It is possible that our mice respond differently to the stress of the test causing less overall time.

Second, stereotaxic injections may mainly target motor cortex but not sensory cortex, or motor cortex related to elbows and shoulders, not wrist and limbs, therefore causing deficits in motor tests involving weight bearing instead of fine motor control of the paw. Thus, the ET-1/L-NAME stroke model I developed here is not sensitive to measure deficits in sensory perception and fine motor control with the adhesive tape test.

Using the horizontal ladder test, which measures limb placement and weight bearing ability, I was able to detect motor deficits at both 7 and 14 days post-stroke following ET-1/L-NAME co-injections. Interestingly, forelimbs showed more consistent deficits when compared to the hindlimbs. It is possible that the speed of traversing the ladder could alter the gait of the mice. Mice that move slowly across the ladder will place more weight on their hind limb, while faster moving mice will lean forward during movement and place more weight on the forelimbs, causing more forelimb errors. Since horizontal ladder run test showed significant motor deficits without contralateral preference in ET-1/L-NAME cortical stroke model, I further used cylinder test, which measures spontaneous forelimb use, to confirm that ET-1/L-NAME co-injections can lead to asymmetric motor deficits, showing ipsilateral preference to use uninjured forepaw. Thus, both horizontal ladder and cylinder tests demonstrate motor deficits in limb placement and weight bearing caused by ET-1/ L-NAME co-injections.

4.2 KI-CBPS436A mice show reduced functional recovery following stroke

A previous study has shown that mice with CBP haploinsuficiency (CBP+/-) display lower ischemic resistance, therefore causing larger infarcts following stroke induction [65]. In this regard, it is important to assess whether the aPKC-CBP pathway is involved in initial stroke-

related brain damage. Interestingly, I observed that WT and KI-CBPS436A mice show similar infarct volumes at 3 and 14 days post-stroke measured by cresyl violet staining, indicating no contribution of the aPKC-CBP pathway to initial stroke-related brain damage. The unaltered stroke infarct size in KI-CBPS436A mice allows me to further dissect the role of the aPKC-CBP pathway in stroke recovery phase. Indeed, I found that both WT and KI-CBPS436A mice have initial motor deficits at 7 days post-stroke. While WT mice show noticeable recovery at 14 days post-stroke, KI-CBPS436A mice display the same extent of motor deficits at both 7 and 14 days post-stroke. The reduction of stroke functional recovery in KI-CBPS436A mice strongly argues the importance of the activation of aPKC-CBP pathway in promoting post-stroke functional recovery. This is supported by indirect evidence, showing that metformin, an activator of this epigenetic pathway, can increase post-stroke functional recovery through both angiogenesis and neurogenesis[76-79].

4.3 The aPKC-CBP pathway modulates post-stroke vascular remodeling

To determine underlying cellular mechanisms for the role of the aPKC-CBP pathway involved in post-stroke functional recovery, post-stroke neurovascular remodeling was further analyzed.

My study is the first to demonstrate the direct involvement of CBPS436 phosphorylation in post-stroke vascular remodeling by showing reduced vessel density/vascular coverage and decreased newly generated blood vessels in KI-CBPS436A mice. These results appear to be in line with previous studies showing the beneficial effects of metformin on angiogenesis [76-79]. Therefore, my results point to the fact that deletion of the aPKC-CBP pathway produces the opposite effect on angiogenesis as activating it through metformin treatment.

Interestingly, increasing evidence emphasizes the role of CBP in vasculogenesis and angiogenesis. One study shows that a truncated form of CBP produces deficits in vasculogenesis causing embryonic lethality [74]. Other studies from the same group demonstrate that CBP and early growth factor -1 (EGR-1) act as binding partners in EPCs to promote vasculogenesis [92,93]. Our own work has found that EGR-1 expression is downregulated in KI-CBPS436A mice (unpublished data in the lab). In these studies, CBP knockdown led to a decrease in the expression of PDGF-β in endothelial cells, the ligand to activate PDGFR-β which is exclusively expressed in pericytes. Stroke induced expression of PDGF-B in endothelial cells acts as a potent signal for pericyte proliferation to participate in vascular remodeling [60,61]. Thus, it is possible that the disruption of endothelial cell-pericyte signaling may occur in KI-CBPS436A mice lacking the aPKC-CBP pathway, causing the decreased stability of newly-generated blood vessels and reduced angiogenesis.

4.4 Stroke induced multipotent pericytes

Locally-derived neural precursors, not migrating from conventional neurogenic regions like the SVZ, have been identified post-stroke in the periinfarct/infarct regions, including neural precursors derived from stroke-induced multipotent pericytes expressing Sox2 and Nestin[87-89]. Interestingly, the locally derived neural precursors ($Sox2^{+}$) exist in the injured cortex of our ET-1/L-NAME stroke model. Furthermore, I observed that the reduced population of pericytes at 14 days post-stroke in KI-CBPS436A mice is correlated well with increased population of multipotent pericytes (Nestin/Sox2+ cells with endothelial morphology) at 3 days post-stroke. This suggests that the aPKC-CBP pathway modulates the production of local neural precursors from perivascular pericytes post-stroke, possibly through epigenetic reprograming. To my

knowledge, this is the first epigenetic reprograming pathway identified to be involved in producing stroke-induced local neural precursors. To further confirm and characterize the role of the aPKC-CBP pathway in the stroke-induced epigenetic reprograming process to generate local neural precursors, future work will involve 1) developing stroke-induced multipotent pericyte culture, and characterizing the function of the multipotent pericytes from both WT and KI-CBPS436A mice; 2) in vivo lineage-tracing pericyte-derived neural precursors following stroke in both WT and KI-CBPS436A mice. My study sets up a solid foundation to initiate this exciting project, which potentially provides an alternative resource to enhance endogenous neurogenesis other than the conventional SVZ neurogenic regions.

4.5 Post-stroke neurogenesis

Our recent study shows that the aPKC-CBP pathway is required to maintain adult hippocampal neurogenesis in response cellular/molecular changes as mice age during early adulthood[84](Appendix 1). Therefore our initial hypothesis was that the aPKC-CBP pathway may be activated post-stroke through stroke-induced transient AMPK activation, an upstream activator of the aPKC-CBP pathway, to enhance post-stroke neurogenesis [75,78,90]. Surprisingly, the total DCX positive newborn neurons in the injured cortex were not altered in KI-CBPS436A mice at 14 days post-stroke.

This can be explained by a few possibilities described below. The increased phosphorylation of CREB [90] following stroke may compensate the neurogenesis defects caused by the deficient aPKC-CBP pathway in KI-CBPS436A mice, as we observed in hippocampal neurogenesis under physiological conditions [84]. In addition, it is possible that the time point at 14 days post-stroke

was too short to observe long-term changes in survival and maturation of neuroblasts. However, the fact that behavioural difference observed at 14 days post-stroke points out that alternative mechanism other than neurogenesis are responsible for spontaneous recovery.

5.0 Conclusion

In summary, I developed the ET-1/L-NAME-induced cortical stroke model, which shows consistent stroke infarct size and motor deficits. Using this model of cortical stroke and CBPS436A knock-in mouse line, I demonstrate that the aPKC-CBP pathway contributes to post-stroke functional recovery, possibly through modulating neurovascular remodeling following stroke.

References

1) Andersen K.K., Olsen T.S., Dehlendorff C. & Kammersgaard L.P. (2009) Hemorrhagic and ischemic strokes compared: stroke severity, mortality, and risk factors. Stroke 40, 2068- 2072.

2) Teasell RW, Foley NC, Bhogal SK, Speechley MR (2003) An Evidence-Based Review of Stroke Rehabilitation. 10(1):29–58.

3) Kruger H, Koot J, Hall R, O'Callaghan C, Bayley M, Corbett D, Prevalence of individuals suffering from the effects of stroke in Canada: Trends and projections, Stroke, 2015, 46, 2226-2231.

4) Prabhakaran, S. Ruff, L, Bernstein P. (2015) Acute Stroke Intervention: A Systematic Review. 313(14):1451–1462.

5) Hacke W, Kaste M, Bluhmki E, Brozman M, Dávalos A, Guidetti D, Larrue V, Lees KR, Medeghri Z, Machnig T, Schneider D, von Kummer R, Wahlgren N, Toni D. Thrombolysis with alteplase 3 to 4.5 hours after acute ischemic stroke. N Engl J Med. 2008 359(13): 1317-1329.

6) Kidwell C, Jahan R, Gornbein J, Alger J, Nenov V, Ajani Z, Feng L, Meyer B, Scott Olson, Schwamm L, Yoo JA, Marshall R, Meyers P, Yavagal D, Wintermark M, Guzy J, Starkman S, Saver J. A trial of imaging selection and endovascular treatment for ischemic stroke. NEngl JMed. 2013 368(10):914-923.

7) Goyal M, Demchuk A, Menon B, Eesa M, Rempel J, Thornton J, Roy D, Jovin T, Willinsky R, Sapkota B, Dowlatshahi D, Frei D, Kamal N, Montanera W, Poppe A, Ryckborst K, Silver F, Shuaib A, Tampieri D, Williams D, Bang O, Baxter B, Burns P, Choe H, Heo J, Holmstedt C, Jankowitz B, Kelly M, Linares G, Mandzia J, Shankar J, Sohn S, Swartz R, Barber P, Coutts S, Smith E, Morrish W, Weill A, Subramaniam S, Mitha A, Wong J, Lowerison M, Sajobi T, and Hill M, Randomized assessment of rapid endovascular treatment of ischemic stroke.N Engl J Med. 2015 372(11):1019-1030.

8) Saver JL, Goyal M, Bonafe A, Diener HC, Levy EI, Pereira VM, Albers GW, Cognard C, Cohen DJ, Hacke W, Jansen O, Jovin TG, Mattle HP, Nogueira RG, Siddiqui AH, Yavagal DR, Devlin TG, Lopes DK, Reddy V, du Mesnil de Rochemont R, Jahan R; SWIFT PRIME Investigators. (2015) Intention for Thrombectomy as Primary Endovascular Treatment for Acute Ischemic Stroke. International Stroke Conference; February 2015; Nashville, TN.

9) Teasell RW, Foley NC, Bhogal SK, Speechley MR. An Evidence-Based Review of Stroke Rehabilitation. 2003. 10(1):29–58.

10) National Institute of Neurological Disorders and Stroke (NINDS). rt-PA Stroke Study Group. Effect of intravenous recombinant tissue plasminogen activator on ischemic stroke lesion size measured by computed tomography. Stroke. 31:2912–2919, 2000.

11) Carmichael ST. (2005) Rodent models of focal stroke: size, mechanism, and purpose. NeuroRx 2(3):396–409.

12) Majid A, He YY, Gidday JM, Kaplan SS, Gonzales ER, Park TS, Fenstermacher JD, Wei L, Choi DW, Hsu CY. Differences in ischemic vulnerability to permanent cerebral ischemia among 3 common mouse strains. Stroke 31:2707–2714, 2001.

13) Watson BD, Dietrich WD, Busto R, Wachtel MS, Ginsberg MD. Induction of reproducible brain infarction by photochemically initiated thrombosis. Ann Neurol 17:497–504, 1985.

14) Albensi BC, Knoblach SM, Chew BG, O'Reilly MP, Faden AI, Pekar JJ. Diffusion and high resolution MRI of traumatic brain injury in rats: time course and correlation with histology. Exp Neurol. 162:61–72, 2000.

15) Schneider G, Fries P, Wagner-Jochem D, Thome D, Laurer H, Kramann B, Mautes A, Hagen T. Pathophysiological changes after traumatic brain injury: comparison of two experimental animal models by means of MRI. MAGMA. 14:233–241, 2003.

16) van Bruggen N, Cullen BM, King MD, Doran M, Williams SR, Gadian DG, Cremer JE. T2- and diffusion-weighted magnetic resonance imaging of a focal ischemic lesion in rat brain. Stroke. 23:576– 582, 1992.

17) Lee VM1, Burdett NG, Carpenter A, Hall LD, Pambakian PS, Patel S, Wood NI, James MF. Evolution of photochemically induced focal cerebral ischemia in the rat. Magnetic resonance imaging and histology. Stroke. 27:2110–2118, 1996.

18) Windle V1, Szymanska A, Granter-Button S, White C, Buist R, Peeling J, Corbett D. An analysis of four different methods of producing focal cerebral ischemia with endothelin-1 in the rat. Exp Neurol. 2006; 201:324–34.

19) Tennant KA, Jones TA. Sensorimotor behavioral effects of endothelin-1 induced small cortical infarcts in C57BL/6 mice. J Neurosci Methods 2009;181:18– 26.

20) Horie N1, Maag AL, Hamilton SA, Shichinohe H, Bliss TM, Steinberg GK. (2008) Mouse model of focal cerebral ischemia using endothelin-1. J Neurosci Methods 173(2):286–290.

21) Wiley, K.E., Davenport, A.P. (2004) Endothelin receptor pharmacology and function in the mouse: comparison with rat and man. J. Cardiovasc. Pharmacol. 44(1):4-6.

22) Roome RB, Bartlett RF, Jeffers M, Xiong J, Corbett D, Vanderluit JL. (2014) A reproducible Endothelin-1 model of forelimb motor cortex stroke in the mouse. J Neurosci Methods. 233:34–44.

23) Uchida H, Sakata H, Fujimura M, Niizuma K (2015) Experimental model of small subcortical infarcts in mice with long-lasting functional disabilities. Brain Res. 1629:318–328.

24) Kuhn HG, Eisch AJ, Spalding K, Peterson DA (2016) Detection and Phenotypic Characterization of Adult Neurogenesis. Cold Spring Harb Perspect Biol. 8(3):a025981

25) Zhang ZG, Chopp M (2015) Promoting brain remodeling to aid in stroke recovery. Trends Mol Med. 21(9):543–548.

26) Zhao, C, Deng, W, and Gage FH. Mechanisms and functional implications of adult neurogenesis. Cell 2008, 132: 645-660.

27) Reynolds A, and Weiss S. Generation of neurons and astrocytes from isolated cells of the adult mammalian central nervous system. Science 1992, 255:1707–1710.

28) Rochefort C, Gheusi G, Vincent JD and Lledo PM. (2002) Enriched odor exposure increases the number of newborn neurons in the adult olfactory bulb and improves odor memory. J Neurosci 22: 2679-2689.

29) Spalding KL1, Bhardwaj RD, Buchholz BA, Druid H, Frisén J. (2005) Retrospective birth dating of cells in humans. Cell. 122, 133–143.

30) Bergmann O1, Liebl J, Bernard S, Alkass K, Yeung MS, Steier P, Kutschera W, Johnson L, Landén M, Druid H, Spalding KL, Frisén J. (2012) The age of olfactory bulb neurons in humans. Neuron. 74, 634–639

31) Hou, S, Wang, Y, Xu M, Shen, D, Wang, J, Huang, F, Yu, Z, and Sun, F. Functional integration of newly generated neurons into striatum after cerebral ischemia in the adult rat. Stroke. 39 :2837-44.

32) Shimada IS, LeComte, MD, Granger, JC, Quinlan, NJ and Spees JL. (2008) Self-Renewal and Differentiation of Reactive Astrocyte-Derived Neural Stem/Progenitor Cells Isolated from the Cortical Peri-Infarct Area after Stroke. J Neurosci. 32:7926 –7940.

33) Nakagomi, T and Matsuyama, T. (2012) Ischemia-Induced Neural Stem/Progenitor Cells Within the Post-Stroke Cortex in Adult Brains. Neural Stem Cells and Therapy.

34) L, L, Harms, KM, Ventura, PB, Lagace, DC, Eisch, AJ, Cunningham,LA. (2010) Focal cerebral ischemia induces a multilineage cytogenic response from adult subventricular zone that is predominantly gliogenic. Glia. 58: 1610-9.

35) Arvidsson, A., Kirik, TD, Kokaia, Z and Lindvall, O. (2002) Neuronal replacement from endogenous precursors in the adult brain after stroke. Nat Med. 8:963-70.

36) Parent, JM, Vexler, ZS, Gong, C, Derugin, N and Ferriero, DM. Rat forebrain neurogenesis and striatal neuron replacement after focal stroke. Ann Neurol, 2002. 52 802-13.

37) Erlandsson, A, Lin, CH, Yu, F, Morshead, CM. (2011) Immunosuppression promotes endogenous neural stem and progenitor cell migration and tissue regeneration after ischemic injury. Exp Neurol. 230:48-57.

38) Corbett, D, Nguemeni, C, Gomez-Smith, M. (2014) How can you mend a broken brain? - neurorestorative approaches to stroke recovery. Cerebrovasc Dis. 38:233-239

39) Jin, K, Wang, X, Xie, L, Mao, XO and Greenberg, DA. (2010) Transgenic ablation of doublecortin-expressing cells suppresses adult neurogenesis and worsens stroke outcome in mice. Proc Natl Acad Sci USA. 107:7993-7998.

40) Sun C, Sun H, Wu S, Lee CC, Akamatsu Y, Wang RK, Kernie SG, Liu J. (2013) Conditional ablation of neuroprogenitor cells in adult mice impedes recovery of poststroke cognitive function and reduces synaptic connectivity in the perforant pathway. J Neurosci 33. 17314-17325.

41) Huttner H, Bergmann O, Salehpour M, Rácz A, Tatarishvili J, Lindgren E, Csonka T, Csiba L, Hortobágyi T, Méhes G, Englund E, Solnestam BW, Zdunek S, Scharenberg C, Ström L, Ståhl P, Sigurgeirsson B, Dahl A, Schwab S, Possnert G, Bernard S, Kokaia Z, Lindvall O, Frisén J. The age and genomic integrity of neurons after cortical stroke in humans. Nature Neuro. 2014 17;801-4.

42) Ohab JJ, Fleming S, Blesch A, Carmichael ST. (2006) A neurovascular niche for neurogenesis after stroke. J Neurosci 26: 13007–13016.

43) Seto SW. (2016) Angiogenesis in Ischemic Stroke and Angiogenic effects of Chinese Herbal Medicine. J Clin Med. 5(6): 56.

44) Hayashi T, Noshita N, Sugawara T, Chan PH. (2003) Temporal profile of angiogenesis and expression of related genes in the brain after ischemia. J Cereb Blood Flow Metab. 23: 166–180.

45) Ma F, Morancho A, Montaner J, Rosell A. (2015) Endothelial progenitor cells and revascularization following stroke. Brain Res: 1623:150-9.

46) Moubarik C, Guillet B, Youssef B, Codaccioni JL, Piercecchi MD, Sabatier F, Lionel P, Dou L, Foucault-Bertaud A, Velly L, Dignat-George F, Pisano P. (2011) Transplanted late outgrowth endothelial progenitor cells as cell therapy product for stroke. Stem Cell Rev Rep. 7:208–220.

47) Nih LR, Deroide N, Leré-Déan C, Lerouet D, Soustrat M, Levy BI, Silvestre JS, Merkulova-Rainon T, Pocard M, Margaill I, Kubis N. (2012) Neuroblast survival depends on mature vascular network formation after mouse stroke: role of endothelial and smooth muscle progenitor cell co-administration. Eur J Neurosci. 35:1208–1217.

48) Schweizer S, Meisel A, Märschenz S. (2013) Epigenetic mechanisms in cerebral ischemia. J Cereb Blood Flow Metab. 33(9):1335–46.

49) Narlikar GJ, Fan HY, Kingston RE. (2002) Cooperation between complexes that regulate chromatin structure and transcription. Cell. 108: 475–487.

50) Johnson AB, Barton MC. (2007) Hypoxia-induced and stress-specific changes in chromatin structure and function. Mutat Res. 618: 149–162.

51) Huang Y, Myers SJ, Dingledine R. (1998) Transcriptional repression by REST: recruitment of Sin3A and histone deacetylase to neuronal genes. Nat Neurosci. 2: 867–872.

52) Chen YT, Zang XF, Pan J, Zhu XL, Chen F, Chen ZB, Xu Y. (2012) Expression patterns of histone deacetylases in experimental stroke and potential targets for neuro- protection. Clin Exp Pharmacol Physiol. 39: 751–758.

53) Yan W, Fang Z, Yang Q, Dong H, Lu Y, Lei C, Xiong L.(2013) Sirt1 mediates hyperbaric oxygen preconditioning-induced ischemic tolerance in rat brain. J Cereb Blood Flow Metab. 33: 396–406.

54) Lanzillotta A, Pignataro G, Branca C, Cuomo O, Sarnico I, Benarese M, Annunziato L, Spano P, Pizzi M.(2012) Targeted acetylation of NF-kappaB/RelA and histones by epigenetic drugs reduces post-ischemic brain injury in mice with an extended therapeutic window. Neurobiol Dis. 49C: 177–189.

55) Ren M, Leng Y, Jeong M, Leeds PR, Chuang DM. Valproic acid reduces brain damage induced by transient focal cerebral ischemia in rats: potential roles of histone deacetylase inhibition and heat shock protein induction. J Neurochem. 2004; 89: 1358–1367.

56) Faraco G, Pancani T, Formentini L, Mascagni P, Fossati G, Leoni F, Moroni F, Chiarugi A.(2006) Pharmacological inhibition of histone deacetylases by suberoylanilide hydroxamic acid specifically alters gene expression and reduces ischemic injury in the mouse brain. Mol Pharmacol. 70:1876–1884.

57) Melvin A, Rocha S. (2012) Chromatin as an oxygen sensor and active player in the hypoxia response. Cell Signal. 24: 35–43.

58) Raz L, Zhang QG, Han D, Dong Y, De Sevilla L, Brann DW (2011). Acetylation of the pro-apoptotic factor, p53 in the hippocampus following cerebral ischemia and modulation by estrogen. PLoS One. 6: e27039.

59) Plate KH, Beck H, Danner S, Allegrini PR, Wiessner C. (1998) Cell type specific upregulation of vascular endothelial growth factor in an MCA-occlusion model of cerebral infarct. J Neuropathol Exp Neurol. 58: 654–666.

60) Dore-Duffy P, Owen C, Balabanov R, Murphy S, Beaumont T, Rafols JA. (2012) Pericyte migration from the vascular wall in response to traumatic brain injury. Microvasc. Res. 60:55–69.

61) Ali A, Thériault P, Rivest S (2014) The role of pericytes in neurovascular unit remodeling in brain disorders. Int J Mol Sci. 15(4):6453–74.

62) George S, Kadam SD, Irving ND, Markowitz GJ, Raja S, Kwan A, Tu Y, Chen H, Rohde C, Smith DR, Comi AM. (2013) Impact of trichostatin A and sodium valproate treatment on post-stroke neurogenesis and behavioral outcomes in immature mice. Front Cell Neurosci. 7:123.

63) Shankar TVS, Willems L (2014) Epigenetic modulators mitigate angiogenesis through a complex transcriptomic network. Vascul Pharmacol. 60(2):57–66.

64) Wang Z (2012) Chronic valproate treatment enhances post-ischemic angiogenesis and promotes functional recovery in a rat model of ischemic stroke. Stroke. 43:2430–2436.

65) Yildirim F, Ji S1, Kronenberg G, Barco A, Olivares R, Benito E, Dirnagl U, Gertz K, Endres M, Harms C, Meisel A. (2014) Histone acetylation and CREB binding protein are required for neuronal resistance against ischemic injury. PLoS One. 9(4):e95465.

66) Formisano L, Guida N, Valsecchi V, Cantile M, Cuomo O, Vinciguerra A, Laudati G, Pignataro G, Sirabella R, Di Renzo G, Annunziato L. (2015) Sp3/REST/HDAC1/HDAC2 Complex Represses and Sp1/HIF-1/p300 Complex Activates ncx1 Gene Transcription, in Brain Ischemia and in Ischemic Brain Preconditioning, by Epigenetic Mechanism. J Neurosci. 35(19):7332–7348.

67) Wang F, Marshall CB, Ikura M. (2013) Transcriptional/epigenetic regulator CBP/p300 in tumorigenesis: structural and functional versatility in target recognition. Cell Mol Life Sci. Nov;70(21):3989-4008.

68) Alarcón JM, Malleret G, Touzani K, Vronskaya S, Ishii S, Kandel ER, Barco A. (2004). Chromatin acetylation, memory, and LTP are impaired in CBP+/- mice: a model for the cognitive deficit in Rubinstein-Taybi syndrome and its amelioration. Neuron. 42: 947–959.

69) Bartsch O, Kress W, Kempf O, Lechno S, Haaf T, Zechner U (2010). Inheritance and variable expression in Rubinstein-Taybi syndrome. Am J Med Genet. 152A: 2254–2261.

70) Wang J, Weaver IC, Gauthier-Fisher A, Wang H, He L, Yeomans J, Wondisford F, Kaplan DR, Miller FD. (2010) CBP Histone Acetyltransferase Activity Regulates Embryonic Neural Differentiation in the Normal and Rubinstein-Taybi Syndrome Brain: Dev Cell. 18(1):114-25.

71) Wang J, Gallagher D, DeVito LM, Cancino GI, Tsui D, He L, Keller GM, Frankland PW, Kaplan DR, Miller FD. (2012) Metformin Activates an Atypical PKC-CBP Pathway to Promote Neurogenesis and Enhance Spatial Memory Formation. Cell Stem Cell. 11(1):23–35.

72) Jiang H, Jian SC (2012) CREB-binding protein silencing inhibits thrombin-induced endothelial progenitor cells angiogenesis. Mol Biol Rep. 2773–2779.

73) Chen J, Jiang, Wang L, Hu (2008) Dysregulation of CREB binding protein triggers thrombin-induced proliferation of vascular smooth muscle cells. Mol Cell Biochem. 123–130.

74) Oike, O et al. (2016) Mice Homozygous for a Truncated Form of CREB-Binding Protein Exhibit Defects in Hematopoiesis and Vasculo-angiogenesis. Blood. 93(9):2771–2779.

75) Ashabi G, Khalaj L, Khodagholi F, Goudarzvand M, Sarkaki A. (2014) Pre-treatment with metformin activates Nrf2 antioxidant pathways and inhibits inflammatory responses through induction of AMPK after transient global cerebral ischemia. Metab Brain Dis. 30(3):747-54.

76) Venna VR1, Li J, Hammond MD, Mancini NS, McCullough LD. (2014) Chronic metformin treatment improves post-stroke angiogenesisand recovery after experimental stroke. Eur J Neurosci. 39(12):2129–2138.

77) Liu Y, Tang G, Zhang Z, Wang Y, Yang G-Y (2014) Metformin promotes focal angiogenesis and neurogenesis in mice following middle cerebral artery occlusion. Neurosci Lett 579:46–51.

78) Deng T, Hou YZW, Yuan Y, Shen Z (2016) Pre-stroke Metformin Treatment is Neuroprotective Involving AMPK Reduction. Neurochem Res. In Press.

79) Dadwal P, Mahmud N, Sinai L, Azimi A, Fatt M, Wondisford FE, Miller FD, Morshead CM. (2015) Activating Endogenous Neural Precursor Cells Using Metformin Leads to Neural Repair and Functional Recovery in a Model of Childhood Brain Injury. Stem Cell Reports. 5(2):166–173.

80) Lacoste B, Comin CH, Ben-Zvi A, Kaeser PS, Xu X, Costa Lda F, Gu C. (2015) Sensory-related neural activity regulates the structure of vascular networks in the cerebral cortex. Neuron. 83(5):1117–1130.

81) Balkaya M, Kro JM, Rex A, Endres M. (2012) Assessing post-stroke behavior in mouse models of focal ischemia. J Cereb Blood Flow Metab. 12:330–338.

82) Bouet V, Boulouard M, Toutain J, Divoux D, Bernaudin M, Schumann-Bard P, Freret T.(2009) The adhesive removal test : a sensitive method to assess sensorimotor deficits in mice. Nat Prot. 4(10):1560–1564.

83) Thored P, Arvidsson A, Cacci E, Ahlenius H, Kallur T, Dar- salia V, Ekdahl CT, Kokaia Z, LindvallO. (2006) Persistent production of neurons from adult brain stem cells during recovery after stroke. Stem Cells 24: 739–747.

84) Gouveia A, Hsu K, Niibori Y, Seegobin M, Cancino GI, He L, Wondisford FE, Bennett S, Lagace D, Frankland PW, Wang J.(2016) The aPKC-CBP Pathway Regulates Adult Hippocampal Neurogenesis in an Age-Dependent Manner. Stem Cell Reports (In Press).

85) Trost A, et al. (2016) Brain and Retinal Pericytes : Origin, Function and Role Front Cell Neurosci. 10:1–13.

86) Özen I, Deierborg T, Miharada K, Padel T, Englund E, Genové G, Paul G. (2014) Brain pericytes acquire a microglial phenotype after stroke. Acta Neuropathol. 381–396.

87) Bifari F, Decimo I, Chiamulera C, Bersan E, Malpeli G, Johansson J, Lisi V, Bonetti B, Fumagalli G, Pizzolo G, Krampera M. (2009) Novel stem/progenitor cells with neuronal differentiation potential reside in the leptomeningeal niche. J Cell Mol Med. 13(9B):3195–208.

88) Nakagomi T, Matsuyama T (2010) Ischemia-Induced Neural Stem / Progenitor Cells Within the Post-Stroke Cortex in Adult Brains. Neual Stem Cells and Therapy. 16; 343-358.

89) Nakagomi T, Kubo S2, Nakano-Doi A1, Sakuma R1, Lu S1,3, Narita A1, Kawahara M1,4, Taguchi A5, Matsuyama T1. (2015) Brain Vascular Pericytes Following Ischemia Have Multipotential Stem Cell Activity to Differentiate Into Neural and Vascular Lineage Cells. Stem Cells. 33(6):1962-74.

90) Sarkaki A, Farbood Y, Badavi M, Khalaj L (2015) Metformin improves anxiety-like behaviors through AMPK-dependent regulation of autophagy following transient forebrain ischemia. Metab Brain Dis. 30(5):1139-50.

91) Liang AC, Mandeville ET, Maki T, Shindo A, Som AT, Egawa N, Itoh K, Chuang TT, McNeish JD, Holder JC, Lok J, Lo EH, Arai K. (2016) Effects of Aging on Neural Stem / Progenitor Cells and Oligodendrocyte Precursor Cells After Focal Cerebral Ischemia in Spontaneously Hypertensive Rats. 25:705–714.

92) Chen J, Xu L, Chen S, Yang J (2012) Transcriptional regulation of platelet-derived growth factor-B chain by thrombin in endothelial cells : involvement of Egr-1 and CREB-binding protein. Mol Cell Biochem. 366(1-2):81–87.

93) Lucerna M, Pomyje J, Mechtcheriakova D, Kadl A, Gruber F, Bilban M, Sobanov Y, Schabbauer G, Breuss J, Wagner O, Bischoff M, Clauss M, Binder BR, Hofer E.(2010) Sustained Expression of Early Growth Response Protein-1 Blocks Angiogenesis and Tumor Growth. Cancer Res. 66(13):6708–6713.

Appendix A

First Author Reprints

The paper "The aPKC-CBP Pathway Regulates Adult Hippocampal Neurogenesis in an Age-Dependent Manner" in the journal Stem Cell Reports, published under Elsevier is reproduced in full under the Attribution-NonCommercial-NoDerivatives 4.0 International Creative Commons license.

Stem Cell Reports
Article
ISSCR
OPEN ACCESS

The aPKC-CBP Pathway Regulates Adult Hippocampal Neurogenesis in an Age-Dependent Manner

Ayden Gouveia,[1,2,10] Karolynn Hsu,[1,10] Yosuke Niibori,[5] Matthew Seegobin,[1] Gonzalo I. Cancino,[5] Ling He,[8] Fredric E. Wondisford,[9] Steffany Bennett,[3,4] Diane Lagace,[2,3] Paul W. Frankland,[5,6,7] and Jing Wang[1,2,3,*]
[1]Regenerative Medicine Program, Ottawa Hospital Research Institute, Ottawa, ON K1H 8L6, Canada
[2]Department of Cellular and Molecular Medicine
[3]Brain and Mind Research Institute
[4]Department of Biochemistry, Microbiology and Immunology
University of Ottawa, Ottawa, ON K1H 8M5, Canada
[5]Neurosciences and Mental Health, Hospital for Sick Children, Toronto, ON M5G 1X8, Canada
[6]Department of Psychology
[7]Department of Physiology
University of Toronto, Toronto, ON M5G 1X5, Canada
[8]Division of Metabolism, Department of Pediatrics, Johns Hopkins Medical School, Baltimore, MD 21287, USA
[9]Department of Medicine and Pediatrics, Rutgers-Robert Wood Johnson Medical School, New Brunswick, NJ 08901, USA
[10]Co-first author
*Correspondence: jiwang@ohri.ca
http://dx.doi.org/10.1016/j.stemcr.2016.08.007

SUMMARY

While epigenetic modifications have emerged as attractive substrates to integrate environmental changes into the determination of cell identity and function, specific signals that directly activate these epigenetic modifications remain unknown. Here, we examine the role of atypical protein kinase C (aPKC)-mediated Ser436 phosphorylation of CBP, a histone acetyltransferase, in adult hippocampal neurogenesis and memory. Using a knockin mouse strain (*Cbp*S436A) in which the aPKC-CBP pathway is deficient, we observe impaired hippocampal neuronal differentiation, maturation, and memory and diminished binding of CBP to CREB in 6-month-old *Cbp*S436A mice, but not at 3 months of age. Importantly, elevation of CREB activity rescues these deficits, and CREB activity is reduced whereas aPKC activity is increased in the murine hippocampus as they age from 3 to 6 months regardless of genotype. Thus, the aPKC-CBP pathway is a homeostatic compensatory mechanism that modulates hippocampal neurogenesis and memory in an age-dependent manner in response to reduced CREB activity.

INTRODUCTION

Newborn neurons are continuously generated throughout life in several areas of the mammalian brain, including the subgranular zone (SGZ) of the hippocampal dentate gyrus (Imayoshi et al., 2008; Palmer et al., 1997; Zhao et al., 2008). Adult hippocampal neurogenesis is essential for neuronal addition and hippocampal growth, potentially contributing to new memory formation during adulthood (Deng et al., 2010; Dupret et al., 2007; Imayoshi et al., 2008; Sahay et al., 2011; Saxe et al., 2006). Adult neural precursor cells (NPCs) in the SGZ predominantly give rise to transit-amplifying cells and neuroblasts, which ultimately generate granule neurons in the hippocampal dentate gyrus (Ming and Song, 2011; Toni et al., 2008; Wang et al., 2012; Zhao et al., 2008). An early and dramatic decline in hippocampal neurogenesis that occurs in mice during early adulthood (3–6 months) is associated with a reduction in neural progenitor proliferation and newborn neuron survival (Kuipers et al., 2015). In contrast, the rate of neuronal differentiation is constant during early adulthood and remains sustained even in older (1–1.5 years old) mice (Kuipers et al., 2015). Disruption of this ongoing neurogenesis has been proposed to play a role in progressive neurodegenerative disorders such as Alzheimer's disease (Mu and Gage, 2011; Winner et al., 2011; Zhao et al., 2008). Therefore, understanding the underlying molecular mechanisms that sustain the age-dependent hippocampal neurogenesis will provide a fundamental basis to elucidate the pathogenesis and therapeutic targets of Alzheimer's disease.

We previously showed that an atypical protein kinase C-CREB binding protein (aPKC-CBP) pathway is important for the differentiation of embryonic NPCs into all three neural cell lineages: neurons, astrocytes, and oligodendrocytes (Wang et al., 2010). Specifically, we demonstrated that activation of aPKC leads to Ser436 phosphorylation in CBP, a histone acetyltransferase, and that this phosphorylation causes transcription of genes that are associated with the three cell lineages. Moreover, we demonstrated that metformin, an AMP kinase (AMPK) activator, could activate the aPKC-CBP pathway to promote neurogenesis and enhance spatial memory formation in adult mice (Wang et al., 2012; Fatt et al., 2015). Interestingly, another recent study demonstrated that CBP is required for enriched environment-induced adult

This is an open access article under the CC BY-NC-ND license (http://creativecommons.org/licenses/by-nc-nd/4.0/).

hippocampal neurogenesis and learning and memory (Lopez-Atalaya et al., 2011). Together, these findings suggest that CBP-mediated epigenetic regulation plays a central role in integrating environmental/microenvironmental changes to the determination of NPC differentiation in the developing and adult brain.

The specificity of CBP actions is determined by its transcription factor binding partners. One of the binding partners is CREB (cyclic AMP response element binding protein), which is known to play a central role in regulating hippocampal plasticity, neurogenesis, and memory formation (Merz et al., 2011; Mizuno et al., 2002; Nakagawa et al., 2002a; Silva et al., 1998). When CREB is phosphorylated at Ser133, it recruits CBP and positively regulates CREB-mediated gene transcription (Parker et al., 1996; Shih et al., 1996). Intriguingly, the phosphorylated CREB at Ser133 (pS133-CREB) is stably expressed in doublecortin (DCX)-positive neuroblasts/newborn neurons in the hippocampal SGZ, suggesting its central role in neuronal differentiation and/or maturation (Merz et al., 2011). Moreover, previous work in liver cells has shown that aPKC-dependent Ser436 phosphorylation of CBP can regulate its association with CREB (He et al., 2009). These findings led us to test the hypothesis that activation of the aPKC-CBP pathway may modulate hippocampal neurogenesis and memory formation by regulating the association of CBP with CREB in the hippocampus.

Our findings show that the aPKC-CBP pathway is required for hippocampal neuronal differentiation and maturation and hippocampal-dependent memory in mature adult (6 months old) mice, but not in young adult (3 months old) mice. Mechanistically, we found that the aPKC-CBP pathway is highly upregulated and is necessary to maintain the association of CBP with CREB in the hippocampus of mature mice when CREB activity (pS133-CREB) is reduced. More importantly, elevation of CREB activity (pS133-CREB) by a phosphodiesterase 4 (PDE4) inhibitor, rolipram, in the hippocampus can rescue the neuronal differentiation and maturation deficits in mature mice. This rescue is also accompanied by restoring impaired pre-exposure fear memory and the diminished binding of CBP to CREB in *Cbp*S436A mice. Together, these data argue that the aPKC-CBP pathway has a compensatory homeostatic role in modulating hippocampal neurogenesis and hippocampal-dependent memory during early adulthood (3–6 months).

RESULTS

The aPKC-CBP Pathway Regulates Adult Neurogenesis

To ask whether the aPKC-mediated CBP S436 phosphorylation is important for adult hippocampal neurogenesis, we took advantage of a phosphor-mutant *Cbp*S436A knockin (*Cbp*S436A-KI) mouse strain in which the aPKC-CBP pathway is deficient due to the exchange of the serine (S) 436 residue for an alanine (A) residue in CBP. *Cbp*S436A-KI mice survive into adulthood, and do not exhibit any apparent changes in brain structure (data not shown). To assess adult hippocampal neurogenesis, we injected 3- and 6-month-old mice with bromodeoxyuridine (BrdU) (100 mg/kg, intraperitoneally) daily for 3 consecutive days, and euthanized the mice 12 days after the first BrdU injection. Hippocampi were analyzed by immunostaining for BrdU and the mature neuron marker NEUN. Quantification throughout the extent of the hippocampal dentate gyrus demonstrated a significant decrease in the total number of BrdU/NEUN-positive neurons in *Cbp*S436A-KI mice at both ages (Figures 1A and 1B).

To explore cellular mechanisms underlying the reduction in neurogenesis in the *Cbp*S436A-KI mice, we first investigated whether the number of proliferating NPCs was decreased using the proliferation marker, Ki-67. This analysis demonstrated that the number of Ki-67-positive proliferating NPCs in the SGZ was unchanged in *Cbp*S436A-KI mice at both 3 and 6 months of age (Figures 1C and 1D). We further immunostained sections for an apoptotic marker, cleaved caspase-3 (CC3), and a marker for neuroblasts/newborn neurons, doublecortin (DCX) (Figures 1E and 1F). We observed that ~80% of CC3-positive cells are DCX-positive neuroblasts/newborn neurons. Although the basal level of CC3-positive dying cells was low in wild-type (WT) mice (total 30–50 cells throughout the extent of hippocampus) at both ages, the number of DCX/CC3-positive cells was significantly increased in *Cbp*S436A-KI mice at the age of 3 months, but not 6 months (Figures 1E and 1F). These results suggest that young adult *Cbp*S436A-KI mice have a reduction in survival of newborn neurons, in the absence of changes in proliferation.

To further confirm that newborn cell survival was decreased in 3-month-old *Cbp*S436A-KI mice, we performed BrdU in vivo chasing experiments by quantifying the total number of surviving BrdU-positive cells at 1, 12, and 30 days following BrdU injections. Relative to their WT littermates, *Cbp*S436A-KI mice had no change in the total number of 1-day-old BrdU cells (Figures 1G and 1H), in agreement with no change in the proliferating Ki-67-positive cells (Figures 1C and 1D). In addition, consistent with less newborn cell survival (Figures 1E and 1F), there was a significant decrease in the total number of 12- and 30-day-old BrdU-positive cells in 3-month-old *Cbp*S436A-KI mice (Figures 1G and 1H). Further quantification of the number of BrdU/NEUN-positive neurons 30 days after BrdU labeling showed a sustained reduction in hippocampal neurogenesis in both 3- and 6-month-old *Cbp*S436A-KI mice (Figures 1I and 1J). We then assessed whether the

reduction in hippocampal neurogenesis was associated with a general decrease of adult neurogenesis by analyzing the same mice for olfactory bulb neurogenesis. The total number of adult-born BrdU/NEUN-positive neurons in the olfactory bulb was proportionately decreased in the 3-month-old *Cbp*S436A-KI mice (Figures S1A and S1B). Together, these findings suggest that a reduction of neurogenesis in young adult *Cbp*S436A-KI mice (3 months) is at least partly due to an increase in the death of neuroblasts/newborn neurons.

The aPKC-CBP Pathway Regulates Adult Hippocampal Neuronal Differentiation and Maturation in an Age-Dependent Manner

Since the aPKC-CBP pathway has been identified as a pro-differentiation pathway during embryonic brain development (Tsui et al., 2014; Wang et al., 2010), we determined whether the aPKC-CBP pathway also regulates hippocampal neuronal differentiation, thus contributing to the reduction in hippocampal neurogenesis in the young (3-month) and older (6-month) mice (Figures 1A and 1B). Using the 12-day BrdU chasing paradigm previously described, *Cbp*S436A-KI had a significant reduction in the proportion of newborn mature neurons to the total BrdU-labeled cells (% NEUN/BrdU$^+$ over BrdU$^+$) at the age of 6 months, but no change at 3 months (Figures 2A and 2B). The fact that the total number of BrdU-positive cells was unaltered in 6-month-old *Cbp*S436A-KI mice (Figure S2A) argues that the decreased rate of hippocampal neurogenesis (Figures 2A and 2B) likely contributes to the reduced hippocampal neurogenesis at the age of 6 months in *Cbp*S436A-KI mice (Figures 1A and 1B). Next, we stained sections from the same experiments with a neural precursor marker, SOX2, and BrdU. The proportion of SOX2$^+$ NPCs over total BrdU-labeled cells (% SOX2/BrdU$^+$ over BrdU$^+$) was significantly increased in *Cbp*S436A-KI mice at the age of 6 months but not 3 months (Figures 2C and 2D), corresponding to the decreased proportion of newborn neurons in *Cbp*S436A-KI mice at 6 months. We further assessed other types of NPCs, including GFAP$^+$ type 1 NPCs and TBR2$^+$ type 2/3 NPCs in 6-month-old *Cbp*S436A-KI mice. Under our experimental conditions, we observed a small population of BrdU/GFAP co-labeled cells located in the SGZ and did not detect BrdU/GFAP co-labeled hilar astrocytes. Quantitative analysis showed that the population of BrdU/GFAP/SOX2$^+$ type 1 NPCs was not changed in *Cbp*S436A-KI mice (Figures S2B and S2C). However, the proportion of TBR2$^+$ NPCs over total BrdU-labeled cells (% TBR2/BrdU$^+$ over BrdU$^+$) was significantly increased in *Cbp*S436A-KI mice at 6 months (Figures 2E and 2F). Further quantification from triple-stained sections for TBR2, SOX2, and BrdU showed that the proportion of both SOX2$^+$/TBR2$^+$ type 2a and SOX2$^-$/TBR2$^+$ type 2b/3 NPCs was elevated in 6-month-old *Cbp*S436A-KI mice (Figures 2E and 2F). These results revealed that lack of Ser436 phosphorylation in CBP leads to the impaired development of hippocampal NPCs at the age of 6 months by arresting them at the stage of TBR2- and or/SOX2-positive NPCs. Together, these data suggest that the aPKC-CBP pathway is required to maintain the sustained neuronal differentiation of hippocampal NPCs in mature adults (6 months).

We further assessed the population of DCX-positive neuroblasts/newborn neurons in *Cbp*S436A-KI mice. The total number of DCX-positive cells was not significantly different between WT and *Cbp*S436A-KI mice (Figures S2D and S2E) at either 3 or 6 months of age. We then examined BrdU-labeled DCX-positive cells at both ages. The proportion of BrdU-positive cells that express DCX (% DCX/BrdU$^+$ over BrdU$^+$) was not changed in *Cbp*S436A-KI mice at both 3 and 6 months (Figures 2G and 2H). In contrast, the total number of co-labeled BrdU/DCX-positive cells was decreased in 3-month-old *Cbp*S436A-KI (Figure S2F), as expected due to the reduced total number of BrdU-positive cells (Figures 1G, 1H, and S2A).

The reduced rate of neuronal differentiation combined with the unaltered number and proportion of DCX-positive cells at the age of 6 months in the *Cbp*S436A-KI mice led us to hypothesize that these mice may have an impaired neuronal maturation process, manifested by the reduced acquisition of a mature neuron phenotype in DCX-positive neuroblasts/newborn neurons. We tested this hypothesis by performing triple staining with BrdU, NEUN, and DCX in 3- and 6-month-old brain sections. As we expected, the proportion of mature neurons (NEUN$^+$) in the BrdU/DCX-positive cells (% NEUN/BrdU/DCX$^+$ over BrdU/DCX$^+$ cells) was significantly decreased in 6-month-old *Cbp*S436A-KI mice (Figures 3A and 3B), indicating the reduced acquisition rate of mature neuron phenotype (NEUN$^+$) in the total newborn neurons. Consistent with this, the proportion of maturing neurons (% NEUN$^+$/DCX$^+$ over BrdU$^+$ cells) (Figure 3C) as well as mature neurons that had exited the immature stage (% NEUN$^+$/DCX$^-$ over BrdU$^+$ cells) (Figure 3D) was significantly reduced. In contrast, the percentage of BrdU-labeled DCX-positive, NEUN-negative neuroblasts/immature neurons (% DCX$^+$/NEUN$^-$ over BrdU$^+$ cells) was increased in 6 month-old *Cbp*S436A-KI mice (Figure 3E). There was also a significant increase in the percentage of BrdU-positive cells that were both NEUN and DCX negative (% NEUN$^-$/DCX$^-$ over BrdU$^+$ cells), representing the NPC population (Figure 3F). Thus, all of these data argue that the aPKC-CBP pathway is required for both neuronal differentiation and maturation in mature adult hippocampi (6 months) (Figure 3G).

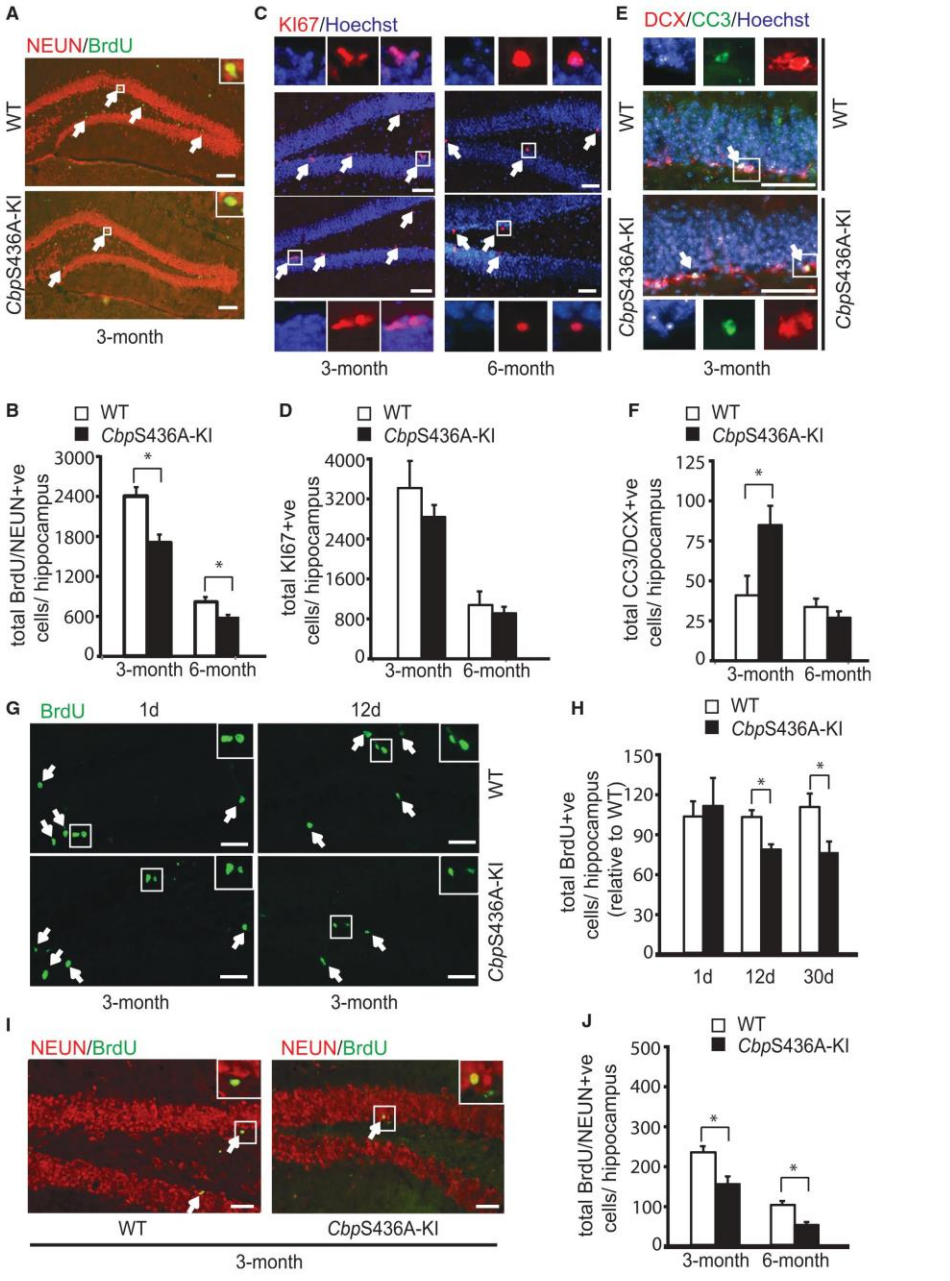

(legend on next page)

The aPKC-CBP Pathway Regulates Hippocampal-Dependent Fear Memory and Spatial Memory in Mature Adult Mice

Adult hippocampal neurogenesis plays a key role in hippocampal-dependent fear memory and spatial memory (Kee et al., 2007; Imayoshi et al., 2008; Saxe et al., 2006). Here we first used a context pre-exposure task, a version of contextual fear memory that is critically dependent on the hippocampus (Matus-Amat et al., 2004; Rudy et al., 2004), and is sensitive to detect deficits in adult neurogenesis (Cancino et al., 2013). In this task, the mice were first exposed to the context 24 hr before the foot shock to temporally separate the context acquisition phase from the association of the context with the shock (Figure 4A), unlike traditional context fear-conditioning experiments where the shock is introduced immediately after context exposure. Only animals that were pre-exposed to the context show high levels of freezing when subsequently tested (Fanselow, 2000). Consistent with an age-dependent reduction in hippocampal neuronal differentiation and maturation, the *Cbp*S436A-KI mice showed low freezing at 6 months but not at 3 months of age when compared with their respective WT littermates (Figures 4A and S3A).

We then used a hidden-platform version of the Morris water maze (MWM) task to measure spatial learning and memory in 6-month-old *Cbp*S436A-KI mice and their WT littermates. We showed that both WT and *Cbp*S436A-KI mice had a comparable learning curve over 7 days despite higher overall escape latency in *Cbp*S436A-KI mice (Figure 4B). We also analyzed the search strategies that the mice used through a visual algorithm analysis (Granger et al., 2016) to assess when the mice switched from a systematic to a spatial search strategy. We found that *Cbp*S436A-KI mice switched from systematic to spatial search strategies by training day 6, which was delayed compared with their WT littermates that switched by training day 4 (Figures 4C and 4D). Following the 7-day training session, probe tests were assessed at day 8 and day 19 by removing the platform from the swimming pool. At day 8, 24 hr after the last training, we observed that both *Cbp*S436A-KI and their WT littermates spent significantly more time in the target quadrant than in other three quadrants (Figure 4E), indicating normal short-term memory in *Cbp*S436A-KI mice. During the late probe test at day 19 (12 days after training), WT mice still spent significantly more time in the target quadrant relative to the other three quadrants while *Cbp*S436A-KI mice did not show a specific preference for the target quadrant (Figure 4F), suggesting impaired long-term spatial memory in *Cbp*S436A-KI mice. Finally, there was no difference in thigmotaxic swim patterns manifesting anxiety behaviors between WT and *Cbp*S436A-KI mice, implying that anxiety was not accountable for the impaired spatial learning and memory (Figures S3B–S3D). In addition, both WT and

Figure 1. Adult Mice Lacking CBPS436 Phosphorylation Show a Reduction in Adult Neurogenesis

(A) Fluorescence images of hippocampal sections from 3-month-old *Cbp*S436A (*Cbp*S436A-KI) and their wild-type littermates (WT), euthanized 12 days after BrdU injections and stained for BrdU (green) and NEUN (red). The insets show the boxed areas at higher magnification. Arrows represent double-labeled BrdU/NEUN-positive neurons. Scale bar, 100 μm.

(B) Quantitative analysis of the total number of BrdU/NEUN-positive newborn neurons in the hippocampi from 3- to 6-month-old WT and *Cbp*S436A-KI mice. *$p < 0.05$ ($n = 4–5$ animals for each group).

(C) Fluorescence images of hippocampal sections from 3- to 6-month-old WT and *Cbp*S436A-KI mice, immunostained for Ki-67 (KI67; red) and counterstained with Hoechst 33342 (blue). The boxed areas are shown at higher magnification in the top and bottom panels. Arrows denote Ki-67-positive proliferating cells. Scale bars, 50 μm.

(D) Quantitative analysis of the total number of Ki-67-positive proliferating cells in the hippocampi from 3- to 6-month-old *Cbp*S436A-KI and their WT littermates ($n = 4$ animals for each group).

(E) Fluorescence images of hippocampal sections from 3-month-old WT and *Cbp*S436A-KI mice, stained for cleaved caspase 3 (CC3) (green) and DCX (red). The boxed areas are shown at higher magnification in the top and bottom panels. Arrows denote double-labeled CC3/DCX-positive cells. Scale bars, 50 μm.

(F) Quantitative analysis of the total number of CC3/DCX-positive cells in the hippocampi from 3- to 6-month-old *Cbp*S436A-KI and their WT littermates. *$p < 0.05$ ($n = 4$ animals for each group).

(G) Fluorescence images of hippocampal sections from 3-month-old WT and *Cbp*S436A-KI mice 1 day and 12 days after BrdU injections, stained for BrdU (green). The insets show the boxed areas at higher magnification. Arrows denote BrdU-positive cells. Scale bars, 25 μm.

(H) Quantitative analysis of the total number of BrdU-positive cells in the hippocampi from 3-month-old WT and *Cbp*S436A-KI mice 1 day, 12 days, and 30 days following BrdU injections. *$p < 0.05$ ($n = 3–5$ animals for each group).

(I) Fluorescence images of hippocampal sections from 3-month-old WT and *Cbp*S436A-KI mice, euthanized 30 days after BrdU injections, and stained for BrdU (green) and NEUN (red). The insets show the boxed areas at higher magnification. Arrows represent double-labeled BrdU/NEUN-positive neurons. Scale bars, 25 μm.

(J) Quantitative analysis of the total number of BrdU/NEUN-positive neurons in the hippocampi from 3- to 6-month-old WT and *Cbp*S436A-KI mice. *$p < 0.05$ ($n = 4–5$ animals for each group).

Error bars represent SEM. See also Figure S1.

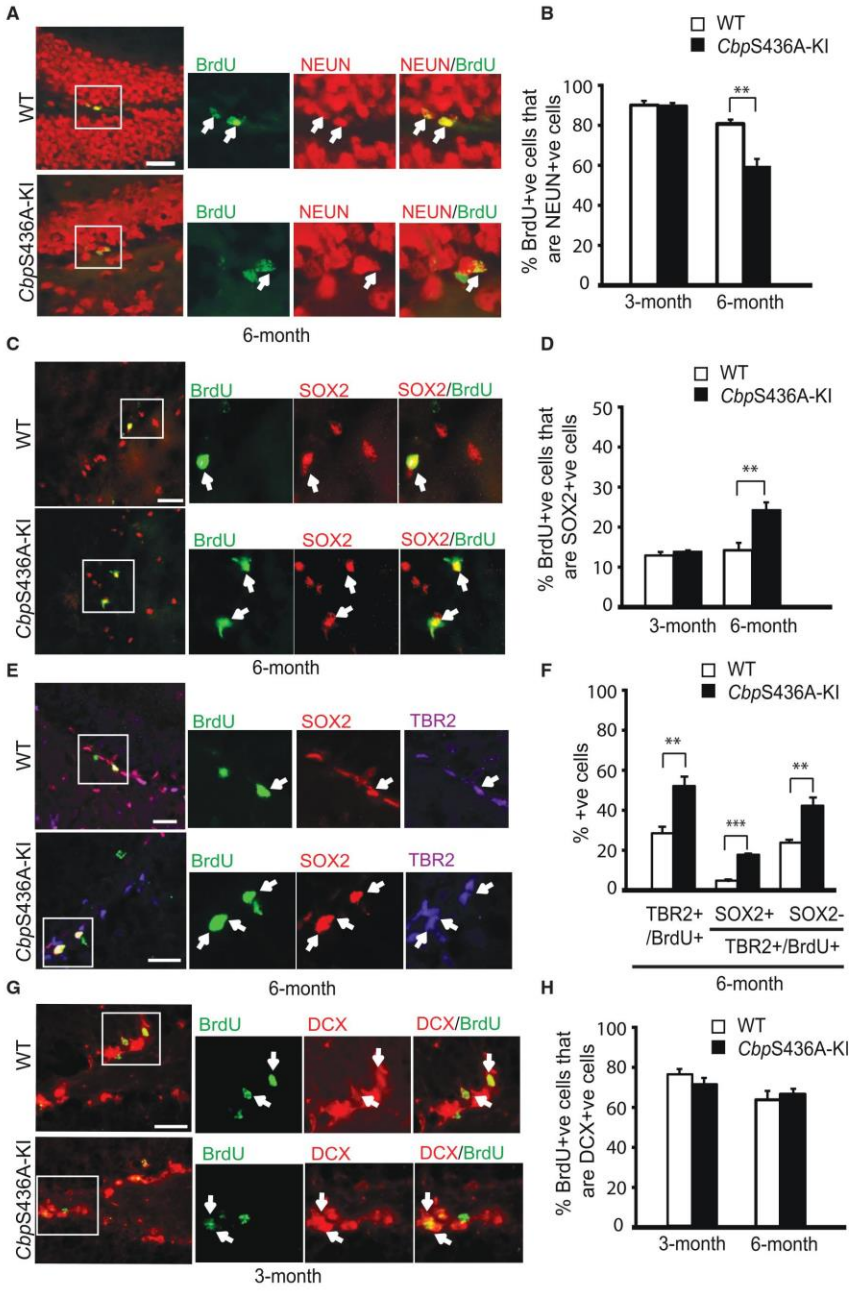

(legend on next page)

*Cbp*S436A-KI mice showed normal mean velocity, distance traveled, and anxiety behaviors in the open field (Figures 4G, S3E, and S3F), making it unlikely that the spatial and contextual memory deficits are attributable to non-specific impairments in motor function or increases in anxiety. Together, these data suggest that the aPKC-CBP pathway is essential for the regulation of age-dependent hippocampal-dependent fear and spatial learning and memory.

The aPKC-CBP Pathway Regulates CBP Binding to CREB in an Age-Dependent Manner

CREB is a major regulator of adult hippocampal neurogenesis and hippocampal-dependent learning and memory (Merz et al., 2011; Mizuno et al., 2002; Silva et al., 1998). Here, we assessed the ability of CBP to bind to CREB in *Cbp*S436A-KI hippocampal tissues at both 3 and 6 months of age using a co-immunoprecipitation assay. A reduction of the association of CBP with CREB was observed in hippocampal extracts obtained from mature (6 months old) but not young (3 months old) *Cbp*S436A-KI mice (Figures 5A and 5B). We further assessed the phosphorylation status of CREB at S133 (pS133-CREB), which is known to be a rate-limiting step in the association of CREB with CBP, and the level of aPKC activity, manifested by phosphorylation of threonine (pT)410/403-aPKC. Western blot analysis showed that WT mice exhibited a significant reduction in pS133-CREB and a robust enhancement in pT410/403-aPKC in hippocampal extracts as mice aged from 3 to 6 months (Figures 5C and 5D). *Cbp*S436A-KI mice similarly had a reduction in pS133-CREB and enhancement in pT410/403-aPKC with aging, although the basal level of pS133-CREB is slightly higher at 3 months in *Cbp*S436A-KI than in WT mice (Figures 5C and 5D). Furthermore, we confirmed that the protein levels of total CREB and aPKC remained unchanged between 3 and 6 months of age in the WT and *Cbp*S436A-KI mice (Figure 5E). These results suggest a model in which the aPKC-CBP pathway plays a compensatory role to maintain the interaction between CBP and CREB in mature adult hippocampi (6 months) in response to a reduced level of pS133-CREB. When the aPKC-CBP pathway is deficient in *Cbp*S436A-KI mice, the association of CBP with CREB is diminished in mature adult hippocampi (6 months) due to lack of phosphorylation in both CREB-S133 and CBP-S436, although the upstream kinase aPKC activity is highly upregulated.

Elevation of CREB Phosphorylation Rescues Neurogenesis Deficits, Impairs Fear Memory, and Restores CBP Binding to CREB in Mature Adult *Cbp*S436A Mice

To further test the model, we asked whether the elevation of pS133-CREB would rescue the cellular, molecular, and behavioral deficits observed in mature adult *Cbp*S436A-KI mice (6 months old). To do this we injected rolipram (1.25 mg/kg/day, intraperitoneally), a specific PDE4 inhibitor, for 14 days in vivo. As expected, we found that rolipram treatment increased pS133-CREB expressions as detected by western blot analysis in 6-month-old WT and *Cbp*S436A-KI hippocampal tissues (Figures 6A and 6B). Notably, immunohistochemistry analysis further showed that pS133-CREB is highly expressed in the hippocampal SGZ and most pS133-CREB positive cells in the hippocampi are DCX-positive cells (Figure S4A), supporting the transcription factor's role in the acquisition and maturation of DCX-positive neuroblasts/newborn neurons. Quantification of pS133-CREB-positive cells in the dentate gyrus indicated that rolipram treatment significantly increased the number of pS133-CREB positive cells in the 6-month-old hippocampal SGZ (Figure S4B), further validating the western blot analysis (Figures 6A and 6B).

To assess neurogenesis, we administered rolipram injections (1.25 mg/kg/day, intraperitoneally) for 14 days; BrdU co-injections were given at days 3–5 (100 mg/kg/day, intraperitoneally), and mice were euthanized at the end of 14 days to follow the same 12-day BrdU chasing

Figure 2. Mature Adult Mice Lacking CBPS436 Phosphorylation Show Reduced Hippocampal Neuronal Differentiation

Adult mice (3 and 6 months old) received BrdU (100 mg/kg) injections for 3 consecutive days, and were euthanized for immunostaining analysis 12 days after the first BrdU injection.

(A, C, E, and G) Fluorescence images of hippocampal sections from 6-month-old (A,C,E) and 3-month-old (G) WT and *Cbp*S436A-KI mice, stained for: (A) BrdU (green) and NEUN (red); (C) BrdU (green) and SOX2 (red); (E) BrdU (green), TBR2 (purple), and SOX2 (red); and (G) BrdU (green) and DCX (red). Arrows denote double-labeled cells. The boxed areas are shown at higher magnification on the right. Scale bars, 25 μm.

(B) Quantitative analysis of the percentage of BrdU-positive cells that express a mature neuron marker, NEUN, in the hippocampi from 3- to 6-month-old WT and *Cbp*S436A-KI mice. $^{**}p < 0.01$ (n = 4 animals for each group).

(D) Quantitative analysis of the percentage of BrdU-positive cells that were positive for SOX2 in the hippocampi from WT and *Cbp*S436A-KI mice at the ages of 3 and 6 months. $^{**}p < 0.01$ (n = 4 animals for each group).

(F) Quantitative analysis of the percentage of BrdU-positive cells that were positive for TBR2 and SOX2 in the hippocampi from WT and *Cbp*S436A-KI mice at 6 months. $^{**}p < 0.01$, $^{***}p < 0.001$ (n = 4 animals for each group).

(H) Quantitative analysis of the percentage of BrdU-positive cells that express DCX in the hippocampi from 3- to 6-month-old WT and *Cbp*S436A-KI mice (n = 4 animals for each group).

Error bars represent SEM. See also Figure S2.

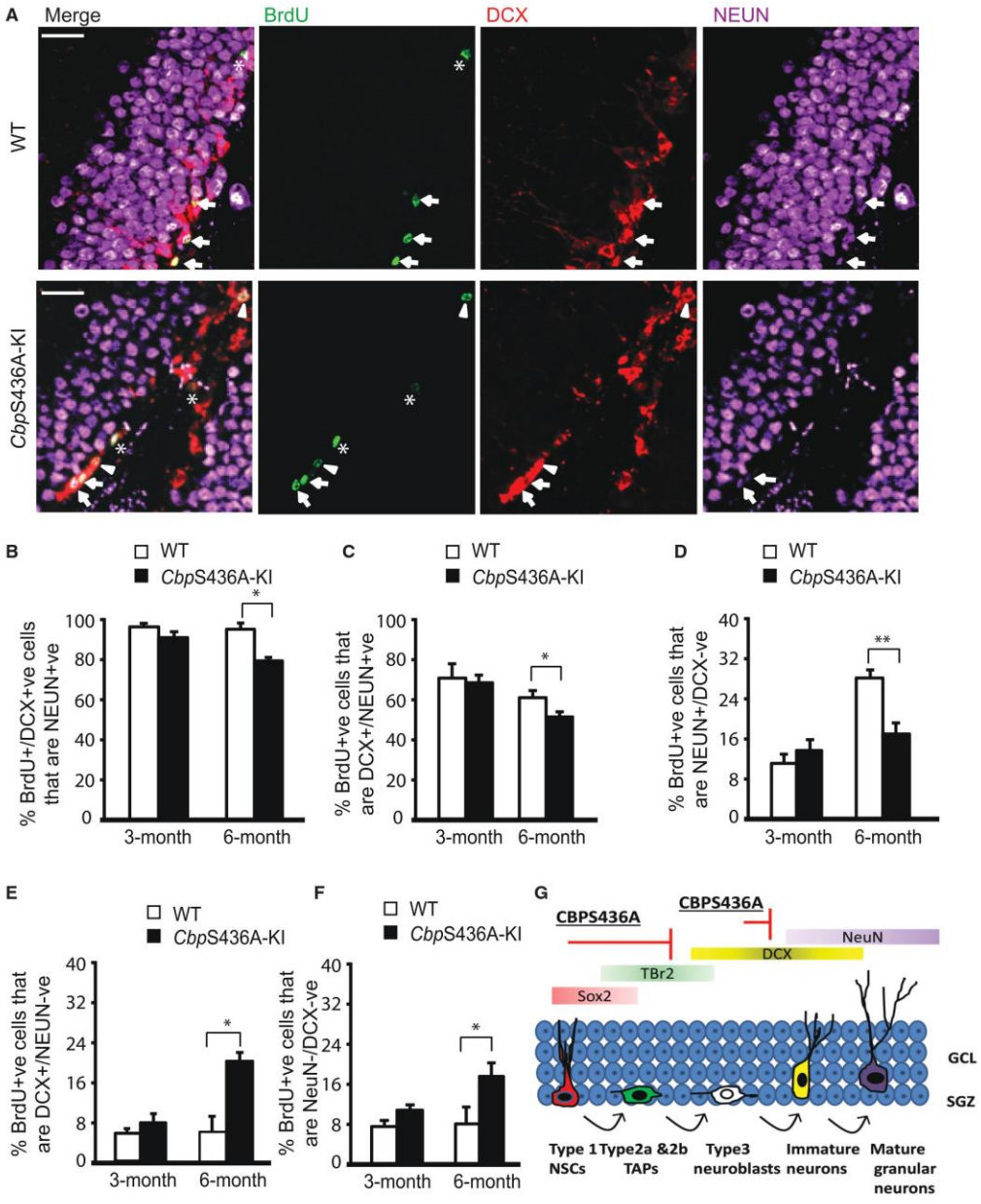

(legend on next page)

paradigm (Figure 3). Quantification of the proportion of BrdU/NEUN-positive neurons showed that rolipram treatment rescued the neurogenesis deficit observed in 6-month-old *Cbp*S436A-KI mice (Figures 6C and 6D). Further triple-labeling experiments (BrdU/DCX/NEUN) showed that the deficits from both neuronal differentiation (Figure 6F, the proportion of BrdU-positive cells that are negative for DCX and NEUN) and maturation (Figures 6G–6I, acquisition of NEUN-positive mature neurons in BrdU/DCX-positive immature cells) processes in 6-month-old *Cbp*S436A-KI mice were rescued by rolipram treatment. In addition, we also found that rolipram treatment increased the total number of Ki-67-positive proliferating cells in both WT and *Cbp*S436A-KI mice to the same extent (Figures S4C and S4D). Consistent with this, the proportion of BrdU-labeled DCX-positive cells was significantly increased by rolipram treatment in both WT and *Cbp*S436A-KI mice to the same extent (Figure S4E), while the total number of BrdU-positive cells was unchanged (Figure S4F). These results show that rolipram not only increases the proliferation and the population of BrdU-labeled DCX-positive cells regardless of genotype, but also prevents the neuronal differentiation and maturation deficits observed in *Cbp*S436A-KI mice.

We then asked whether rolipram treatment would restore the impaired fear memory of *Cbp*S436A-KI mice. Indeed, 21 days of rolipram treatment was capable of rescuing the impaired pre-exposure context fear memory (Figure 6J). Finally, co-immunoprecipitation assay showed that 14-day rolipram treatment rescued the impaired interaction between CBP and CREB in 6-month-old *Cbp*S436A-KI mice (Figures 6K–6L). Thus, these data support the concept that pS436-CBP is a compensatory mechanism in response to reduced pS133-CREB expression to maintain hippocampal neurogenesis, hippocampal-dependent fear memory, and the association of CBP with CREB in mature adult mice.

DISCUSSION

Our present data demonstrate four key events that are mediated by the aPKC-CBP pathway: (1) neurogenesis in young adult mice (3 months old) by, at least in part, preventing the death of newborn neurons; (2) maintenance of a stable rate of hippocampal neuronal differentiation and maturation in mature adult mice (6 months old); (3) formation of hippocampal-dependent fear memory and maintenance of spatial learning and memory in mature adult mice (6 months old); and (4) maintenance of the association of CBP with CREB in mature adult hippocampi (6 months old), when CREB activity/pS133-CREB is significantly reduced. Importantly, elevation of pS133-CREB expression in vivo rescues the impaired phenotypes at the cellular, behavioral, and molecular levels in mature adult *Cbp*S436A-KI mice where the aPKC-CBP pathway is deficient. Hence, our study strongly argues that the aPKC-CBP pathway is a homeostatic intrinsic mechanism that maintains a sustained rate of hippocampal neurogenesis and hippocampal-dependent memory in response to reduced CREB activity during early adulthood (3–6 months).

Originally, we identified the aPKC-CBP pathway as a pro-differentiation pathway during embryonic cerebral cortex development (Wang et al., 2010). Enriched neural developmental cues during cortex development converge on the aPKC-CBP pathway to promote the differentiation of embryonic NPCs into three neural cell lineages. Here, we ask a different question as to whether aPKC-mediated CBP phosphorylation/activation is a homeostatic signaling cascade that modulates adult hippocampal neurogenesis. Interestingly, recent research indicates that an early and dramatic decline in hippocampal neurogenesis during early adulthood (3–6 months) is primarily due to a decrease in neural progenitor proliferation and newborn neuron survival in the absence of any large changes in neuronal

Figure 3. Mature Adult Mice Lacking CBPS436 Phosphorylation Show Impaired Hippocampal Neuronal Maturation

Adult mice (6 months old) received BrdU (100 mg/kg) injections for 3 consecutive days, and were euthanized 12 days after the first BrdU injection.

(A) Confocal Images of coronal hippocampal dentate gyrus sections from 6-month-old WT and *Cbp*S436A-KI mice, stained for BrdU (green), DCX (red), and NEUN (purple). Arrows denote triple-labeled $BrdU^+/DCX^+/NEUN^+$ cells; arrowheads denote double-labeled $BrdU^+/DCX^+/NEUN^-$ cells; asterisks denote single-labeled $BrdU^+/DCX^-/NEUN^-$ cells. Scale bars, 20 μm.

(B–F) Quantitative analysis of the percentage of BrdU/DCX-positive cells that also express NEUN (B); the percentage of BrdU-positive cells that were positive for both NEUN and DCX (C); the percentage of BrdU-positive cells that were positive for NEUN but negative for DCX (D); the percentage of BrdU-positive cells that express DCX but not NEUN (E); and the percentage of BrdU-positive cells that were negative for both NEUN and DCX (F) in the hippocampi from 3- to 6-month-old WT and *Cbp*S436A-KI mice. $^*p < 0.05$, $^{**}p < 0.01$ ($n = 4$ animals for each group).

(G) Schematic representation showing that *Cbp*S436A mutation not only arrests the NPC development at SOX2 and/or $TBR2^+$ NSCs/TAPs but also inhibits neuronal maturation from DCX^+ cells to $NEUN^+$ mature neurons in 6-month-old adult mice. NSCs, neural stem cells; TAPs, transient amplifying progenitors.

Error bars represent SEM.

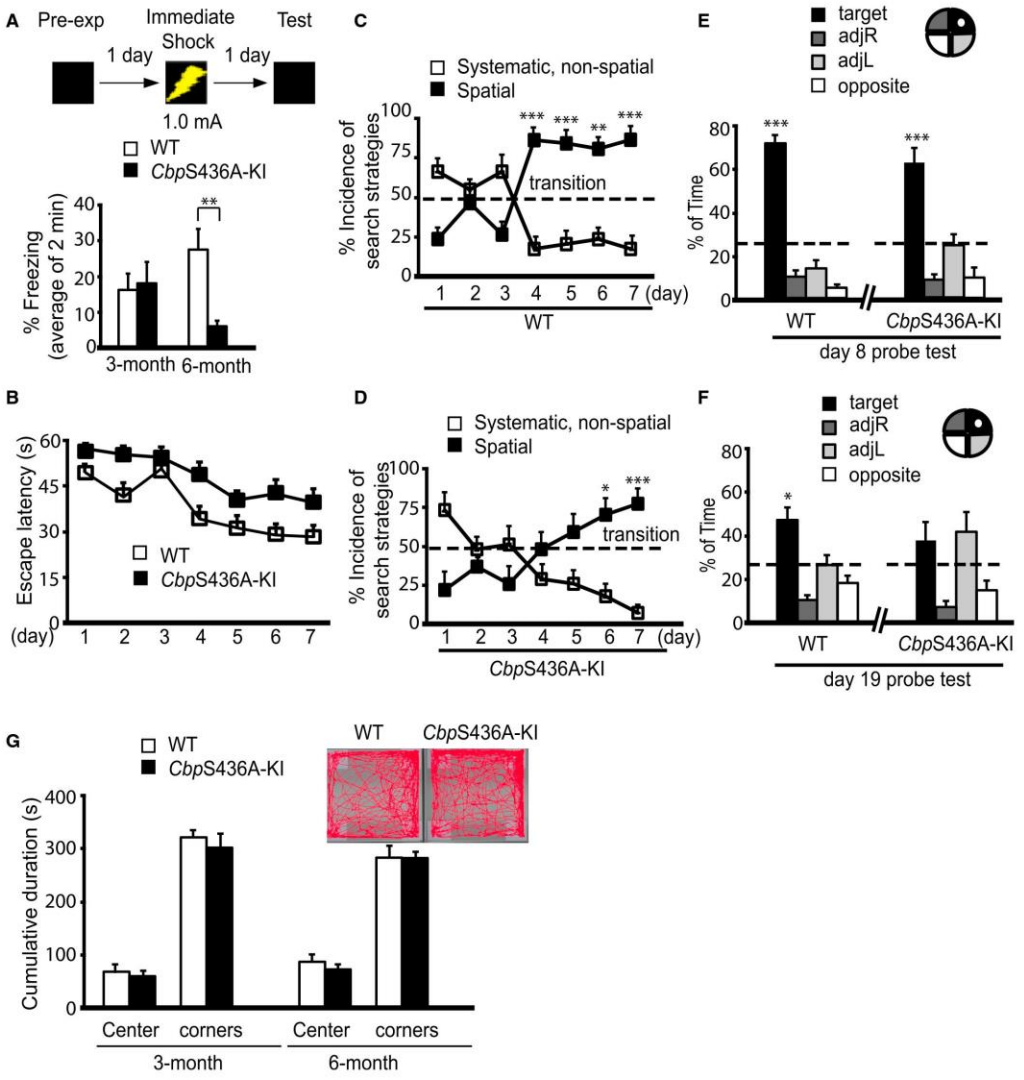

Figure 4. Mature Adult Mice Lacking CBPS436 Phosphorylation Display Impaired Pre-exposure Contextual Fear Memory and Deficits in Spatial Learning and Memory

(A) Both 3- and 6-month-old WT and *Cbp*S436-KI mice were pre-exposed to the conditioning context at day 1, and received an immediate shock (1.0 mA, 2 s) within the same context at day 2. Graph shows percentage of time spent freezing within the first 2 min when the mice were re-placed in the conditioning context at day 3 without shock $^{**}p < 0.01$ (n = 11 animals for each group).

(B–F) Six-month-old WT and *Cbp*S436A-KI mice were trained on the hidden-platform version of the Morris water maze (MWM) for 7 days. Early probe (day 8, 1 day after training) and late probe (day 19, 12 days after training) tests were performed on these mice by removing the submerged platform from the pool and leaving them to swim for a period of 60 s. (B) Acquisition of the platform location across a 7-day training session with latency to reach the platform as a measurement of learning. *Cbp*S436A-KI and WT groups had a comparable learning

(legend continued on next page)

differentiation rates (Kuipers et al., 2015). Thus, a sustained rate of neuronal differentiation may produce sufficient amounts of newborn neurons that can be functionally integrated into neural circuits to support increased memory during adulthood. In the present study, we found that the aPKC-CBP pathway is essential to maintain the stable rate of hippocampal neuronal differentiation and maturation during early adulthood development (3–6 months), suggesting its role as a homeostatic intrinsic mechanism in response to cellular changes during early adulthood to sustain functional neurogenesis, a key player in hippocampal-dependent memory formation.

In addition to phenotypic analyses, our study also provides insights into the molecular mechanisms that mediate the aPKC-CBP pathway in regulating hippocampal neurogenesis and hippocampal-dependent memory in an age-dependent manner. Previous work in liver cells shows that fully phosphorylated CBP at S436 eliminates the binding of CBP to CREB to regulate gluconeogenic gene expression (He et al., 2009), while we found that CBPS436 phosphorylation is required for CBP to bind to CREB in mature adult hippocampal extracts (6 months old) but not those of young adult mice (3 months old). The discrepancy between the hepatic and hippocampal tissues may be explained by the different CREB signals in the two tissue types. Specifically, CREB was constantly phosphorylated at S133 in hepatic tissue under the testing condition (He et al., 2009), while hippocampal tissues showed a significant reduction of pS133-CREB in mature adults (6 months old) regardless of the genotype. pS133-CREB is known to be a rate-limiting step in promoting the interaction between CREB and CBP (Parker et al., 1996). Our working model is that high levels of S133-phosphorylated CREB in young adult hippocampi play a dominant, stimulatory role in the regulation of the binding between CBP and CREB, whereas S436 phosphorylation in CBP is a compensatory regulator for the interaction between CBP and CREB in mature adult hippocampi when pS133-CREB is significantly reduced (Figure 7). This model is well supported by our data showing that aPKC activity was significantly enhanced in mature adult hippocampi where a significant reduction of pS133-CREB is evident. More interestingly, we observe that the activated form of CREB, pS133-CREB, is restrictively expressed in the hippocampal SGZ neurogenic region. Moreover, most of pS133-CREB-positive cells in the hippocampi are DCX-positive neuroblasts/newborn neurons, suggesting its role in the acquisition and maturation of DCX-positive cells. This idea has been explored in several previous studies (Herold et al., 2011; Merz et al., 2011; Nakagawa et al., 2002b). Importantly, we show here that the expression of pS133-CREB is robustly reduced in the adult hippocampi during early adulthood. We further demonstrate that elevation of CREB phosphorylation by rolipram treatment is able to rescue the hippocampal neuronal differentiation deficit and impaired pre-exposure fear memory, and restore diminished CBP binding to CREB in mature adult *Cbp*S436A-KI mice (6 months old). Together, these data suggest that the aPKC-CBP pathway is a compensatory signaling cascade that is activated in response to reduced CREB activity in mature adult hippocampi to sustain the interaction between CBP and CREB, potentially contributing to hippocampal neurogenesis and hippocampal-dependent fear memory.

Our behavioral work showed that the aPKC-CBP pathway is required for hippocampal-dependent fear memory formation in mature adult mice (6 months old) but not young adult mice (3 months old). This observation correlates well with the age-dependent functions of the aPKC-CBP pathway in maintaining hippocampal neuronal differentiation and maturation and CREB binding ability, suggesting that the aPKC-CBP/CREB signaling is key in the formation of hippocampal-dependent fear memory.

curve despite higher overall escape latency in *Cbp*S436A-KI mice (two-way ANOVA: main effect of genotypes $F(1,20) = 15.4$, $p < 0.001$; main effect of training day $F(6,120) = 10.95$, $p < 0.001$; genotype × training day interaction $F(6,120) = 0.77$, $p = 0.58$, $n = 22$). (C and D) Incidence of search strategies was analyzed using a fully automatic MWM visual algorithm. WT mice (C) were able to switch navigational search strategies from systematic to spatial search strategies by training day 4, while *Cbp*S436A-KI mice (D) exhibited a delayed transition from systematic to spatial search strategies at training day 6 (two-way ANOVA, WT: training day × strategy interaction, $F(6,66) = 12.2$, $p < 0.001$; post hoc multiple comparison, ***$p < 0.001$, **$p < 0.01$, $n = 12$; *Cbp*S436A-KI: training day × strategy interaction, $F(6,54) = 9.1$, $p < 0.001$; post hoc multiple comparison, ***$p < 0.001$, *$p < 0.05$, $n = 10$). Dashed line defines 50% incidence in the use of search strategies. (E) The percentage of time spent in four quadrant zones was analyzed at day 8 as a measurement of short-term memory (one-way ANOVA, WT: $F(3,44) = 131.2$, $p < 0.001$, target quadrant > all other quadrants, ***$p < 0.001$, $n = 12$; *Cbp*S436A-KI: $F(3,36) = 29$, $p < 0.001$, target quadrant > all other quadrants, ***$p < 0.001$, $n = 10$). (F) The percentage of time spent in four quadrant zones was analyzed at day 19 as a measurement of long-term memory (one-way ANOVA, WT: $F(3,44) = 11.78$, $p < 0.001$; target quadrant > all other quadrants, *$p < 0.05$, $n = 12$; *Cbp*S436A-KI: $F(3,36) = 8.3$, $p < 0.001$; for the target quadrant relative all other quadrants, not significant, $p > 0.05$, $n = 10$).

(G) The open field test was performed in an open box for 10 min. The cumulative time spent within the center and all four corners of the box was analyzed. Insets show representative traces of WT and *Cbp*S436A-KI mouse during the course of the open field test.

Error bars represent SEM. See also Figure S3.

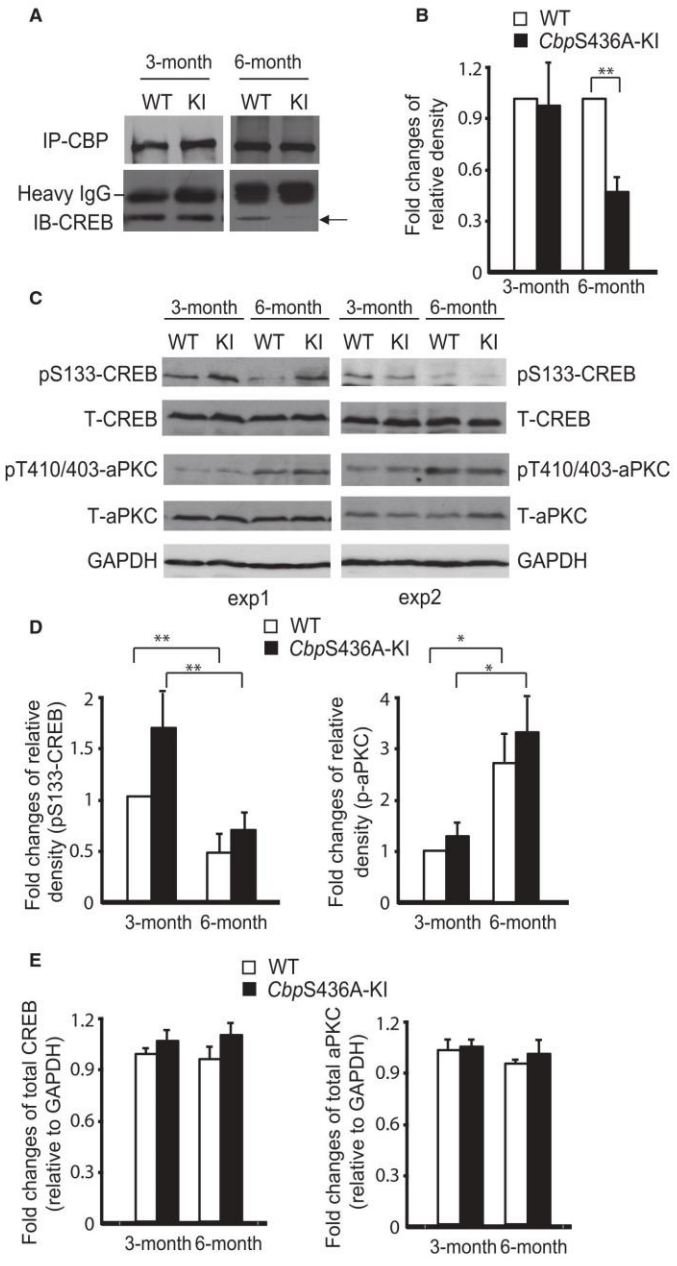

Figure 5. Mature Adult Mice Lacking CBPS436 Phosphorylation Display Impaired CBP Binding to CREB

(A) Co-immunoprecipitation analysis of the interaction between CBP and CREB in the hippocampus of WT and *Cbp*S436A-KI mice at 3 and 6 months. Hippocampal lysates were immunoprecipitated with a CBP antibody, washed, and blotted with the indicated antibody (n = 4 animals for each group). Arrow indicates CREB-expression band. IP, immunoprecipitation; IB, immunoblot; IgG, immunoglobulin G.

(B) Graph indicating the fold changes of the relative pulled-down CREB protein over the total CBP amounts, as determined by densitometry. **p < 0.01 (n = 4 animals for each group).

(C) Western blot analysis for CREB phosphorylation at S133 and aPKC zeta/iota phosphorylation at T410/403 in hippocampal tissue extracts from 3- to 6-month-old WT and *Cbp*S436A-KI mice. Blots were re-probed for total CREB or aPKC, with GAPDH as loading control.

(D) Graphs show relative levels of phosphorylation of CREB and aPKC over total CREB and aPKC, respectively, normalized to samples from 3-month-old WT. *p < 0.05, **p < 0.01 (n = 4 animals for each group).

(E) Graphs show relative levels of total CREB and aPKC over GAPDH, normalized to one of the 3-month WT samples (n = 4 animals for each group).

Error bars represent SEM.

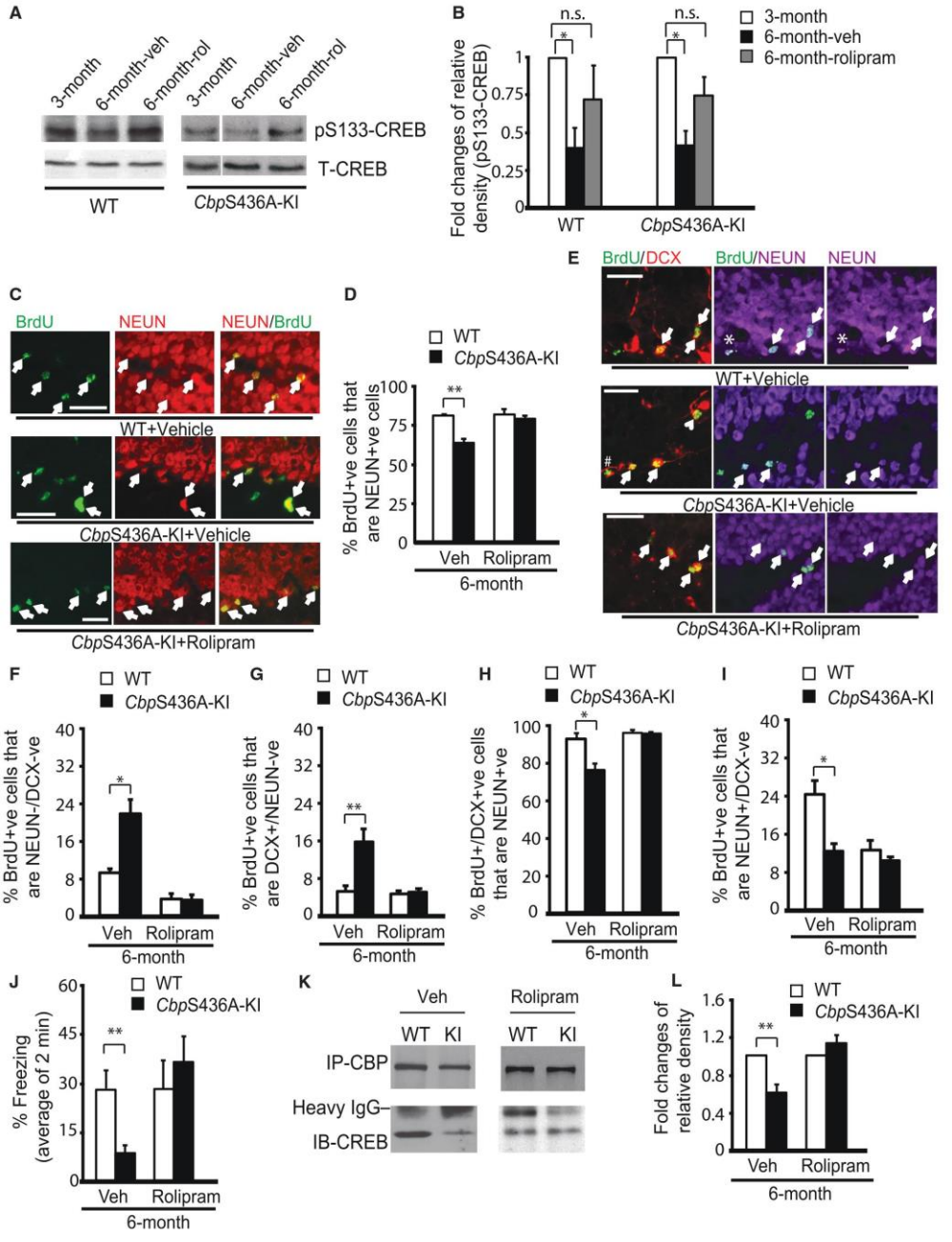

(legend on next page)

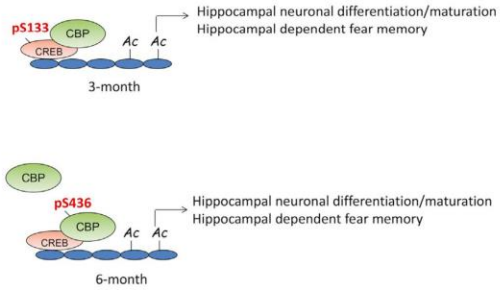

Figure 7. Working Model Depicting the Interaction between CBP and CREB

Highly phosphorylated CREB at S133 in young adult hippocampi (3 months old) plays a dominant role in the regulation of the interaction between CBP and CREB, whereas S436 phosphorylation in CBP is a compensatory regulator of CBP-CREB binding in mature adult hippocampi (6 months old) to promote hippocampal neuronal differentiation and maturation and hippocampal-dependent memory when pS133-CREB is significantly reduced.

This idea was also supported by a previous study showing that Cbp^{kix} mutant mice that lack the interaction with CREB have reduced hippocampal-dependent fear memory associated with decreased CREB-mediated gene transcription (Wood et al., 2006). In addition, our comprehensive analysis of the MWM task indicated that the aPKC-CBP pathway is required for spatial learning and long-term spatial memory in mature adult mice. The mice lacking the aPKC-CBP pathway exhibit a delayed acquisition of spatial search strategies, showing impaired spatial learning, as well as the disruption of long-term spatial memory. These results are very intriguing, as previous findings from other *Cbp* mutants generated by modifying endogenous *Cbp* gene alleles (Alarcón et al., 2004; Oike et al., 1999) show normal spatial memory measured by the MWM task. This strongly argues that CBP phosphorylation at Ser436 is a signaling cascade that specifically fine-tunes spatial memory by modulating adult hippocampal neurogenesis in an age-dependent manner.

Altogether, our findings support a concept that the aPKC-CBP pathway is a homeostatic signaling cascade that maintains functional hippocampal neurogenesis and forms hippocampal-dependent memory in response to cellular/molecular changes during early adulthood. Disruption of the homeostatic signaling may be involved in the pathogenesis of neurodegenerative disease such as Alzheimer's disease.

EXPERIMENTAL PROCEDURES

Animals and Drug Treatment

All animal use was approved by the Animal Care Committees of the Hospital for Sick Children and the University of Ottawa in accordance with the Canadian Council of Animal Care policies. *Cbp*S436A mice (Zhou et al., 2004) were maintained on a 12-hr light/12-hr dark cycle with ad libitum access to food and water. Detailed information regarding animals and drug treatment is provided in Supplemental Experimental Procedures.

Figure 6. Rolipram, a PDE4 Inhibitor, Rescues Neuronal Differentiation Deficit and Impaired Fear Memory, and Restores the Association between CBP and CREB in Mature Adult *Cbp*S436A-KI Mice

Six-month-old mice received rolipram intraperitoneally or vehicle (veh) for 14 days, and were euthanized for western blot and immunostaining analyses.

(A) Western blot analysis for CREB phosphorylation at S133 in hippocampal extracts from 3-to 6-month-old WT and *Cbp*S436A-KI mice. Blots were reprobed for total CREB as loading controls.

(B) Graph shows the relative level of phosphorylation of CREB over total CREB. *$p < 0.05$ ($n = 3$ animals for each group). n.s., not significant.

(C and E) Fluorescence images of hippocampal sections from 6-month-old WT and *Cbp*S436A-KI mice in the presence of rolipram or vehicle, (C) stained for BrdU (green) and NEUN (red), arrows denote BrdU/NEUN-positive neurons; (E) stained for BrdU (green), DCX (red), and NEUN (purple), arrows denote triple-labeled $BrdU^+/DCX^+/NEUN^+$ cells, arrowhead denotes $BrdU^+/DCX^+/NEUN^-$ cells, asterisks denote $BrdU^+/DCX^-/NEUN^+$ cells, and hash denotes $BrdU^+/DCX^-/NEUN^-$ cells. Scale bars, 25 μm (C) and 20 μm (E).

(D and F–I) Quantitative analysis of the percentage of BrdU-positive cells that express NEUN (D), the percentage of BrdU-positive cells that were negative for both NEUN and DCX (F), the percentage of BrdU-positive cells that express DCX but not NEUN (G), the percentage of BrdU-positive, DCX-positive cells that also express NEUN (H), and the percentage of BrdU-positive cells that were positive for NEUN but negative for DCX (I) in the hippocampi from WT and *Cbp*S436A-KI mice. *$p < 0.05$, **$p < 0.01$ ($n = 4$ animals for each group).

(J) Percentage of time spent freezing in the context that was pre-exposed to the mice 2 days prior, and together with an immediate shock 1 day before, following 3-week rolipram (or vehicle) treatment in 6-month-old WT and *Cbp*S436-KI mice. **$p < 0.01$ ($n = 11$ animals for each group).

(K and L) Co-immunoprecipitation analysis of the interaction between CBP and CREB in the hippocampus of 6-month-old WT and *Cbp*S436A-KI mice upon rolipram or vehicle treatment. IP, immunoprecipitation; IB, immunoblot; IgG, immunoglobulin G. The graph (L) indicates the fold changes of the relative pulled-down CREB protein over the total CBP amounts. **$p < 0.01$ ($n = 3$ animals for each group) Veh, vehicle.

Error bars represent SEM. See also Figure S4.

BrdU Labeling

In one set of experiments, mice were injected intraperitoneally with 100 mg/kg BrdU (Sigma-Aldrich) once and then euthanized 24 hr later. In a second set of experiments, mice were injected intraperitoneally with 100 mg/kg BrdU once daily for 3 days. These mice were euthanized 12 days after the first BrdU injection. In a third set of experiments, mice were injected intraperitoneally with 60 mg/kg BrdU four times at 3-hr intervals (Morshead et al., 1998), and euthanized 30 days later. Detailed information on tissue processing is provided in Supplemental Experimental Procedures.

Immunohistochemistry, Microscopy, and Quantification

Detailed information is provided in Supplemental Experimental Procedures.

Co-immunoprecipitation, Western Blot Analysis, and Densitometry

Hippocampal tissues were homogenized and lysed in lysis buffer, as detailed in Supplemental Experimental Procedures.

Context Pre-exposure Fear Conditioning, Morris Water Maze Task, and Open Field Test

For context pre-exposure fear conditioning, mice were trained as described previously (Frankland et al., 2004), as detailed in Supplemental Experimental Procedures. The MWM task and open field test were performed by the Behavioral Core Facility at the University of Ottawa. Detailed information is provided in Supplemental Experimental Procedures.

Antibodies

Detailed information is provided in Supplemental Experimental Procedures.

Statistics

Statistical analyses were performed with a two-tailed Student's t test or ANOVA with Sidak's multiple comparison post hoc analysis, unless otherwise indicated. Error bars indicate the SEM.

SUPPLEMENTAL INFORMATION

Supplemental Information includes Supplemental Experimental Procedures and four figures and can be found with this article online at http://dx.doi.org/10.1016/j.stemcr.2016.08.007.

AUTHOR CONTRIBUTIONS

A.G. and K.H. equally performed experiments, analyzed data, and contributed to paper writing; Y.N. performed fear memory experiments; Y.N. and P.F. contributed to fear memory experimental design, data analysis, and interpretation; M.S. and G.I.C. performed experiments; S.B. contributed to search strategies analysis; D.L. contributed to MWM experimental design, data analysis, and interpretation; L.H. and F.W. generated *Cbp*S436A knockin mouse strain; J.W. designed and performed experiments, analyzed and interpreted data, and wrote the paper.

ACKNOWLEDGMENTS

We are indebted to Dr. Freda Miller who provided very strong support for the work presented herein. This work was supported by the J.P. Bickell Foundation, Ottawa Hospital Foundation, and NSERC Discovery Grant (RGPIN-2016-05656) to J.W., and CIHR (FDN143227) to P.F. P.F. is a Canada Research Chair. We thank Dennis Aquino for mouse colony assistance, and Mirela Hasu and Christine Luckhart of the behavioral core for technical assistance.

Received: July 27, 2015
Revised: August 10, 2016
Accepted: August 11, 2016
Published: September 8, 2016

REFERENCES

Alarcón, J.M., Malleret, G., Touzani, K., Vronskaya, S., Ishii, S., Kandel, E.R., and Barco, A. (2004). Chromatin acetylation, memory, and LTP are impaired in CBP+/- mice: a model for the cognitive deficit in Rubinstein-Taybi syndrome and its amelioration. Neuron *42*, 947–959.

Cancino, G.I., Yiu, A.P., Fatt, M.P., Dugani, C.B., Flores, E.R., Frankland, P.W., Josselyn, S.A., Miller, F.D., and Kaplan, D.R. (2013). p63 regulates adult neural precursor and newly born neuron survival to control hippocampal-dependent behavior. J. Neurosci. *42*, 12569–12585.

Deng, W., Aimone, J.B., and Gage, F.H. (2010). New neurons and new memories: how does adult hippocampal neurogenesis affect learning and memory? Nat. Rev. Neurosci. *11*, 339–350.

Dupret, D., Fabre, A., Döbrössy, M.D., Panatier, A., Rodríguez, J.J., Lamarque, S., Lemaire, V., Oliet, S.H., Piazza, P.V., and Abrous, D.N. (2007). Spatial learning depends on both the addition and removal of new hippocampal neurons. PLoS Biol. *5*, e214.

Fanselow, M.S. (2000). Contextual fear, gestalt memories, and the hippocampus Behav. Brain Res. *10*, 73–81.

Fatt, M., Hsu, K., He, L., Wondisford, F., Miller, F.D., Kaplan, D.R., and Wang, J. (2015). Metformin acts on two different molecular pathways to enhance adult neural precursor proliferation/self-renewal and differentiation. Stem Cell Rep. *5*, 1–8.

Frankland, P.W., Josselyn, S.A., Anagnostaras, S.G., Kogan, J.H., Takahashi, E., and Silva, A.J. (2004). Consolidation of CS and US representations in associative fear conditioning. Hippocampus *14*, 557–569.

Granger, M.W., Franko, B., Taylor, M.W., Messier, C., St George-Hyslop, P., and Bennett, S.A. (2016). A TgCRND8 mouse model of Alzheimer's disease exhibits sexual dimorphisms in behavioral indices of cognitive reserve. J. Alzheimers Dis. *51*, 757–773.

He, L., Sabet, A., Djedjos, S., Miller, R., Sun, X., Hussain, M.A., Radovick, S., and Wondisford, F.E. (2009). Metformin and insulin suppress hepatic gluconeogenesis through phosphorylation of CREB binding protein. Cell *137*, 635–646.

Herold, S., Jagasia, R., Merz, K., Wassmer, K., and Lie, D.C. (2011). CREB signalling regulates early survival, neuronal gene expression and morphological development in adult subventricular zone neurogenesis. Mol. Cell. Neurosci. *46*, 79–88.

Imayoshi, I., Sakamoto, M., Ohtsuka, T., Takao, K., Miyakawa, T., Yamaguchi, M., Mori, K., Ikeda, T., Itohara, S., and Kageyama, R. (2008). Roles of continuous neurogenesis in the structural and functional integrity of the adult forebrain. Nat. Neurosci. *11*, 1153–1161.

Kee, N., Teixeira, C.M., Wang, A.H., and Frankland, P.W. (2007). Preferential incorporation of adult-generated granule cells into spatial memory networks in the dentate gyrus. Nat. Neurosci. *10*, 355–362.

Kuipers, S.D., Schroeder, J.E., and Trentani, A. (2015). Changes in hippocampal neurogenesis throughout early development. Neurobiol. Aging *36*, 365e379.

Lopez-Atalaya, J.P., Ciccarelli, A., Viosca, J., Valor, L.M., Jimenez-Minchan, M., Canals, S., Giustetto, M., and Barco, A. (2011). CBP is required for environmental enrichment-induced neurogenesis and cognitive enhancement. EMBO. J. *30*, 4287–4298.

Matus-Amat, P., Higgins, E.A., Barrientos, R.M., and Rudy, J.W. (2004). The role of the dorsal hippocampus in the acquisition and retrieval of context memory representations. J. Neurosci. *24*, 2431–2439.

Merz, K., Herold, S., and Lie, D.C. (2011). CREB in adult neurogenesis—master and partner in the development of adult-born neurons? Eur. J. Neurosci. *33*, 1078–1086.

Mizuno, M., Yamada, K., Maekawa, N., Saito, K., Seishima, M., and Nabeshima, T. (2002). CREB phosphorylation as a molecular marker of memory processing in the hippocampus for spatial learning. Behav. Brain Res. *133*, 135–141.

Morshead, C.M., Craig, C.G., and van der Kooy, D. (1998). In vivo clonal analyses reveal the properties of endogenous neural stem cell proliferation in the adult mammalian forebrain. Development *125*, 2251–2261.

Mu, Y., and Gage, F.H. (2011). Adult hippocampal neurogenesis and its role in Alzheimer's disease. Mol. Neurodegener. *6*, 85.

Ming, G.L., and Song, H. (2011). Adult neurogenesis in the mammalian brain: significant answers and significant questions. Neuron *70*, 687–702.

Nakagawa, S., Kim, J.E., Lee, R., Malberg, J.E., Chen, J., Steffen, C., Zhang, Y.J., Nestler, E.J., and Duman, R.S. (2002a). Regulation of neurogenesis in adult mouse hippocampus by cAMP and the cAMP response element-binding protein. J. Neurosci. *22*, 3673–3682.

Nakagawa, S., Kim, J.E., Lee, R., Chen, J., Fujioka, T., Malberg, J., Tsuji, S., and Duman, R.S. (2002b). Localization of phosphorylated cAMP response element-binding protein in immature neurons of adult Hippocampus. J. Neurosci. *22*, 9868–9876.

Oike, Y., Hata, A., Mamiya, T., Kaname, T., Noda, Y., Suzuki, M., Yasue, H., Nabeshima, T., Araki, K., and Yamamura, K. (1999). Truncated CBP protein leads to classical Rubinstein-Taybi syndrome phenotypes in mice: implications for a dominant-negative mechanism. Hum. Mol. Genet. *8*, 387–396.

Palmer, T.D., Takahashi, J., and Gage, F.H. (1997). The adult rat hippocampus contains primordial neural stem cells. Mol. Cell. Neurosci. *8*, 389–404.

Parker, D., Ferreri, K., Nakajima, T., LaMorte, V.J., Evans, R., Koerber, S.C., Hoeger, C., and Montminy, M.R. (1996). Phosphorylation of CREB at Ser-133 induces complex formation with CREB-binding protein via a direct mechanism. Mol. Cell. Biol. *16*, 694–703.

Rudy, J.W., Huff, N.C., and Matus-Amat, P. (2004). Understanding contextual fear conditioning: insights from a two-process model. Neurosci. Biobehav. Rev. *28*, 675–685.

Sahay, A., Scobie, K.N., Hill, A.S., O'Carroll, C.M., Kheirbek, M.A., Burghardt, N.S., Fenton, A.A., Dranovsky, A., and Hen, R. (2011). Increasing adult hippocampal neurogenesis is sufficient to improve pattern separation. Nature *472*, 466–470.

Saxe, M.D., Battaglia, F., Wang, J.W., Malleret, G., David, D.J., Monckton, J.E., Garcia, A.D., Sofroniew, M.V., Kandel, E.R., Santarelli, L., et al. (2006). Ablation of hippocampal neurogenesis impairs contextual fear conditioning and synaptic plasticity in the dentate gyrus. Proc. Natl. Acad. Sci. USA *103*, 17501–17506.

Silva, A.J., Kogan, J.H., Frankland, P.W., and Kida, S. (1998). Creb and memory. Annu. Rev. Neurosci. *21*, 127–148.

Shih, H.M., Goldman, P.S., BeMaggio, A.J., Holleggerg, S.M., Goodman, R.H., and Hoekstra, M.F. (1996). A positive genetic selection for disrupting protein-protein interactions: identification of CREB mutations that prevent association with the coactivator CBP. Proc. Natl. Acad. Sci. USA *93*, 13896–13901.

Toni, N., Laplagne, D.A., Zhao, C., Lombardi, G., Ribak, C.E., Gage, F.H., and Schinder, A.F. (2008). Neurons born in the adult dentate gyrus form functional synapses with target cells. Nat. Neurosci. *11*, 901–907.

Tsui, D., Voronova, A., Gallagher, D., Kaplan, D.R., Miller, F.D., and Wang, J. (2014). CBP regulates the differentiation of interneurons from ventral forebrain neural precursors during murine development. Dev. Biol. *385*, 230–241.

Wang, J., Weaver, I.C.G., Gauthier-Fisher, A.S., Wang, H., He, L., Yeomans, J., Wondisford, F., Kaplan, D.R., and Miller, F.D. (2010). CBP histone acetyltransferase activity regulates embryonic neural differentiation in the normal and Rubinstein-Taybi syndrome brain. Dev. Cell *18*, 114–125.

Wang, J., Gallagher, D., DeVito, L., Cancino, I., Tsui, D., He, L., Keller, G.M., Frankland, P.W., Kaplan, D.R., and Miller, F.D. (2012). Metformin activates atypical PKC-CBP pathway to promote neurogenesis and enhance spatial memory formation. Cell Stem Cell *11*, 23–35.

Winner, B., Kohl, Z., and Gage, F.H. (2011). Neurodegenerative disease and adult neurogenesis. Eur. J. Neurosci. *33*, 1139–1151.

Wood, M.A., Attner, M.A., Oliveira, A.M.M., Brindle, P.K., and Abel, T.A. (2006). A transcription factor-binding domain of the coactivator CBP is essential for long-term memory and the expression of specific target genes. Learn. Mem. *13*, 609–617.

Zhou, X.Y., Shibusawa, N., Naik, K., Porras, D., Temple, K., Ou, H., Kaihara, K., Roe, M.W., Brady, M.J., and Wondisford, F.E. (2004). Insulin regulation of hepatic gluconeogenesis through phosphorylation of CREB-binding protein. Nat. Med. *10*, 633–637.

Zhao, C., Deng, W., and Gage, F.H. (2008). Mechanisms and functional implications of adult neurogenesis. Cell *132*, 645–660.

Stem Cell Reports, Volume 7

Supplemental Information

The aPKC-CBP Pathway Regulates Adult Hippocampal Neurogenesis in an Age-Dependent Manner

Ayden Gouveia, Karolynn Hsu, Yosuke Niibori, Matthew Seegobin, Gonzalo I. Cancino, Ling He, Fredric E. Wondisford, Steffany Bennett, Diane Lagace, Paul W. Frankland, and Jing Wang

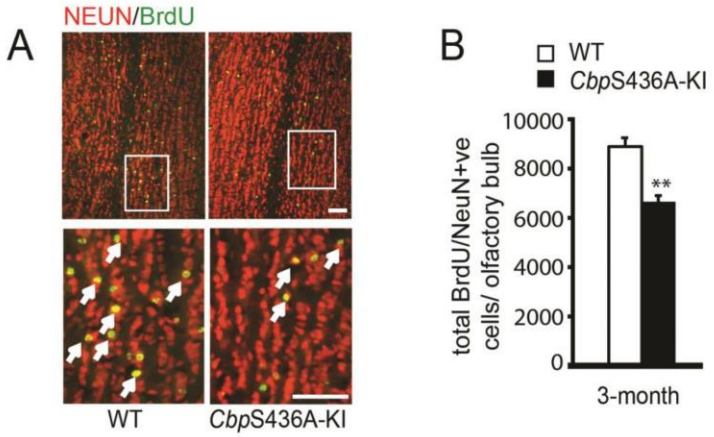

Figure S1. Young adult mice (3 months) lacking CBPS436 phosphorylation show a reduction in adult olfactory bulb neurogenesis, related to Figure 1. (A) Fluorescence photomicrographs of coronal olfactory bulb (OB) sections from 3-month old WT and *Cbp*S436A-KI mice 30 days after BrdU injection. Sections were stained for BrdU (green) and NEUN (red). Scale bar =20 μm. (B) Quantitative analysis of the total number of BrdU-positive, NEUN-positive newborn neurons, determined from sections as shown in (A), in OB from WT and *Cbp*S436A-KI mice (3-month old). **$p < 0.01$ ($n = 3$ for each group).

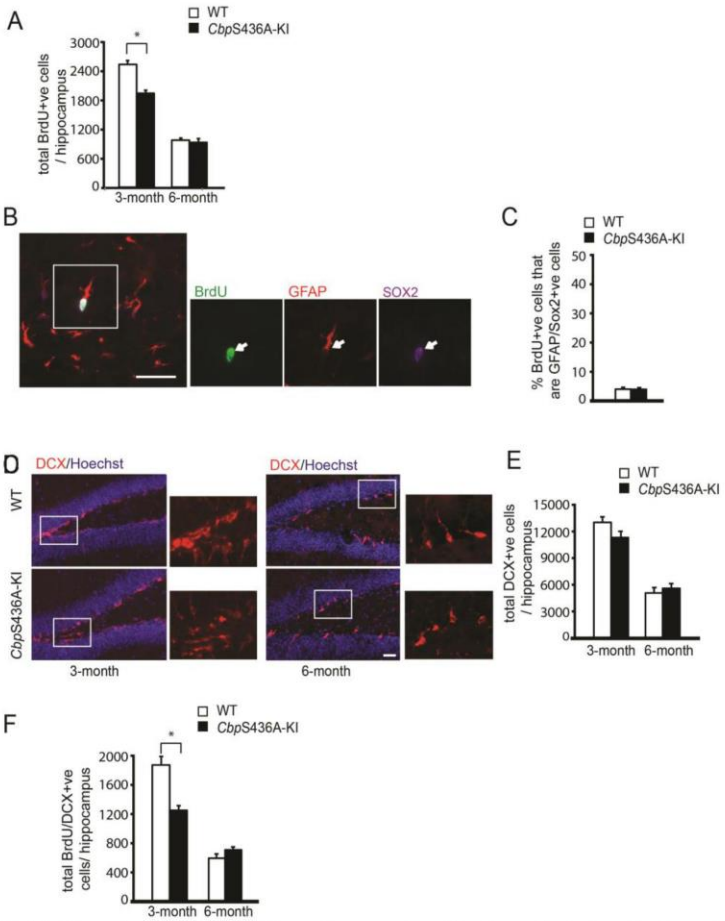

Figure S2. Total number of BrdU positive cells was reduced in 3 months but not in 6 months *Cbp*S436A-KI mice 12 days after BrdU injections, related to Figure 2A. (A)Quantitative analysis of the total number of BrdU-positive cells in the hippocampi from WT and *Cbp*S436A-KI mice at the age of 3 and 6 months. (n =5-7 animals for each group). **The proportion of BrdU labelled GFAP/Sox2 positive type I radial glial cells was not changed in mature adult *Cbp*S436A-KI mice, related to Figure 2E-F. (**B**)** photomicrographs of coronal hippocampal sections from 6-month-old *Cbp*S436A KI mice, sacrificed 12 days after the first BrdU injections. Sections were stained for BrdU (green), GFAP (red) and SOX2 (purple). Scale bar =25μm. (C) Quantitative analysis of the percentage of BrdU-positive cells that are also positive for GFAP and Sox2 in the hippocampi from WT and *Cbp*S436A-KI mice at the age of 6 months. (n =3-4 animals for each group). **Total number of DCX positive cells was not changed in *Cbp*S436A-KI mice, while the number of BrdU-colabeled DCX positive cells was significantly reduced at 3 months *Cbp*S436A-KI mice, related to Figure 2G-H.** (D) Fluorescence photomicrographs of coronal hippocampal dentate gyrus sections from 3 months and 6 months WT (upper panels) and *Cbp*S436A-KI (lower panels) mice. Sections were stained for doublecortin (DCX) (red) and counter-stained for Hoechst 33342 (blue). Boxed areas were shown at higher magnification on the right. Scale bar=25μm. (E) Quantitative analysis of the total number of DCX-positive cells in the hippocampi from WT and *Cbp*S436A-KI mice at the age of 3 months and 6 months. (n = 4 animals for each group). (F) Quantitative analysis of the total number of BrdU positive, DCX-positive cells in the hippocampi from both 3 and 6 months WT and *Cbp*S436A-KI mice 12 days following BrdU injections (n = 5-7 animals for each group).

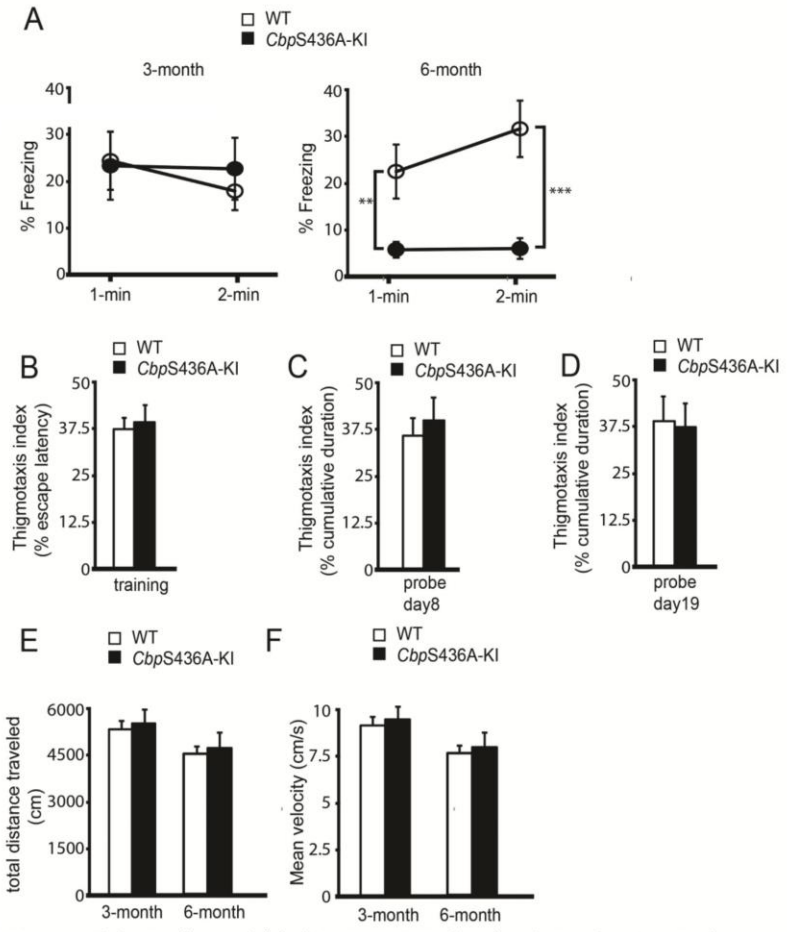

Figure S3. Mature adult mice (6 months) lacking CBP S436 phosphorylation show impaired pre-exposure contexture fear memory, related to Figure 4A.(A) Percentage of the time spent freezing in the context within each min for 3 and 6 months WT and *Cbp*S436A-KI mice. ** $p<0.01$; *** $p<0.001$. **Mature adult mice (6 months) lacking CBP S436 phosphorylation show the same thigmotaxis as their wild type littermates, related to Figure4B-F.** (B-D) Percentage of thigmotaxis were assessed for WT and *Cbp*S436A-KI mice during training (B), early (day8, C) and late probe (day 19, D) tests. **Mature adult mice (6 months) lacking CBP S436 phosphorylation show normal general motor activities, related to Figure4G.** (E) Analysis of the total distance travelled during the open field test for WT and *Cbp*S436A-KI mice at the age of 3 and 6 months. (F) Analysis of the mean velocity during the 10-minutes of movement for WT and *Cbp*S436A-KI mice at the age of 3 and 6 months.

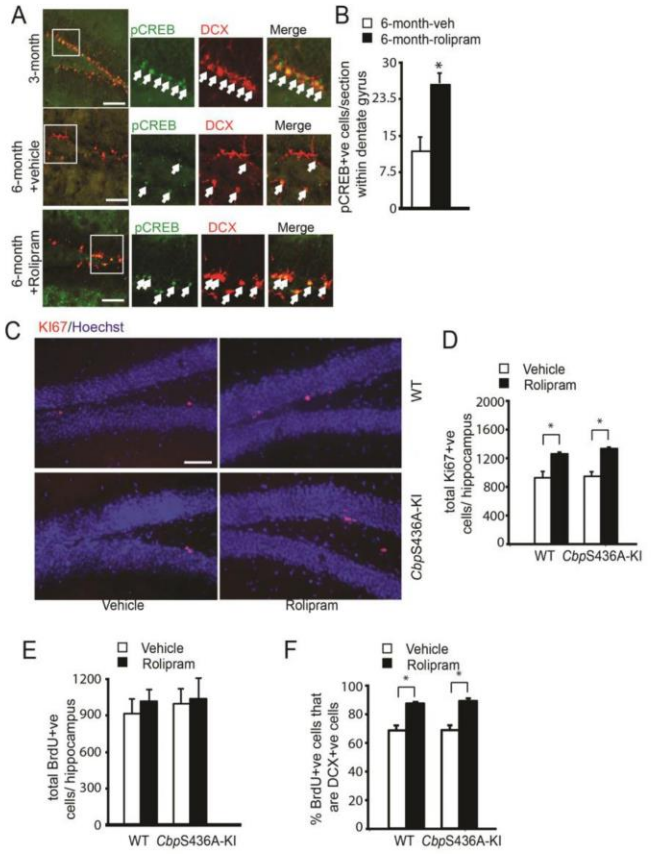

Figure S4. Rolipram treatment significantly increased the number of pS133-CREB positive cells in the 6-month-old hippocampal SGZ, related to Figure 6A-B. (A) Fluorescence photomicrographs of coronal hippocampal dentate gyrus sections from 3- and 6-month-old WT mice in the presence of rolipram or vehicle. Sections were stained for p-CREB (green), DCX (red). Arrows denote double labelled pS133-CREB/DCX positive cells Scale bar = 50 μm. (B) Quantitative analysis of the number of pS133-CREB positive cells in the 6-month-old hippocampal SGZ in the presence of rolipram or vehicle regardless of genotypes, determined from sections as shown in (A). *$p < 0.05$; veh: vehicle, n =4 animals for each group. **Rolipram treatment significantly increased total number of KI67 positive proliferating cells in both WT and *Cbp*S436A-KI mice, related to Figure 6C-I** (C) Fluorescence photomicrographs of coronal hippocampal dentate gyrus sections from 6 months WT (upper panels) and *Cbp*S436A-KI (lower panels) mice in the absence (left panels) and presence of rolipram (right panels). Sections were stained for KI67 (red) and counter-stained for Hoechst 33342 (blue). Scale bar=50μm. (D) Quantitative analysis of the total number of Ki67-positive cells in the hippocampi from WT and *Cbp*S436A-KI mice at the age of 6 months in the absence and presence of rolipram. (n = 4 animals for each group). **Rolipram treatment significantly increased the proportion of BrdU labelled DCX positive cells in both WT and *Cbp*S436A-KI mice, related to Figure 6E.(E)**Quantitative analysis of the total number of BrdU-positive cells in the hippocampi from WT and *Cbp*S436A-KI mice at the age of 6 months in the absence and presence of rolipram. (n = 4 animals for each group). (F) Quantitative analysis of the proportion of BrdU-positive cells that are positive for DCX in the hippocampi from WT and *Cbp*S436A-KI mice at the age of 6 months in the absence and presence of rolipram. (n = 4 animals for each group).

Supplemental Experimental Procedures:

Animals and drug treatment

Only wild type (WT) and homozygous (*Cbp*S436A-KI) mice were used as experimental mice and heterozygous of *Cbp*S436A were used for breeding. For rolipram treatment, mice were given saline containing 2% DMSO as a control (vehicle) or rolipram (1.25 mg/kg, i.p; Sigma, St. Louis, MO) in saline containing 2% DMSO daily for 14 or 21 days.

BrdU labeling

Following the three sets of BrdU-chasing experiments, the mice were sacrificed by a lethal dose of pentobarbital and perfused transcardially with PBS and 4% paraformaldehyde. Brains were postfixed, cryoprotected and cryosectioned at 20 μm and 14 μm for hippocampus and olfactory bulb, respectively. Every tenth hippocampal section was analyzed immunohistochemically for BrdU, NEUN, DCX, SOX2, GFAP and TBR2 as previously described (Wojtowicz et al., 2006).

Immunohistochemistry, microscopy, and quantification

Immunostaining of brain sections was performed as previously described (Wang et al., 2012). Sections were post-fixed with 4% PFA, blocked and permeabilized with 5% BSA and 0.3% Triton-X, and then sections were incubated with primary antibodies at 4ºC overnight, with secondary antibodies at room temperature for 1 hour, counterstained with Hoechst 33343 (1:2000, Sigma-Aldrich) and mounted using GelTol (Fisher). For BrdU colabelling with DCX, sections were first immunostained with anti-DCX followed by an Alexa Fluor 555-conjugated donkey anti-goat secondary antibody. Following that, the same sections were incubated in 2 N HCl at 45°C for 30 min, rinsed in PBS, incubated in rat anti-BrdU antibody at 4°C overnight,

and finally treated with Alexa 488 donkey anti-rat antibody for 1 hour. For BrdU colabelling with NEUN, TBR2, GFAP or SOX2, sections were incubated in 1 N HCl at 60°C for 30 min, rinsed in PBS, incubated in rat anti-BrdU antibody at 4°C overnight, in Alexa 488 donkey anti-rat antibody for 1 hour and then sequentially immunostained with anti-NEUN, anti-TBR2, anti-GFAP or anti-SOX2 followed by Alexa Fluor -conjugated secondary antibodies.

Digital image acquisition was performed using either a Zeiss Axioplan 2 fluorescent microscopy with Zeiss Axiovision software that contains z-axis capability, or a Zeiss LSM 510 confocal microscopy using Zeiss Zen Pro software V2.0 (Oberkochen, Germany). 10-15 images were captured in the Z-axis per section at a maximum of 1um apart and processed as an optical stack of 10-15 scanned slices for quantification.

For quantification, positive cells were quantified using a modified stereological method that have been extensively used (Eisch et al., 2000, Gould et al., 1999, Malberg et al., 2000, Olariu et al, 2007, Wang, et al, 2012, West et al., 1991). We exhaustively quantified every positive cell within dentate gyrus region including SGZ, GCL and hilus. Thus we used an area sampling fraction of 1 as is commonly utilized for counting rare populations of cells (Jayatissa et al., 2009, Mouton et al., 2002) since the raw counts for the numbers of positive cells were low according to disector/fractionator standards (Guillery, et al., 1997; Pakkenberg, et al., 1988; West, et al., 1990) and the cells are not evenly distributed within the dentate gyrus. Given recent work suggesting the absence of lost caps in perfusion fixed tissue and potential bias that can occur with traditional use of guard zones (Carlo, et al., 2011; Gardella, et al., 2003; Miller, et al., 2014), we did not employ a guard zone and used the same method to quantify both wild type and knock-in mice brain sections. We sampled 1 in every 10 sections throughout the septotemporal axis of the hippocampal structure (-1.3 mm to -3.70 mm relative to bregma referring to the

rostral-caudal coordinates) by an examiner that was blind to group assignments. Since the section sampling fraction was 1/10, the resulting raw count for each region was multiplied by 10 to obtain an estimate of the total number of cells per dentate gyrus.

Co-immunoprecipitation

Hippocampal tissues were homogenised and lysed in lysis buffer (25mM Tris, pH=7.4, 10mM NaCl, 2mM EDTA, 1mM EGTA, 0.5% Triton-100, 10% glycerol) containing 1mM PMSF, 1mM sodium orthovanadate, 20mM sodium fluoride, 10 μg/ml aprotinin and 10 μg/ml leupeptin. The extractions were sonicated 3 times with 5 seconds pulses at 1 minute intervals. Then, 1 mg protein lysate from each sample was incubated with 50 ul protein A conjugated magnetic beads and 3 ug anti-CBP antibody or normal rabbit IgG antibody at 4ºC overnight. Following that, the magnetic beads were rinsed 3 times with lysis buffer, boiled with sample buffer, and loaded on a 5-15% gradient SDS-PAGE gel.

Western blot analysis and densitometry

Hippocampal tissues were lysed in lysis buffer (25 mM Tris, pH=7.4, 10mM NaCl, 2mM EDTA, 1mM EGTA 0.5% Triton-100, 10% glycerol) containing 1 mM PMSF, 1 mM sodium orthovanadate, 20 mM sodium fluoride, 10 μg/ml aprotinin and 10 μg/ml leupeptin. 100 μg protein lysates were resolved on a 10% SDS-PAGE gel, and western blots performed as previously described (Wang et al, 2012). Densitometry was performed using Image J.

Context pre-exposure fear conditioning

Mice were individually placed in the conditioning chamber for 10 min. No shocks were delivered in this phase of the experiment. Twenty-four hours later, all mice were placed in the conditioning context and, 5 s later, received a footshock (2 s, 1.0 mA). Twenty-four hours after immediate shock training, mice were placed in the conditioning context and freezing was assessed for a 2-min period. During this period, no shock was presented. For rolipram experiment, male mice received either vehicle (saline containing 2% DMSO, i.p. daily) or rolipram (1.25 mg/kg, i.p; in saline containing 2% DMSO, daily) treatment for 21 days followed by the 3-day paradigm of context pre-exposure fear memory test.

Morris Water Maze Task

6 months old mice (WT and *Cbp*S436A-KI, n=10-12/group) were trained on the hidden platform version of the water maze using a circular pool (122 cm diameter,83.5 cm depth, 22ºC) filled with 74.2 cm of water and made opaque with nontoxic white paint. The escape platform (10 cm diameter) was submerged 0.5 cm below the water surface. All testing was conducted under with 120lux lighting and an extra maze visual cue with "X" printed in black ink (2.9 cm thickness) on a white paper (13.5x15cm) was located on one wall. Acquisition was measured as latency to reach the platform and four possible start locations were pseudorandomly assigned to each trial. Each animal was given three 60 s trials to find the platform with a 15 s inter-trial interval across 7 days. A probe trial was then completed at day 8 and days 19 after the 7-day training, leaving the mice swim in the pool for 60 sec when the platform was removed. Ethovision tracking software was used to record behavior of the mice during testing and a full-automatic algorithm software developed by Steffany Bennett laboratory (Granger, et al., 2016) was used to determine search strategies during the training sessions.

Open field test

Mice were individually placed in a 45cm x 45cm x 45cm open field chamber for 10 min, and Ethovision software was used to record and analyze the distance traveled, locomotion speed, and amount of time the mice spent in respective zones (outer, middle, and center) of the box.

Antibodies

For immunohistochemistry, the primary antibodies used were rabbit anti-cleaved caspase 3 (1:1000; Cat#9661, Cell Signaling Technology, Beverly, MA), mouse anti-KI67 (1:200; Cat#556003, BD Pharmingen, Heidelberg, Germany), goat anti-doublecortin (1:200; Cat#sc-8066, Santa-Cruz Biotechnology), rat anti-BrdU (1:200; Cat#OBT0030G, Accurate Chemical), mouse anti-NEUN (1:500; Cat#MAB377, Chemicon), mouse anti-SOX2 (1:200; Cat#4900, Cell Signaling Technologies) rabbit anti-TBR2 (1:300; Cat#ab23345, Abcam), rabbit anti-GFAP (1:1000; Cat#ab7260, Abcam) and rabbit anti-p-CREB (S133)(1:100; Cat#9198, Cell Signaling). The secondary antibodies used were Alexa Fluor 555-conjugated goat anti-mouse IgG (1:1000; Cat#A21422, Molecular Probes), Alexa Fluor 488-conjugated goat anti-rat IgG (1:1000; Cat#A21208, Molecular Probe), Alexa Fluor 488-conjugated goat anti-rabbit IgG (1:1000; Cat#4412, Cell Signaling), Alexa Fluor 555-conjugated donkey anti-goat IgG (1:1000; Cat#A21432, Molecular Probes), Alexa Fluor 647-conjugated goat anti-mouse IgG (1:1000; Cat#A21237, Molecular Probes). For western blots, the primary antibodies were rabbit anti-p-aPKCζ/ι (T410/403)(1:500, Cat#9378, Cell Signaling), mouse anti- aPKCζ/ι (1:500; Cat#610175, BD), rabbit anti-p-CREB (S133)(1:500; Cat#9198, Cell Signaling), mouse anti-CREB (1:500; Cat#9104, Cell Signaling), rabbit anti-CBP (1:100; Cat#sc-583, Santa-Cruz).

Secondary antibodies for western blots were HRP-conjugated goat anti-mouse or anti-rabbit (1:4000; Cat#7076 and #7074, Boehringer Mannheim).

References

Carlo, C. N., and Stevens, C. F. (2011). Analysis of differential shrinkage in frozen brain sections and its implications for the use of guard zones in stereology. J. Comp. Neurol. 519: 2803–2810.

Eisch A.J., Barrot M., Schad, C.A., Self, D.W. and Nestler E.J. (2000) Opiates inhibit neurogenesis in the adult rat hippocampus. Proc Natl Acad Sci U. S. A. *97*, 7579-7584.

Gardella, D., Hatton, W. J., Rind, H. B., Rosen, G. D., and von Bartheld, C. S. (2003). Differential tissue shrinkage and compression in the z-axis: implications for optical dissector counting in vibratome-, plastic- and cryosections. J. Neurosci. Methods 124: 45–59.

Gould, E., Beylin, A., Tanapat, P., Reeves, A., Shors, T.J. (1999) Learning enhances adult neurogenesis in the hippocampal formation. Nat. Neuroscience *2*, 260-265.

Granger, M.W., Franko, B., Taylor, M.W. Messier, C., St George-Hyslop, P. and Bennett, S.A. (2016) A TgCRND8 Mouse Model of Alzheimer's Disease Exhibits Sexual Dimorphisms in Behavioral Indices of Cognitive Reserve, J.Alzheimers Dis. Feb 10 [Epub ahead of print].

Guillery, R.W. and Herrup, K. (1997) Quantification without pontification: choosing a method for counting objects in sectioned tissues. J Comp Neurol *386*, 2-7.

Jayatissa, M.N., Henningsen, K., West, M.J. and Wiborg, O. (2009) Decreased cell proliferation in the dentate gyrus does not associate with development of anhedonic-like symptoms in rats. Brain Res *1290*, 133-141.

Malberg, J.E., Eisch, A.J., Nestler, E.J. and Duman, R.S. (2000) Chronic antidepressant treatment increases neurogenesis in adult rat hippocampus. J Neurosci. 20, 9104-9110.

Mouton, P. (2002) Principles and Practices of Unbiased Stereology: An Introduction for Bioscientists (The Johns Hopkins University Press, Baltimore).

Miller, D.J., Balaram, P., Young, N.A. and Kaas, J.H. (2014) Three counting methods agree on cell and neuron number in chimpanzee primary visual cortex. Front. Neuroanat. 8:36.

Olariu, A., Cleaver, K.M. and Cameron, H.A. (2007) Decreased neurogenesis in aged rats results from loss of granule cell precursors without lengthening of the cell cycle. J Comp Neurol *501*, 659-667.

Pakkenberg, B. and Gundersen, H.J. (1988) Total number of neurons and glial cells in human brain nuclei estimated by the disector and the fractionator. J Microsc *150*, 1-20.

Wang, J., Gallagher, D., DeVito, L., Cancino, I., Tsui, D., He, L., Keller, G.M., Frankland, P.W., Kaplan, D.R. and Miller, F.D. (2012) Metformin activates atypical PKC-CBP pathway to promote neurogenesis and enhance spatial memory formation. Cell Stem Cell, *11,* 23-35.

West, M.J. and Gundersen, H.J. (1990) Unbiased stereological estimation of the number of neurons in the human hippocampus. J Comp Neurol *296*:1-22.

West, M.J., Slomianka, L. and Gundersen, H.J. (1991) Unbiased stereological estimation of the total number of neurons in thesubdivisions of the rat hippocampus using the optical fractionator. Anat. Rec. *231*, 482-497

Wojtowicz, J.M., and Kee, N. (2006). BrdU assay for neurogenesis in rodents. Nat. Protoc. 1, 1399–1405.